

Electronic Thesis and Dissertation Repository

5-4-2016 12:00 AM

Seismic Vulnerability of Buried Energy Pipelines in Northern Canada

Behrang Dadfar
The University of Western Ontario

Supervisor
M. Hesham El Naggari
The University of Western Ontario

Graduate Program in Civil and Environmental Engineering
A thesis submitted in partial fulfillment of the requirements for the degree in Doctor of Philosophy
© Behrang Dadfar 2016

Follow this and additional works at: <https://ir.lib.uwo.ca/etd>



Part of the [Geotechnical Engineering Commons](#), and the [Structural Engineering Commons](#)

Recommended Citation

Dadfar, Behrang, "Seismic Vulnerability of Buried Energy Pipelines in Northern Canada" (2016). *Electronic Thesis and Dissertation Repository*. 3805.
<https://ir.lib.uwo.ca/etd/3805>

This Dissertation/Thesis is brought to you for free and open access by Scholarship@Western. It has been accepted for inclusion in Electronic Thesis and Dissertation Repository by an authorized administrator of Scholarship@Western. For more information, please contact wlsadmin@uwo.ca.

Abstract

Permafrost in Canada's North covers the terrain either continuously or discontinuously. Geological hazards associated with the presence of permafrost are serious barriers against development of the northern hydrocarbon resources. In recent decades, negative effects of geohazards such as frost heave, thaw settlement, slope instability on the safety of northern pipelines are widely studied; however, those of the seismic events are not. During earthquakes, buried pipelines may suffer damage from the induced transient ground deformations (TGD) and/or permanent ground deformations (PGD). While the former is caused by seismic wave propagation, the latter can result from liquefaction, faulting and landslides. This thesis investigates the effects of seismic hazards on the safety of northern pipelines.

In discontinuous permafrost regions, the subsurface conditions are complex due to the presence of intermittent scattered frozen areas. Therefore, this case is studied by means of shaking table tests and 2D numerical modelling. It is concluded that the site response at the top of frozen zones is larger than that at the top of unfrozen zones. Consequently, the pipelines in discontinuous permafrost regions are exposed to intermittent differential ground motions during wave propagation. Pipeline response to this type of excitation is investigated using a finite element program developed in Matlab in which soil and pipe nonlinearities, large deformations and cross-sectional ovalization of the pipe are considered. Tensile rupture, local buckling and premature cross-sectional failure are checked and it is observed that the pipes have a margin of safety under TGD.

Northern pipelines behaviour subjected to the PGD caused by active-layer detachments, the most common type of landslides in the permafrost regions, is also studied. Considering soil and slope uncertainties and utilizing Monte Carlo technique, probabilistic slope stability analysis is performed first. The probability of exposure to the landslide-caused PGD and the statistical distribution of the PGD zone affecting to the pipelines are computed. The pipeline response to this PGD zone is then calculated utilizing the developed structural analysis program. Finally, effects of PGD zone

geometric uncertainties are simulated using Monte Carlo technique and damage functions for the pipelines under PGD are derived.

Keywords

Buried steel pipelines, pipe cross-sectional ovalization, finite element analysis, site response analysis, cold regions, permafrost, shaking table, seismic wave propagation, landslides, permanent ground deformation, vulnerability functions.

Co-Authorship Statement

This thesis has been prepared in accordance with the regulations for an Integrated Article format thesis stipulated by the School of Graduate and Postdoctoral Studies at Western University. Statements regarding the co-authorship of individual chapters are as follows:

Chapter 2: Ovalization of steel energy pipelines buried in saturated sands during ground deformations

A version of this paper has been co-authored by B. Dadfar, M. H. El Naggar and M. Nastev and has been published in the journal of Computers and Geotechnics.

All the numerical modelling, interpretation of results and writing the draft were carried out by B. Dadfar, under the supervision of M. H. El Naggar and M. Nastev. The supervisors' contribution consisted of providing advice throughout the research program and reviewing the draft and the publication from this research.

Chapter 3: Experimental and analytical study of seismic site response of discontinuous permafrost

A version of this paper has been co-authored by B. Dadfar, M. H. El Naggar and M. Nastev and has been published in the Canadian Geotechnical Journal.

All the experimental and numerical modelling, interpretation of results and writing the draft were carried out by B. Dadfar, under the supervision of M. H. El Naggar and M. Nastev. The supervisors' contribution consisted of providing advice throughout the research program and reviewing the draft and the publication from this research.

Chapter 4: Vulnerability of buried energy pipelines subject to seismic wave propagation in discontinuous permafrost

A version of this paper has been co-authored by B. Dadfar, M. H. El Naggar and M. Nastev and has been submitted to the journal of Soil Dynamics and Earthquake Engineering.

All the numerical modelling, computer programming, interpretation of results and writing the draft were carried out by B. Dadfar, under the supervision of M. H. El Nagggar and M. Nastev. The supervisors' contribution consisted of providing advice throughout the research program and reviewing the draft and the publication from this research.

Chapter 5: Quantifying exposure of buried pipelines to earthquake-triggered transverse landslides in permafrost thawing slopes

A version of this paper has been co-authored by B. Dadfar, M. H. El Nagggar and M. Nastev and has been submitted to the Canadian Geotechnical Journal.

All the numerical modelling, computer programming, interpretation of results and writing the draft were carried out by B. Dadfar, under the supervision of M. H. El Nagggar and M. Nastev. The supervisors' contribution consisted of providing advice throughout the research program and reviewing the draft and the publication from this research.

Chapter 6: Vulnerability of buried energy pipelines subject to earthquake-triggered landslides in permafrost thawing slopes

A version of this paper has been co-authored by B. Dadfar, M. H. El Nagggar and M. Nastev and has been submitted to the journal of Geotechnique.

All the numerical modelling, computer programming, interpretation of results and writing the draft were carried out by B. Dadfar, under the supervision of M. H. El Nagggar and M. Nastev. The supervisors' contribution consisted of providing advice throughout the research program and reviewing the draft and the publication from this research.

Acknowledgments

The completion of the thesis has brought sharply into focus the debt of gratitude owed to a number of people.

It is my pleasure to acknowledge my supervisor, Dr. M. Hesham El Naggar, and my joint supervisor from Natural Resources Canada, Dr. Miroslav Nastev, for their assistance, advice, mentorship and encouragement. Dr. El Naggar provided me the required research facilities, shared his knowledge and experience with me and helped to overcome the barriers of this research work. Dr. Nastev patiently revised drafts and publications and offered many constructive comments and suggestions that served to improve this work.

I am very grateful to the technical staffs of the Boundary Layer Wind Tunnel, Gerry Dafoe and Anthony Burggraaf, and laboratory supervisor, Wilbert Logan, for their assistance during my experimental work. As well, many thanks go to my friends at Western University who provided me a pleasant work environment.

Appreciation is also expressed to Natural Resources Canada for their Research Affiliate Program scholarship and to the Ontario Graduate Scholarship program for their financial support.

I am sincerely grateful to my family, specially my parents, for their unfailing love and endless support and would like to dedicate this thesis to them.

Last but not least, I wish to express my deepest gratitude to my lovely wife and my best colleague, Naemeh Naghavi. Thank you for always supporting me in my academic pursuits and for the wonderful life that we share together.

Table of Contents

Abstract	i
Co-Authorship Statement.....	iii
Acknowledgments.....	v
Table of Contents	vi
List of Tables	ix
List of Figures	xi
List of Appendices	xix
Chapter 1	1
1 Introduction	1
1.1 Background.....	1
1.2 Thesis objectives.....	3
1.3 Thesis outlines	4
1.4 Original contributions	5
References	5
Chapter 2.....	8
2 Ovalization of steel energy pipelines buried in saturated sands during ground deformations.....	8
2.1 Introduction and literature review.....	8
2.2 Numerical model.....	11
2.3 Results.....	18
2.4 Conclusions.....	27
References	28
Chapter 3.....	31

3	Experimental and analytical study of seismic site response of discontinuous permafrost	31
3.1	Introduction.....	31
3.2	Physical modelling with reduced-scale 1g shaking table tests	33
3.3	Numerical simulations	41
3.4	Experimental and numerical results	44
3.5	Practical application of results	55
3.6	Conclusions.....	59
	References	60
	Chapter 4.....	65
4	Vulnerability of buried energy pipelines subject to seismic wave propagation in discontinuous permafrost	65
4.1	Introduction.....	65
4.2	Seismic wave propagation	66
4.3	Discontinuous permafrost site response.....	68
4.4	Pipeline response to wave propagation.....	76
4.5	Response to wave propagation in discontinuous permafrost	84
4.6	Summary and conclusions	92
	References	93
	Chapter 5.....	98
5	Quantifying exposure of buried pipelines to earthquake-triggered transverse landslides in permafrost thawing slopes	98
5.1	Introduction.....	98
5.2	Objectives and scope of work	99
5.3	Pipeline exposure to transverse ALD hazard.....	99
5.4	ALD geometry	101

5.5 Assessment of ALD deformations	105
5.6 Probability of exposure and Monte Carlo simulations	115
5.7 Summary and conclusions	120
References	121
Chapter 6.....	127
6 Vulnerability of buried energy pipelines subject to earthquake-triggered landslides in permafrost thawing slopes	127
6.1 Introduction.....	127
6.2 Seismic vulnerability function	129
6.3 Analysis of pipeline damage.....	131
6.4 Damage evaluation.....	140
6.5 Summary and conclusions	143
References	144
Chapter 7.....	148
7 Summary and conclusions.....	148
7.1 Summary.....	148
7.2 Conclusions.....	150
7.3 Suggestions for future studies.....	153
Appendix A.....	155
Technical specifications of measuring instruments	155
Appendix B	156
Acceleration time-histories	156
Appendix C	159
Evaluating the goodness-of-fit.....	159
References	161
Curriculum Vitae	162

List of Tables

Table 2-1: Soil physical properties.	13
Table 2-2: Parameters considered in parametric study.	18
Table 3-1: Scale factors for 1g shaking table tests on soil-structure-fluid models (Iai 1988).	35
Table 3-2: Soil properties.....	37
Table 3-3: Variations of cohesion with temperature (θ) for a silty sand (Tsytoich 1975).	38
Table 3-4: Uniaxial compression resistance of structurally undisturbed permafrost (silty sand) (Tsytoich 1975).	39
Table 3-5: Configurations of soil models used in experimental program (all dimensions in centimetres).....	41
Table 4-1: GEV distribution parameters of W_f and W_u in 100 km intervals of the Norman Wells to Zama oil pipeline route.....	70
Table 4-2: Parameters of loose and medium dense soils denoted by L and D in this study.	83
Table 4-3: Comparison of the pipe strains obtained from homogeneous and non-homogeneous grounds.	86
Table 5-1: Statistical parameters of active-layer detachments at “Hot Weather Creek” site, Fosheim Peninsula, estimated based on Lewkowicz (1990).....	102

Table 5-2: ALD width and length medians at three locations on the Fosheim Peninsula: “Black Top Creek” (BTC), “Hot Weather Creek” (HWC) and “Big Slide Creek” (BSC).	103
Table 5-3: Correction factors used in the estimation of factor of safety against liquefaction in this study.	108
Table 5-4: Newmark displacement threshold values (Jibson 2011).	112
Table 5-5: Input variables for Monte Carlo simulations.	116
Table 5-6: Probabilities of exposure, weakening instability and inertial instability obtained from Monte Carlo simulations.	119
Table 6-1: Probability of exposure and the peak PGD (δ) Weibull distribution parameters from Chapter 5.	132

List of Figures

Figure 2-1: Bilinear force–displacement of soil in (a) horizontal, (b) axial and (c) vertical (upward and downward) directions based on ALA (2001).	12
Figure 2-2: Soil model assuming discrete nonlinear springs along the pipeline: cross-sections with (a) horizontal end displacement, (b) downward and (c) upward end displacements. Axial springs are not shown.	13
Figure 2-3: Non-dimensional soil stiffness in (a) downward, (b) upward and (c) horizontal directions. H/D is the normalized burial depth. Dense sands are represented with solid line, whereas loose sands are indicated with dashed line.	14
Figure 2-4: Boundary conditions of (a) the in-air pipe and (b) the buried pipe.....	15
Figure 2-5: Numerical results of the current study compared to those presented by Limam et al. (2010). P is normalized internal pressure, OV is ovalization factor, and K is normalized curvature, defined by Equations (2-3).....	16
Figure 2-6: Key parameters that formed nondimensional variables in the analyses (H/D , D/t and P).	17
Figure 2-7: Simulated horizontal and vertical displacements for pipe type “A” ($D/t = 18$). SL and SD indicate shallow pipe buried in loose and dense sandy soil, respectively (blue solid and dotted lines); DL and DD indicate deep pipe buried in loose and dense sandy soil, respectively (red solid and dotted lines) Black dotted line indicates response of above-ground pipe (in-air).	20
Figure 2-8: Simulated horizontal and vertical displacements for pipe type “B” ($D/t = 86$). SL and SD indicate shallow pipe buried in loose and dense sandy soil, respectively (blue solid and dotted lines); DL and DD indicate deep pipe buried in loose and dense sandy soil, respectively (red solid and dotted lines) Black dotted line indicates response of above-ground pipe (in-air).	22

Figure 2-9: Soil yield index (SYI) for (a) pipe type “A” and (b) pipe type “B”. H, VD and VU denote horizontal, downward and upward end displacements, respectively.....23

Figure 2-10: Ovalization of deep pipe (H/D=10) buried in dense sand for horizontal end displacement, (a) pipe type “A” (D/t=18) moment-curvature, (b) pipe type “B” (D/t=86) moment-curvature, (c) pipe type “A” ovalization-curvature and (d) pipe type “B” ovalization-curvature. Different levels of hoop stress in the pipe circumference are presented as percentages of SMYS.....25

Figure 2-11: (a) Von Mises yield criterion, and approximate flexural stress distribution under (b) low and (c) high internal pressures.26

Figure 3-1: Dynamic interaction between frozen soil blocks (in gray color) and the surrounding unfrozen soil.33

Figure 3-2: Test setup including (from left to right): data acquisition system, the electric control module, shaking table with the mounted flexible container with 12 frames; and sand-cement blocks representing frozen soils.....36

Figure 3-3: Particle size distribution curves.37

Figure 3-4: Schematic presentation of typical test setup: (a) longitudinal cross-section and (b) top view. Frozen soil blocks are indicated in grey color. H_f , height of frozen block; W_f , width of frozen block; W_u , distance separating frozen blocks.41

Figure 3-5: Shear modulus reduction curves for frozen sand at -1°C by Singh and Donovan (1977) and average unfrozen sand by Seed and Idriss (1970).43

Figure 3-6: Transfer function of unfrozen soil deposit under low-intensity base excitation, $\text{PGA}=0.05\text{g}$. Dashed arrows indicate the first three natural frequencies of the model.....45

Figure 3-7: Experimental and numerical acceleration response spectra (respectively denoted by Exp and Num) after performing vertical stiffness corrections.46

Figure 3-8: Results of experiment No. 2: (a) acceleration response spectra and (b) ratio of the frozen block and unfrozen soil response spectra.....47

Figure 3-9: Acceleration response spectra at the top of (a) frozen blocks, and (b) unfrozen soil. Legends indicate thickness of frozen blocks, where H denotes total thickness of soil layers.47

Figure 3-10: Spectral acceleration obtained from shaking table experiments (Exp) and numerical modelling (Num) for (a) $W_u=5W_f$ and (b) $W_u=3W_f$. Time histories of r_u in unfrozen soils measured at depth of 5 cm at mid-distance between blocks for (c) $W_u=5W_f$ and (d) $W_u=3W_f$. Subscripts f and u indicate frozen and unfrozen soil responses, respectively.49

Figure 3-11: Study of effect of span length (W_u) on site response in (a) frozen and (b) unfrozen soils.50

Figure 3-12: Study of effect of block width (W_f) on site response in (a) frozen and (b) unfrozen parts.....51

Figure 3-13: Envelopes of maximum and minimum spectral response for the number of frozen blocks varying between two and five. Distance between the blocks remained constant, $W_u=50$ cm.52

Figure 3-14: Sensitivity of site response to varying shear wave velocity of frozen blocks. Distance between blocks remained constant, $W_u=50$ cm.53

Figure 3-15: Experimental readings of PGA in frozen blocks and unfrozen soils for (a) low, (b) medium and (c) high intensities of base excitations. Dashed lines depict average of the PGAs.....54

Figure 3-16: Top view of test setup of experiment No. 8. Dashed lines represent location of blocks in experiment No. 7 for comparison.....54

Figure 3-17: Comparison of free-field responses of plane strain and 3D cases in (a) frozen and (b) unfrozen soils.....55

Figure 3-18: Schematic profile of temperature and shear wave velocity (V_s) in depth of permafrost based on LeBlanc et al. (2004).56

Figure 3-19: Schematic horizontal distribution of temperature and shear wave velocity in discontinuous permafrost regions and spring model of permafrost-transition zones system.58

Figure 4-1: Top view of a pipeline impacted by seismic waves propagating in a homogeneous medium with the angle of incidence α67

Figure 4-2: Distribution of width of (a) frozen parts (W_f), and (b) unfrozen parts (W_u) along the Norman Wells oil pipeline based on geophysical surveys of Kay et al. (1983). The distance is measured from Norman Wells toward Zama.69

Figure 4-3: Generalized extreme value distributions of (a) W_f , and (b) W_u in 100 km intervals of the Norman Wells to Zama oil pipeline route. The distance is measured from Norman Wells, Northwest Territories, toward Zama, Alberta, Canada.70

Figure 4-4: Top view of the shaking table test setups and the configurations of permafrost representing buried blocks for (a) plane strain, and (b) 3D cases used in Chapter 3 in site response study.72

Figure 4-5: Top view of a hypothetical discontinuous permafrost region and the distribution of PGA along the Section A-A.72

Figure 4-6: PGA at the top of (a) frozen blocks, and (b) unfrozen soil (at the middle of unfrozen span) based on the experimental and numerical findings of Chapter 3.73

Figure 4-7: The functions fitted to the simulated site response results of Chapter 3: (a) PGA_f , and (b) PGA_u for $W_f=10$ m.74

Figure 4-8: The acceleration response spectra of the input motion records. Data from PEER (2016) and USGS (2016).75

Figure 4-9: Variations of the PGA response of (a) frozen and (b) unfrozen parts with PGA of the bedrock, PGA_r and deposit thickness (depth to bedrock), H .	75
Figure 4-10: A dynamic Winkler element i - j for buried pipes comprised of frame element with lumped masses, soil springs and dashpots.	78
Figure 4-11: Dimensionless parameters of soil damping for lateral (\bar{S}_{u2}) and axial (\bar{S}_{v2}) directions. (Adapted from Hindy and Novak 1979)	78
Figure 4-12: Top view of the displacement response of a pipeline segment subjected to transient ground deformations. U_{qst} and U_{dyn} represent the quasi-static and dynamic parts of the response, respectively, and U_g is the ground deformation.	80
Figure 4-13: Discretization of pipe cross-section at plastic hinge.	81
Figure 4-14: (a) The moment-curvature and (b) the ovalization-curvature for a pipe made of X65 steel with $D/t=96$ subjected to cyclic bending moment. The bending moment and curvature are normalized with respect to the yield moment and curvature, M_y and Φ_y , respectively.	82
Figure 4-15: Response of a straight pipeline segment to S and R waves with and without considering soil-pipe interaction (SPI): (a) axial strains under S waves, (b) bending strains under S waves, (c) axial strains under R waves, and (d) bending strains under R waves.	84
Figure 4-16: Different burial conditions considered in this study. Sections A-A to D-D indicate the longitudinal pipeline view, the partial burial, the unfrozen span burial, and the full burial in active layer, respectively.	85
Figure 4-17: Response of an ISS straight pipeline segment to S and R waves: (a) axial strains under S waves, (b) bending strains under S waves, (c) axial strains under R waves, and (d) bending strains under R waves. D and L respectively represent dense and loose soils, and the kilometerpost of the considered intervals of the Norman Wells pipeline route are denoted in parentheses.	87

Figure 4-18: Response of a MSS straight pipeline segment to R waves buried in a terrain with average geothermal conditions of kmp 700-800: (a) axial strains, and (b) bending strains. D and L respectively represent dense and loose soils, and MSS and ISS stand for multiple and identical support stiffness pipelines, respectively.....88

Figure 4-19: Effect of frequency content on the response of a straight pipeline segment to R waves: (a) axial strains, and (b) bending strains.89

Figure 4-20: Effect of pipe diameter, D, and diameter to wall-thickness ratio, D/t, on (a) axial strains, and (b) bending strains, and effect of burial depth, d, on (c) axial strains, and (d) bending strains.....91

Figure 4-21: Variation of total strain (axial+bending) with the angle of incidence for the worst case scenario.92

Figure 5-1: Mechanisms of material transfer and distribution of the PGD for: (a) translational and (b) compressional movement. L represents the total landslide length, L_s is the scar zone length and S is the distance of scar crown to pipeline axis.100

Figure 5-2: Top view of a hypothetical pipeline segment exposed to potential active-layer detachments (ALD) and the relevant parameters: ALD width (W) and length (L), length of scar zone (L_s) and distance of scar crown to pipeline axis (S). ALDs that impact the pipeline are shown in grey.101

Figure 5-3: Landslide area distributions of active-layer detachments in permafrost region and some global landslides from Malamud et al. (2004).....103

Figure 5-4: Simplified relationship of the cyclic resistance ratio (CRR) in M7.5 earthquakes and SPT results, developed for this study based on Seed et al. (1985) and recommendation of NCEER workshop (1996) published by Youd et al. (2001).107

Figure 5-5: Infinite thawed slope in cold region with related parameters.111

Figure 5-6: Flowchart showing the procedure of earthquake-induced ALD scar length calculations.113

Figure 5-7: Boore et al. (1997) PGA attenuation used in this study. R is the closest horizontal distance of the site to the vertical projection of the fault rupture plane. 115

Figure 5-8: Venn diagram of the slope samples generated by Monte Carlo technique...117

Figure 5-9: Variation of the cumulative distribution function (CDF) of the index of exposure (I_E) with (a) distance of the pipeline axis to the scar crown S, (b) thaw-consolidation ratio R_{tc} , (c) earthquake magnitude M, and (d) source-to-site distance R. 118

Figure 5-10: Variation of the cumulative distribution function (CDF) of the PGD with (a) distance of the pipeline axis to the scar crown, (b) thaw-consolidation ratio, (c) earthquake magnitude and (d) source-to-site distance..... 119

Figure 6-1: (a) Parameters that characterize an active-layer detachment (ALD) hazard: ALD width (W), length (L), scar length (L_S), and distance of scar crown to pipeline axis (S), and (b) distribution of ALDs along a pipeline route, which may or may not impact the pipeline..... 128

Figure 6-2: PGD spatial variation and locations of the potential plastic hinges on pipeline. 132

Figure 6-3: The side and front views of (a) undeformed plastic hinge, and (b) deformed plastic hinge under a bending moment. 134

Figure 6-4: Normalized moment-curvatures resulted from the present study (continuous lines) compared to (a) experimental results of Sherman (1983) for pure bending ($D/t=36$ and 96), and (b) analytical results of Sohal and Chen (1987) for combined bending moment-axial force only ($D/t=36$). M_y , Φ_y and P_y represent the yield moment, yield curvature and yield axial force of the cross-section, respectively. 135

Figure 6-5: Modification of the yield capacity of the pressurized pipes: (a) biaxial stress condition, (b) the Von Mises yield criterion, and (c) the corrected stress-strain curves based on the Von Mises criterion..... 136

Figure 6-6: Responses of a 400 m-long segment of pipeline with $D=0.61$ m and $D/t=64$ made of X52 steel subjected to three levels of PGD zone width (W). Comparison of (a) bending moments, (b) axial forces and (c) maximum pipe strains resulted from this study with those of Liu and O'Rourke (1997). Results of this study are presented with dashed lines. 139

Figure 6-7: (a) Maximum pipe strains and (b) maximum pipe ovalization according to ALA (2001b) definition in a 600 m-long segment of pipeline with $D=0.61$ m and $D/t=78$ made of X52 steel subjected to three levels of PGD zone width (W). Results of the simulations for the pressurized pipes are shown with dashed lines. 141

Figure 6-8: Critical values of peak PGD, δ_{cr} , as a function of PGD zone width, W , for unpressurized pipes. 142

Figure 6-9: Repairs for one ALD, RR_{ALD} , as a function of mean and COV of δ 142

List of Appendices

Appendix A: Technical specifications of measuring instruments	155
Appendix B: Acceleration time-histories.....	156
Appendix C: Evaluating the goodness-of-fit	159

Chapter 1

1 Introduction

1.1 Background

In the current seismic risk assessment procedures, performance of continuous buried energy pipeline is evaluated empirically following a similar approach to that employed by the water industry for segmented pipeline. However, the damage level in the continuous pipelines is generally considered at 30% of the predicted damage in segmented pipelines (FEMA 2003). Being more ductile, continuous pipelines are capable of sustaining ground deformations better than segmented pipelines, and consequently suffer less damage.

The existing vulnerability functions for buried pipelines recommended by American Lifelines Alliance (ALA) correlate the number of damages per unit length to a given seismic intensity measure (ALA 2001a). Since the mid-70s, parameters such as peak ground acceleration, peak ground velocity, peak ground displacement, modified Mercalli intensity, Arias intensity, spectral acceleration, spectral intensity, maximum ground strain and composite parameters are employed as measures of intensity (Pineda-Porras and Najafi 2010). Determined from post-seismic observations, existing pipeline vulnerability functions reflect the pipeline performance under the actual field conditions. However, these field conditions do not cover the whole range of the potential input motions, site conditions and pipe properties. Consequently, they can only roughly estimate the average loss under average site and structural conditions and are not predictive for future events and every site condition.

The recorded damages are characterized as leaks and breaks that result from different modes of failure. For continuous pipelines, the following failure mechanisms typically generate damage: tensile rupture, local buckling and sometimes beam buckling (O'Rourke 2003). The cross-sectional ovalization under bending moment should be added to this list as it can also lead to premature failure and endanger pipeline safety. To prevent potential collapse, modern codes and guidelines, such as the Canadian standard for oil and gas pipeline systems (CAN-CSA Z662 2003) and the American Lifelines

Alliance guidelines for the design of buried steel pipes (ALA 2001b), have limited the maximum pipe strains and cross-sectional ovalization.

Transient ground deformations (TGD) and permanent ground deformations (PGD) caused by earthquakes can be very destructive. TGD occurs due to seismic wave propagation and depends on the local site conditions and the properties of the released seismic waves at the surface. When the seismic waves travel in nonhomogeneous terrains such as those composed of discontinuous horizontal media, the spatially variable ground shaking and the respective TGD can be critical to the pipeline integrity (Liang and Sun 1994, and Zerva et al. 1988). PGD, on the other hand, is a result of earthquake-induced ground failures such as liquefaction, landslide, and fault rupture (FEMA 2003). When compared to TGD, PGD in general generates considerably larger displacements and consequently higher damages are expected. The evaluation of both TGD and PGD is important in the planning process during the pre-construction stage for accurate aseismic design, and in the post-construction period for seismic risk assessment.

Canada's north, rich in hydrocarbon resources, is mainly covered by permafrost (Government of Canada 2016). Permafrost is a term used to describe the thermal condition of earth materials when their temperature remains below 0°C for two or more consecutive years (Muller 2007). The permafrost can be continuous when its presence is ubiquitous, or discontinuous with only occasional presence. From a geotechnical earthquake engineering point of view, continuous permafrost can be treated simply as a stiff soil layer. However, discontinuous permafrost, which manifests itself as an intermittent horizontal terrain discontinuity along the pipelines, has many unknown aspects (Lawrence 2004) and represents serious geotechnical challenges for the pipelines.

The discontinuous permafrost represents a particular challenge for the wave propagation, since frozen soils have comparable higher shear wave velocities than unfrozen soils. When situated next to each other, the relatively high impedance contrast between these soils may contribute to important site effects and considerably affect the ground motion's correlation. As well, a number of potential geohazards such as frost heave, thaw settlement and slope instabilities are associated with discontinuous permafrost (Nixon et

al. 1990, DeGeer and Nessim 2008, and Oswell 2011). Aylsworth et al. (2000) identified various types of landslides in the permafrost regions. It was also shown that the thaw-consolidation phenomenon (Morgenstern and Nixon 1971), particular to ice-rich fine-grained soils, increases the pore water pressure and facilitates slope instability (McRoberts and Morgenstern 1974). As a result, during warm seasons the stable thawing permafrost slopes subject to ground shakings may easily become unstable and cause ground failures (McRoberts 1978).

1.2 Thesis objectives

Although seismic aspects related to geohazards in discontinuous permafrost regions represent a threat to the safety and security of the engineering structures, it is observed that the quantification of the potentially negative effects on the pipelines has not received sufficient attention. This thesis aims to fill in the gaps in current knowledge and to experimentally and numerically investigate the seismic vulnerability of steel energy pipelines buried in discontinuous permafrost regions. The main objectives of the thesis are to:

- Develop a reasonably accurate tool for the analysis of static and dynamic responses of buried pipelines. It involves development of finite element analysis program that accounts for the soil-pipe interactions, large deformations, material nonlinearities (soil and pipe) and geometric nonlinearities of the pipe cross-section.
- Investigate the effects of discontinuous permafrost on the site response considering geological and geotechnical settings typical for northern Canada and propose a quantification model.
- Analyze buried pipelines subject to TGD resulting from wave propagation in discontinuous permafrost in order to determine the respective analytical vulnerability functions.
- Quantify the potential PGD caused by typical landslides occurring in permafrost regions.

- Analyze buried pipeline response subject to PGD in order to derive the associated analytical vulnerability functions.

The outputs of this thesis can be employed for aseismic design of energy pipelines in northern permafrost and discontinuous permafrost conditions. As well, the generated vulnerability functions can be used by the existing regional risk assessment platforms, such as the FEMA's Hazus (FEMA 2003).

1.3 Thesis outlines

This dissertation comprises seven chapters. Chapter 1 presents an introduction that addresses the background, objectives, outlines and original contributions of the research.

In Chapter 2, cross-sectional ovalization of buried steel pipes is numerically studied employing the finite element program, Abaqus (Dassault Systemes 2007). Considering parameters such as soil density, burial depth, pipe diameter to wall-thickness ratio and the internal pressure, some moment-curvature and ovalization-curvature functions exclusive to buried pipes are developed and presented.

Chapter 3 is devoted to the discontinuous permafrost site response studies. The results of the experimental and numerical modelling phases of the study obtained respectively from shaking table tests and analysis using FLAC software (Itasca Consulting Group, Inc. 2002) are presented.

In Chapter 4, the findings of Chapter 3 are extended to certain practical cases derived based on the geological settings of the Mackenzie Valley region (Northwest Territories, Canada) and a model is presented for that. A detailed parametric study is performed next on the pipeline response under TGD using a finite element program developed in Matlab (The MathWorks, Inc. 2011).

Chapter 5 focuses on the PGD hazard of the most common type of permafrost-region landslides, i.e., active layer detachments (ALD). A probabilistic framework is adopted to account for the numerous uncertainties in quantifying the ALD hazard.

Chapter 6 applies the results of Chapter 5 as input to determine the pipeline response under PGD. Vulnerability functions are then derived with a probabilistic approach.

Chapter 7 presents the summary and conclusions of the thesis and provides recommendations for future research.

1.4 Original contributions

This study claims the following original contributions:

- Presented moment-curvature and ovalization-curvature relationships for buried steel pipes under different soil, pipe, burial depth and internal pressure conditions.
- Addressed seismic site response of discontinuous permafrost regions experimentally and numerically.
- Performed numerical pipeline analysis under wave propagation effects in discontinuous permafrost regions.
- Introduced a novel probabilistic model for quantifying permanent ground deformations of earthquake-induced active layer detachment landslides applied to buried pipelines.
- Derived analytical vulnerability functions for buried steel pipes under permanent ground deformations of earthquake-induced active layer detachment landslides.

References

Abaqus 6.7 User Documentation. Dassault Systèmes, 2007.

Aylsworth, J. M., A. Duk-Rodkin, T. Robertson, and J. A. Traynor. "Landslides of the Mackenzie Valley and adjacent mountainous and coastal regions." In *The physical environment of the Mackenzie Valley, Northwest Territories: a base line for the assessment of environmental change*. Edited by L. D. Dyke, & G. R. Brooks. Geological Survey of Canada, Bulletin 547, 2000. 167-176.

CSA Z662-03 oil and gas pipeline systems. Mississauga, ON: Canadian Standards Association, 2003.

DeGeer, D., and M. Nessim. "Arctic pipeline design considerations." *Proceedings of the ASME 27th International Conference on Offshore Mechanics and Arctic Engineering*. Estoril, Portugal, 2008.

FLAC, fast lagrangian analysis of continua, user's guide. Minneapolis, MN: Itasca Consulting Group, Inc., 2002.

Government of Canada. Natural Resources Canada. <http://www.nrcan.gc.ca/earth-sciences/geography/atlas-canada/selected-thematic-maps/16872> (accessed December 20, 2015).

Guideline for the design of buried steel pipe. American Lifelines Alliance, 2001.

Lawrence, D. E. *Survey of expert opinion on permafrost and geotechnical issues for northern pipelines*. Ottawa: Geological Survey of Canada, 2004.

Liang, J., and S. Sun. "Site effects on seismic behavior of pipelines: a review." *Journal of Pressure Vessel Technology* 122, no. 11 (2000): 469-474.

Matlab and Statistics Toolbox Release 2011b. Natick, MA: The MathWorks, Inc., 2011.

McRoberts, E. C. "Slope stability in cold regions." In *Geotechnical engineering for cold regions*, edited by O. B. Andersland, & D. M. Anderson, 363-404. New York, NY: McGraw-Hill Book Company, 1978.

McRoberts, E. C., and N. R. Morgenstern. "The stability of thawing slopes." *Canadian Geotechnical Journal* 11, no. 4 (1974): 447-469.

Morgenstern, N. R., and J. F. Nixon. "One-dimensional consolidation of thawing soils." *Canadian Geotechnical Journal*, 1971: 558-565.

Muller, S. W. *Frozen in time, permafrost and engineering problems*. Edited by H. French, & F. Nelson. ASCE, 2007.

"Multi-hazard loss estimation methodology earthquake model HAZUS MH MR4 technical manual." Washington, DC: Federal Emergency Management Agency (FEMA), 2003.

Nixon, J. F., K. A. Sortland, and D. A. James. "Geotechnical aspects of northern gas pipeline design." *The Fifth Canadian Permafrost Conference*. Quebec City, 1990.

O'Rourke, M. J. "Buried pipelines." Chap. 23 in *Earthquake engineering handbook*, edited by W. F. Chen, & C. Scawthorn. Boca Raton, FL: CRC Press, 2003.

Oswell, J. M. "Pipelines in permafrost: geotechnical issues and lessons." *Canadian Geotechnical Journal* 48 (2011): 1412-1431.

Pineda-Porras, O., and M. Najafi. "Seismic damage estimation for buried pipelines: challenges after three decades of progress." *Journal of Pipeline Systems Engineering and Practice* 1, no. 1 (2010): 19-24.

Seismic fragility formulations for water systems, Part 2- Appendices. American Lifelines Alliance, 2001.

Zerva, A., A. H. S. Ang, and Y. K. Wen. "Lifeline response to spatially variable ground motions." *Earthquake Engineering and Structural Dynamics* 16 (1988): 361-379.

Chapter 2

2 Ovalization of steel energy pipelines buried in saturated sands during ground deformations¹

2.1 Introduction and literature review

The various types of pipelines used by the oil industry are considered to be tubular structures. They normally operate under external pressures exerted by the backfill materials or by the sea water in offshore pipelines, and internal pressures generated by the transported liquid and gas products. In addition, buried pipelines are subjected to transverse and longitudinal forces induced by seismic waves and by various types of ground displacement such as downslope or lateral movements, vertical settling, fault rupturing, thawing and frost heaving in northern regions (Nixon et al. 1990, O'Rourke and Ayala 1993, and Oswell 2011). The pipelines should therefore be designed to withstand the resulting pressures, axial/shear forces and bending moments of different origins.

Due to their importance and unique mechanical behaviour under various loads, structural response of tubes under bending has been the focus of many research studies. Ovalization and bifurcation instabilities are the most important mechanical response features of tubular structural members under flexural loads.

Ovalization is a geometric nonlinearity that changes the circular cross-section of a tube to an oval shape. It is caused by vertical components of tensile and compressive flexural stresses in the cross-section resulting in reduction of the bending capacity due to transverse distortion. The negative effect of ovalization on the bending capacity of elastic cylindrical shells was first introduced by Brazier (1927) and is sometimes called the "Brazier effect". Ades (1957) expanded the previous work to long elastic-plastic tubes undergoing uniform ovalization and provided a nonlinear moment-curvature relationship. The ovalization due to bending is an important part of the pipe response to flexural loads and should be considered in the design of new pipelines and vulnerability assessment of

¹ A version of this chapter has been published in the journal of Computers and Geotechnics 69 (2015) 105-113.

the existing ones. The Canadian standard for oil and gas pipeline systems (CAN-CSA Z662 2003) limits flattening caused by ovalization to a critical value to be determined by “valid analysis methods or physical tests or both”. Also, the American Lifelines Alliance (ALA) considers the maximum allowable ovalization factor to be 15% (ALA 2001).

Bifurcation instability, on the other hand, refers to local buckling in compressive zones that develops wave-type wrinkles. Both instabilities prevent thin-walled tubular members from reaching the ultimate theoretical bending capacity. Studies have shown that the diameter to thickness ratio (D/t) is a key parameter in determining flexural capacity of the tubes (Schilling 1965, and Sherman 1976). Kim (1992) approximated plastic buckling of the pipes subjected to bending by an axisymmetric plastic bifurcation analysis under uniform axial compression combined with circumferential stresses caused by the internal pressure. It was concluded that the critical buckling strains increase with the increase of the circumferential stresses.

The effect of internal pressure on flexural response of in-air pipelines was studied for the first time by Bouwkamp and Stephen (1973). Seven 48-inch-diameter pipes ($D/t=104$ and 85) with different internal pressures were subjected to four-point bending tests to evaluate the local instabilities and the ultimate rupture. The study revealed that highly internally pressurized pipes show more flexibility under bending. Different local buckling mode shapes were observed: pipes under low internal pressure exhibit an inward diamond-shaped deformation, whereas pipes under high internal pressure tend to buckle outward with a bulged shape. The authors also observed that local buckling occurred at inelastic strains in all tests.

Gresnigt (1986) presented a number of formulas for assessing the bending capacity of buried steel pressurized pipelines in the settlement areas by applying the plastic theory. The analytical results were supported by few small-scale experiments. Also, a critical strain formula was presented based on the available test results from a number of studies. The proposed critical strain formula was shown to give reasonable results on the conservative side. Currently, this formula is suggested by the ALA and with few minor modifications by CAN-CSA Z662.

Murray (1997) conducted tests on pipes with $D/t=64$ and 51 under combined axial force, internal pressure and bending moment. It was shown that the finite element method could successfully capture the local buckling of the tested pipes under this combined loading. The effect of normalized length (L/D) on the mechanical response was also investigated. Although the aim of the research was the study of behaviour of buried pipelines, the effect of soil confinement was neither considered in the experiments nor in the finite element models.

More recently, Schaumann et al. (2005) conducted a series of scale model four-point bending experiments on steel pipes with $D/t=132$ and confirmed conclusions of previous studies regarding the effect of internal pressure. They emphasized the stabilizing effect of the internal pressure that leads to higher critical buckling strains.

Houliara and Karamanos (2006) used a special-purpose nonlinear finite element technique to predict pre- and post-buckling equilibrium path of the elastic thin-walled tubes under combined bending and internal/external pressure. They also developed a simplified closed-form solution for bifurcation that accounts for pressure and initial ovality and curvature. The behaviour of a steel pipe with $D/t=52$ subjected to internal pressure and bending moment was also investigated experimentally and numerically by Limam et al. (2010). The authors focused on the effect of internal pressure on ovalization, ultimate bending capacity and critical buckling strains.

Konuk et al. (1999) conducted lab experiments on the flexural behaviour of unpressurized buried pipes. They displaced laterally the ends of pipes buried in dense sand by means of two actuators at a low rate. Two D/t ratios of 43 and 64 were considered. The measured bending strains were substituted into BS 8010 (1993) formula, which relates ovalization to mechanical and geometrical properties of the pipe, bending strain and pressure and the results were compared to the measured ovalization factors. An appreciable discrepancy was observed for tested buried pipes, in contrast to some studies that showed relatively good agreement between predictions of the BS 8010 formula and real behaviour of the above-ground pipes. The authors attributed this difference to the confining role of the soil.

Mahdavi et al. (2013) developed a three dimensional continuum finite element model in Abaqus/Standard which included the soil and pipeline. The model was first calibrated against the results of Konuk et al. (1999). A parametric study was conducted afterward to understand the effect of critical parameters on the local buckling of pipes buried in firm clayey soil. An empirical equation for the critical buckling strain was proposed based on the obtained numerical results.

As it can be seen from the above review, numerous studies have been conducted in the past decades to explain the flexural behaviour of pipelines. Some of them included the effect of boundary conditions, residual stresses, and experimentation method together with the assemblage and type of used materials. However, only a few of them considered the combined effect of soil and internal pressure on the response. In addition, the published results exhibit considerable variations due to the number of different parameters that influence the response, and there is no consensus on the validity and reliability of the available formulas for different loading conditions.

This study aims to determine typical non-dimensional relationships between the bending moment and resulting ovalization for buried pipes by considering effect of parameters such as normalized burial depth (H/D), diameter to wall-thickness ratio (D/t), sand density and level of the internal pressure. The finite element analysis which is commonly used in practice was applied with three-dimensional (3D) shell elements since they are particularly suitable to consider the effects of internal pressure, geometric nonlinearities of the cross-section and local buckling instabilities.

2.2 Numerical model

2.2.1 Soil spring representation

The ALA (2001) suggested the use of elastic perfectly plastic springs to represent the soil response of the soil-pipe systems in the three directions (longitudinal, horizontal and vertical) (Figure 2-1). These relationships were derived based on experimental and theoretical studies performed in the past decades on buried pipelines and other similar geotechnical structures such as piles and anchor plates.

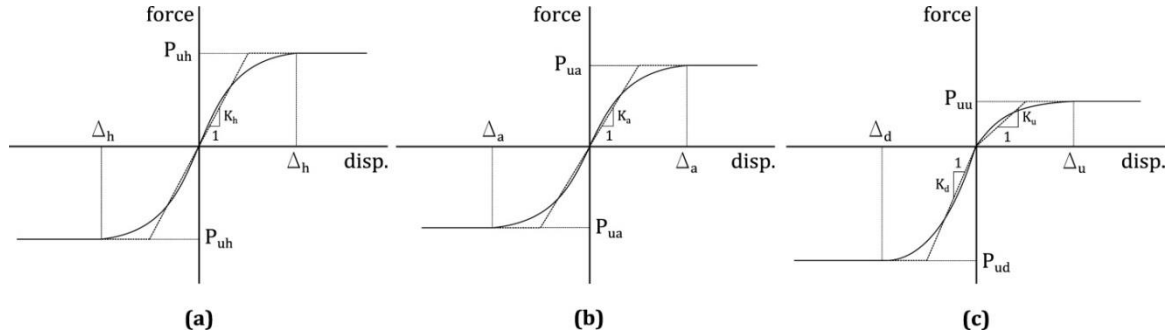


Figure 2-1: Bilinear force–displacement of soil in (a) horizontal, (b) axial and (c) vertical (upward and downward) directions based on ALA (2001).

The nonlinear force-displacement spring curves are widely used in the design of buried pipelines and are employed in the present study. These springs can be added to beam or shell elements that represent pipelines (Xie et al. 2013). In this study, the horizontal and vertical end displacements were considered independently and the stiffness of the soil springs in each cross-section was assumed to be distributed at the three respective semicircles (Figure 2-2). As an example, the top springs were distributed over the nodes of the top semicircle and their stiffness was determined based on the projection of their tributary area on a plane perpendicular to the direction of displacement. The same method was applied to the side and bottom springs. Since the loading was monotonic, it was not necessary to use gap elements. In the case of horizontal end displacement, the lateral resistance is provided by the soil spring stiffness K_h , whereas the upward and downward stiffness (K_u and K_d) provide the vertical confinement. Likewise, in the case of vertical end displacement and depending on its direction, either upward or downward stiffness (K_u or K_d) resists the motion vertically and K_h confines the pipeline horizontally. The soil bearing mechanisms in the upward and downward directions are different and this results in different values for stiffness in the vertical direction. On the other hand, due to symmetry, the horizontal stiffness is the same in both directions. The resulting deformations δh , δu and δd are used to compute the level of ovalization in both directions.

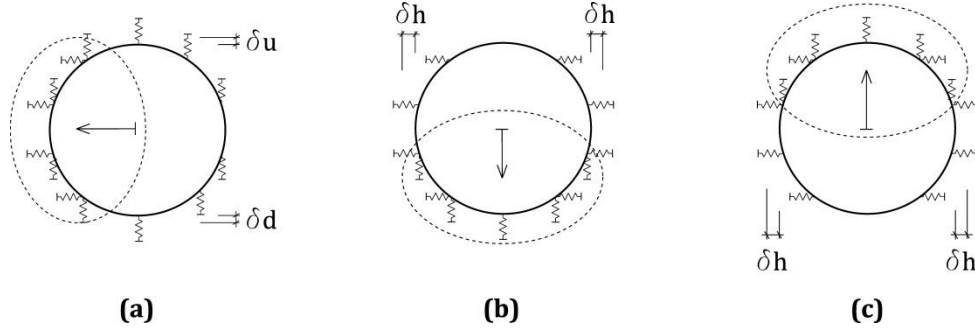


Figure 2-2: Soil model assuming discrete nonlinear springs along the pipeline: cross-sections with (a) horizontal end displacement, (b) downward and (c) upward end displacements. Axial springs are not shown.

The physical properties of the considered saturated sandy soils ($c=0$) are assumed for loose and dense sands representing the lower- and upper-bound properties of the surrounding soil, respectively. Physical properties assumed for these soils are presented in Table 2-1 where ϕ is the internal friction angle, e is the void ratio, w is the moisture content, γ is the total unit weight, γ' is the effective unit weight, G_s is the soil particles specific gravity and D_r is the relative density.

Table 2-1: Soil physical properties.

Sand Type	ϕ	e	w	γ	γ'/γ	G_s	D_r (%)
Loose	30°	0.8	0.30	19.0	0.484	2.7	25
Dense	45°	0.4	0.15	21.7	0.548	2.7	80

The soil stiffness in the downward (K_d), upward (K_u), horizontal (K_h) and axial (K_a) directions was calculated dividing the ALA's ultimate load bearing capacities by the half of the corresponding displacements (Figure 2-1). According to ALA, the assumed ultimate load bearing capacities for sand ($c=0$) shown in Figure 2-1 are:

$$P_{ud} = N_q \gamma' H D + 0.5 N_\gamma \gamma D^2 \quad (2-1a)$$

$$P_{uu} = N_{qv} \gamma' H D \quad (2-1b)$$

$$P_{uh} = N_{qh} \gamma' H D \quad (2-1c)$$

$$P_{ua} = 0.5 \pi \gamma' H D (1 + K_0) \tan(f\phi) \quad (2-1d)$$

where, N_q , N_γ , N_{qv} and N_{qh} are bearing capacity factors that are only functions of ϕ and H/D , K_0 is the coefficient of pressure at rest and f is a coating dependent factor that varies from 0.6 to 1 and it is assumed to be 0.8 in this study. Also, the corresponding displacements are:

$$\Delta_d = 0.1D \quad (2-2a)$$

$$\Delta_u = 0.01H < 0.1D \text{ for dense sand} \quad (2-2b)$$

$$\Delta_u = 0.02H < 0.1D \text{ for loose sand} \quad (2-2c)$$

$$\Delta_h = 0.04(H + 0.5D) < 0.10D \text{ to } 0.15D \quad (2-2d)$$

$$\Delta_a = 3 \text{ mm for dense sand} \quad (2-2e)$$

$$\Delta_a = 5 \text{ mm for loose sand} \quad (2-2f)$$

By substituting the assumed soil properties from Table 2-1 and rearranging the variables, non-dimensional stiffness was obtained as function of the normalized burial depth for vertical and horizontal directions (Figure 2-3). Since the axial stiffness arises from a different mechanism (the longitudinal friction between pipe and the surrounding soil), it is only a function of relative pipe-soil displacement and cannot be presented in a non-dimensional form.

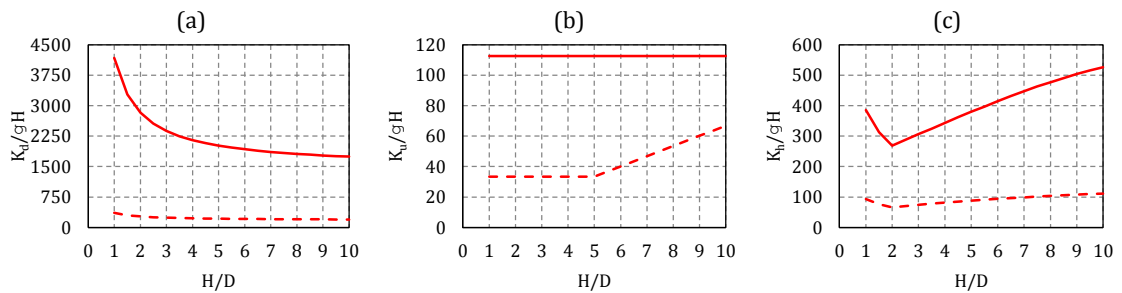


Figure 2-3: Non-dimensional soil stiffness in (a) downward, (b) upward and (c) horizontal directions. H/D is the normalized burial depth. Dense sands are represented with solid line, whereas loose sands are indicated with dashed line.

2.2.2 Modelling and validation

The finite element analyses were carried out using the Abaqus/CAE software (Dassault systemes 2007). The pipe was discretized by S4 general-purpose shell elements and the considered mesh size was first evaluated using the response results of in-air steel pipes tested by Limam et al. (2010) in a laboratory setup under pure bending and internal pressure ($D=38.15$ mm, $t=0.737$ mm, $D/t=52$, $L/D=7.3$, $E=186$ GPa, $\sigma_y=227$ MPa). To optimize the mesh refinement, a sensitivity analysis was conducted in which the pipe circumference was divided into 16, 24 and 32 square S4 elements. The former was not precise enough and the latter did not notably improve the results over those obtained using 24 elements. Therefore, the pipe circumference was divided into 24 square S4 elements and only half of the span was modeled due to symmetry. Boundary conditions and loading are shown in Figure 2-4a where the left end of the pipe model is on the plane of symmetry and the right end is under rotation.

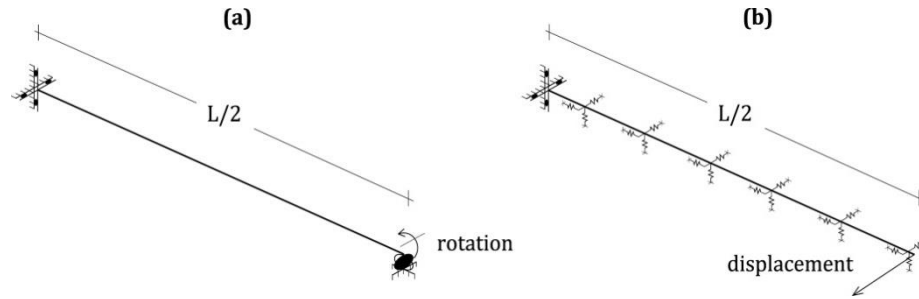


Figure 2-4: Boundary conditions of (a) the in-air pipe and (b) the buried pipe.

Figure 2-5 compares the obtained results and the numerical simulations of Limam et al. In Figure 2-5, the simulated ovalization (OV) is plotted against normalized curvature (K) for three magnitudes of normalized internal pressure (P), which are defined as:

$$P = \frac{p(D-t)}{2\sigma_y t} \quad (2-3a)$$

$$OV = \frac{\Delta D}{D} \quad (2-3b)$$

$$K = \frac{\kappa(D-t)^2}{t} \quad (2-3c)$$

where, ΔD is the change of pipe diameter in the plane of bending, D is the outer pipe diameter, κ is curvature in the critical section, t is the wall thickness, p is the internal pressure and σ_y is yield stress. As it can be seen from Figure 2-5, there is a good agreement between results of the two studies for the considered mesh size.

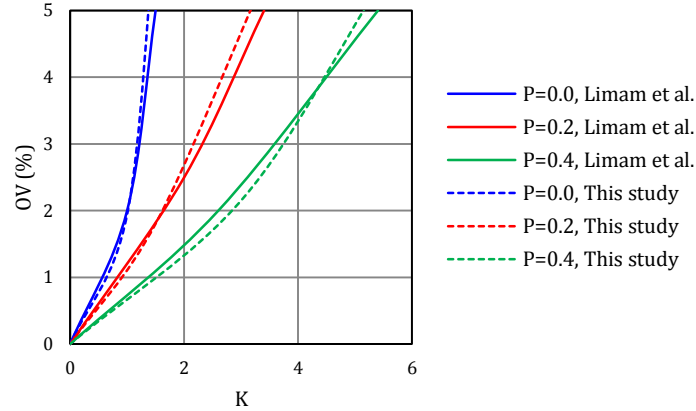


Figure 2-5: Numerical results of the current study compared to those presented by Limam et al. (2010). P is normalized internal pressure, OV is ovalization factor, and K is normalized curvature, defined by Equations (2-3).

After validation of the pipe mesh size, the finite element model of the buried pipe was developed by adding the ALA's soil-pipe interaction springs to the proper nodes as discussed in Section 2.3.1. The modelling strategy was based on the experimental study of Konuk et al. (1999) in which quasi-static displacements were applied to the ends of the pipes buried in dense sand. The pipe length in this study was 4 meters, however due to symmetry only half of the span was modeled by considering appropriate displacement boundary conditions as illustrated in Figure 2-4b. It was assumed that the pipe is made of X65 steel and stress-strain relationship is defined by the Ramberg-Osgood equation (Ramberg and Osgood 1943):

$$\varepsilon = \frac{\sigma}{E} \left[1 + \frac{3}{7} \left(\frac{\sigma}{\sigma_y} \right)^{n-1} \right] \quad (2-4)$$

where, $E=210$ GPa, $\sigma_y=448$ MPa and $n=9.3$. Each analysis was performed in three consecutive steps: applying vertical soil surcharge loading to the top of the pipe, pressurizing inside the pipe (if it is supposed to be under internal pressure) and inducing the lateral end displacements.

2.2.3 Parametric analysis

Following the satisfactory modelling results, a sensitivity analysis was conducted to investigate the importance of different parameters on the pipe response. A series of simulations was performed varying the diameter to thickness ratio (D/t), normalized burial depth (H/D), internal pressure and soil density as key parameters (Figure 2-6). Two basic D/t ratios of 18 and 86 representing thick- and thin-walled energy pipeline categories respectively (based on slenderness parameter introduced by Sherman (1986)), were considered. In the further text, these pipes are referred to as pipe “A” and pipe “B”, respectively. The normalized burial depth was varied between shallow ($H/D=1$) and deep ($H/D=10$) pipelines as bounds of practical range. By increasing the internal pressure, the hoop stress was gradually increased from 0 to 80% of the specified minimum yield strength (SMYS) as the maximum value allowed by the CAN-CSA Z662 code. The parameters that were considered in the parametric study performed for this research are summarized in Table 2-2. In all of the cases $D=38.15$ mm.

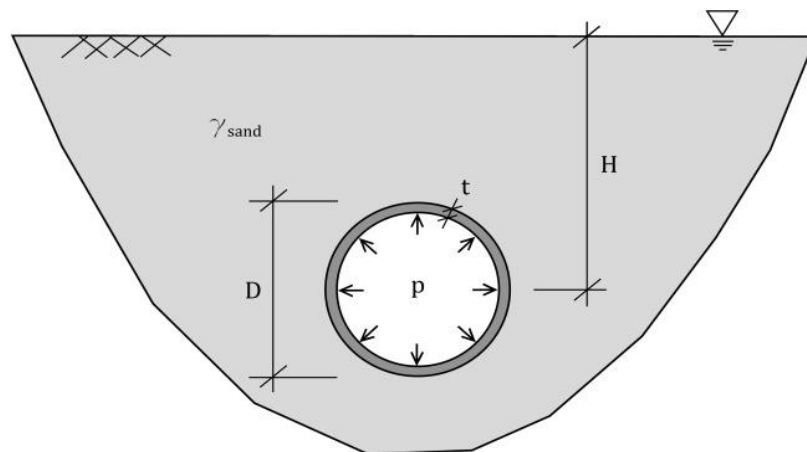


Figure 2-6: Key parameters that formed nondimensional variables in the analyses (H/D , D/t and P).

Table 2-2: Parameters considered in parametric study.

Depth*/Soil density	Pipe diameter	Pipe type**	Displacement direction	P
Shallow/Loose (SL)	D=38.15 mm	A, B	Horizontal, Vertical	0
Shallow/Dense (SD)	D=38.15 mm	A, B	Horizontal, Vertical	0
Deep/Loose (DL)	D=38.15 mm	A, B	Horizontal, Vertical	0
Deep/Dense (DD)	D=38.15 mm	A, B	Horizontal, Vertical	0
Deep/Dense (DD)	D=38.15 mm	A, B	Horizontal	0.1, 0.2, 0.4, 0.8

*Shallow: H/D=1, Deep: H/D=10

**Type "A": D/t=18, Type "B": D/t=86

2.3 Results

2.3.1 Nondimensionalization

All results in this section are presented in terms of non-dimensional parameters in order to facilitate extrapolation to other pipeline configurations and mechanical properties. The normalized bending moment M is thus defined as:

$$M = \frac{m}{\sigma_y(D-t)^2t} \quad (2-5)$$

where, m is bending moment in the critical section. The corresponding ovalization factors in the horizontal (OV_h) and vertical (OV_v) directions are defined as the ratio between the simulated deformations in the respective horizontal and vertical directions and the pipe outer diameter D as follows:

$$OV_h = \frac{\delta u + \delta d}{D} \quad (2-6a)$$

$$OV_v = \frac{2\delta h}{D} \quad (2-6b)$$

In Equations (2-6), the vertical deformation is given as the sum of the simulated downward and upward displacements, i.e., δd and δu , whereas the horizontal deformation is double of the horizontal displacement, δh (Figure 2-2).

2.3.2 Unpressurized pipelines

Figure 2-7 presents the variation of bending moment and ovalization factor with curvature for pipe type "A" ($D/t=18$). Two types of the ultimate conditions can be observed in Figure 2-7: soil failure and pipe collapse which have occurred mostly in the cases of shallow and deep burial depths, respectively. In Figure 2-7, as a convention, the former

instability is indicated by horizontal arrow, whereas the latter is presented by vertical arrow and slope of the arrows does not represent the slope change in M-K curves. Beyond these points, in the case of soil failure, the bending moment, the ovalization factor and the curvature remain constant (for the considered length of pipeline) while in the case of pipe collapse, the corresponding ovalization starts a rapid ascending phase and shortly after, the pipe collapses due to excessive cross-sectional deformations (progressive ovalization). Under both horizontal and vertical end displacements, moment-curvature plots of the buried and in-air pipes are coincident (Figures 2-7a and b) though the ultimate moments/curvatures and ovalization curves are different (Figures 2-7c and d). As can be seen from Figures 2-7a and b, generally the ultimate moment and the corresponding curvature of the buried pipes have decreased compared to the in-air case. Although the moment capacity has decreased only up to 14%, the ultimate curvature, an indicator of ductility, has dropped up to 78%. The only exception is observed where the pipe was buried deeply in the dense sand (DD) and displaced downward. In this case, the lateral soil confinement was extremely large compared to the other cases and prevented the cross-section from experiencing excessive ovalization. Consequently, both the moment capacity and the ductility of the pipe increased compared to the other buried cases, yet they are not larger than the in-air case.

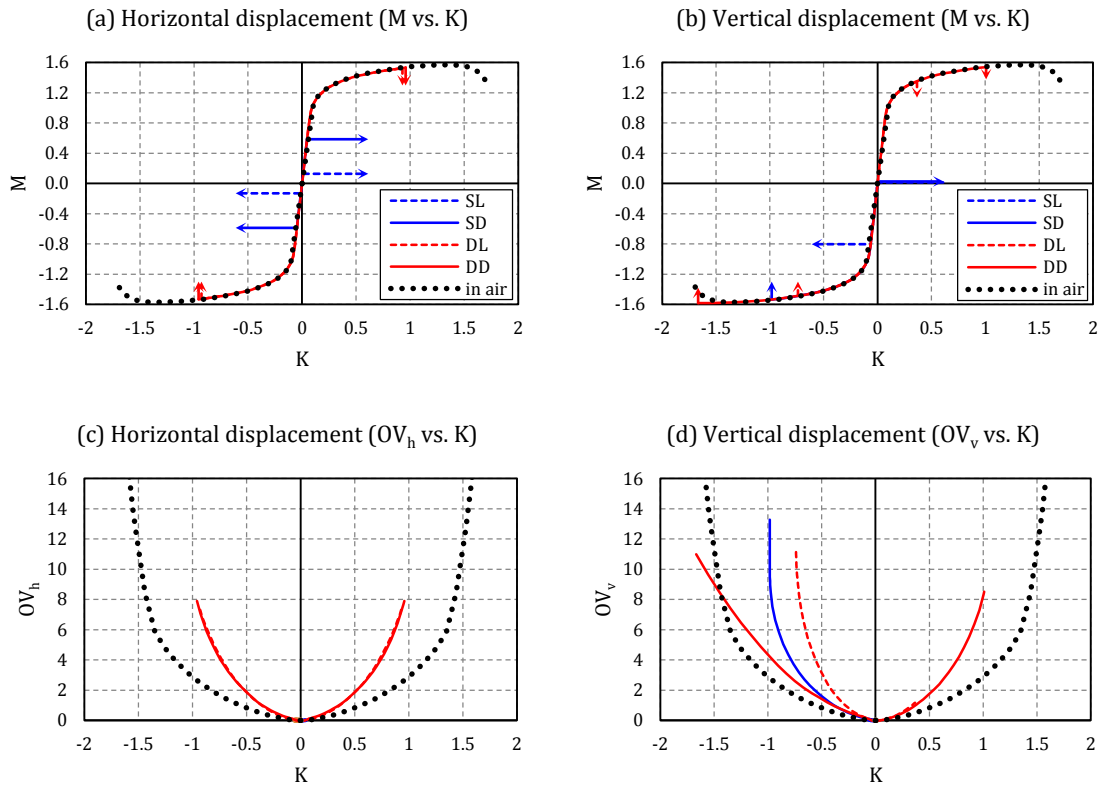


Figure 2-7: Simulated horizontal and vertical displacements for pipe type “A” ($D/t=18$). SL and SD indicate pipes buried at shallow depths in loose and dense sandy soil, respectively (blue solid and dotted lines); DL and DD indicate pipes buried deeply in loose and dense sandy soil, respectively (red solid and dotted lines) Black dotted line indicates response of above-ground pipe (in-air). Soil failure is indicated by horizontal arrow, whereas pipe collapse is presented by vertical arrow and slope of the arrows does not represent the slope change in M-K curves.

To prevent from progressive ovalization failure or fluid conveying dysfunction, most of the design codes limit the cross-sectional ovalization; for example, ALA considers 15% as the maximum allowable ovalization factor. As it can be seen from Figures 2-7c and d, the ALA’s limit only works for the in-air pipe and for the buried pipes unsafe overestimates their capacity. The soil stiffness that directly resists against pipe displacement (direct stiffness) intensifies the ovalization, whereas the one that acts in the perpendicular direction (confining stiffness) provides confinement and opposes

cross-sectional deformations. The absolute and relative direct and confining stiffness values control the capacity of a buried pipe by affecting the cross-sectional ovalization.

The moment-curvature and ovalization-curvature curves are asymmetric for the vertical end displacements due to differences in the upward and downward soil bearing capacities. However, in the cases of deep normalized burial depths (DL and DD) both the upward and downward pipe movements give almost the same maximum bending moment (Figure 2-7b).

The corresponding results for the pipe type “B” ($D/t=86$) are depicted in Figure 2-8. The two mentioned failure mechanisms are observed again. However, for this type of pipe (with a large D/t) local buckling causes instability rather than progressive ovalization. Moment-curvature plots of in-air and buried pipes coincide in the linear range while beyond that some differences between the curves can be seen which emphasize that the density of the surrounding soil is more important in the flexural behaviour of this slender pipe than it is the case with pipe type “A”. Variation of moment-curvature in the nonlinear range is a result of large cross-sectional deformations caused by direct and confining stiffness of the soil.

In contrast to the pipe type “A”, pipe burial is beneficial in most conditions of depth and soil density. According to Figures 2-8a and b, in most cases the bending capacity and ductility have increased. For example up to 14 and 33% increase in the ultimate bending and curvature was observed in the upward displacement of a pipe buried deeply in the sand (DD). On the other hand, there are some exceptions in which the pipe bending capacity has reduced compared to the in-air and other buried cases. The direct soil stiffness in these cases is large enough to cause buckling instability. Again, in the cases of deep normalized burial depths, both the upward and downward pipe movements induced almost the same level of bending moment, but different levels of curvature (Figure 2-8b).

From Figures 2-8c and d, it is clearly seen that the ALA’s 15% ovalization limit is not satisfied for the buried pipes though the flexural capacity has generally increased.

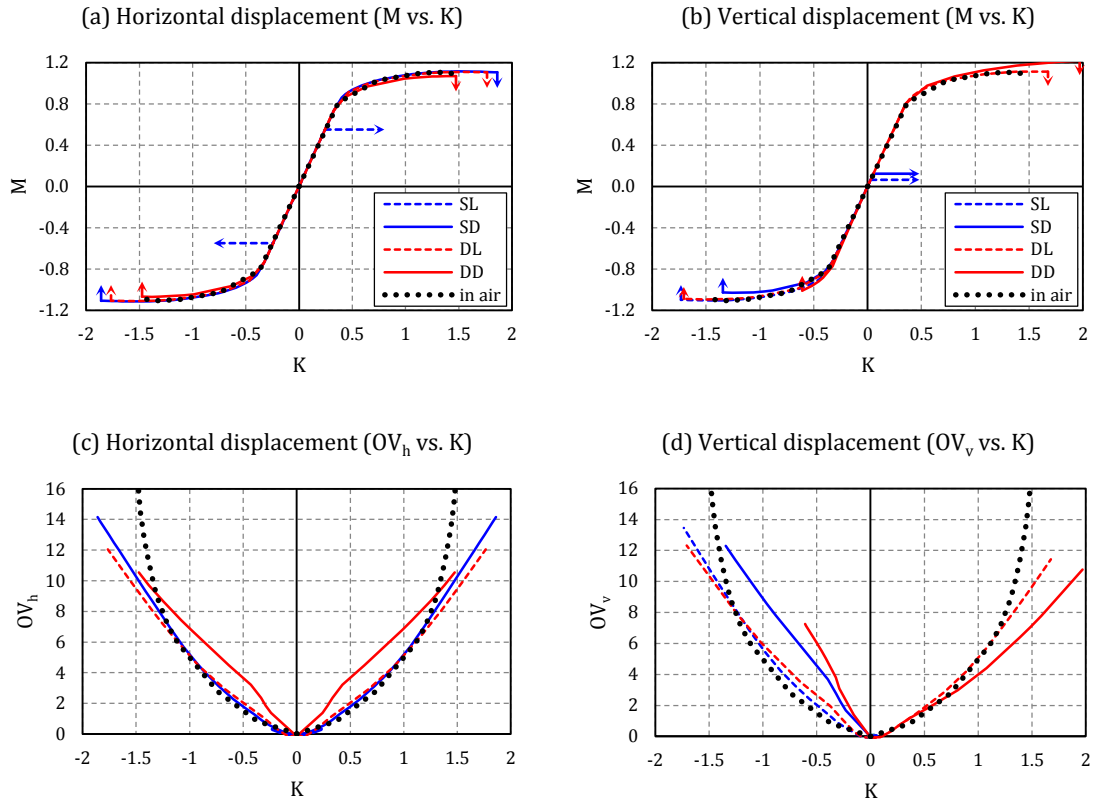


Figure 2-8: Simulated horizontal and vertical displacements for pipe type “B” ($D/t=86$). SL and SD indicate pipes buried at shallow depths in loose and dense sandy soil, respectively (blue solid and dotted lines); DL and DD indicate pipes buried deeply in loose and dense sandy soil, respectively (red solid and dotted lines) Black dotted line indicates response of above-ground pipe (in-air). Soil failure is indicated by horizontal arrow, whereas pipe collapse is presented by vertical arrow and slope of the arrows does not represent the slope change in M-K curves.

As mentioned before, for the considered pipe length two types of failure mechanisms were observed in the pipeline-soil system: soil failure or local instability of the pipe wall. When the soil bearing capacity and its stiffness are relatively small compared to the flexural stiffness of the pipe (i.e., either the soil is loose or the pipe is stiff), the soil provides weak resistance to the deformations induced by the pipeline and yields at the early stages of loading. With the increase of the end displacement, the soil first starts yielding in the vicinity of the extremities and the yield zone expands toward the middle of

span. As soon as yield zone extends along the whole pipe span, the pipeline-soil system becomes unstable and the bending moment distribution remains constant along the span. The maximum bending moment value is directly related to the density of the confining soil and the length of the pipeline subjected to the end displacements. On the other hand, the pipe failure occurs when the surrounding soil has considerable stiffness and bearing capacity. In this case, the soil yields only along two zones located at the end of the pipe, with the pipe instability regarded as a plastic hinge, occurs at the beginning of the mentioned zones.

To indicate the length of yielded zone in each case, the soil yield index (SYI) was defined as:

$$SYI = \frac{2L_y}{L} \quad (2-7)$$

where, L_y is the length of the yielded zone and L is the total length of the pipe. SYI is smaller than 1 unless the soil yields before the collapse of the pipe in which $L_y=L/2$ and SYI becomes 1. SYIs for the studied cases are shown in Figure 2-9. As it can be seen, for the type “A”, the indexes are generally larger than those of the type “B” and also, the cases in which the soil became unstable first (SYI=1), can be easily detected.

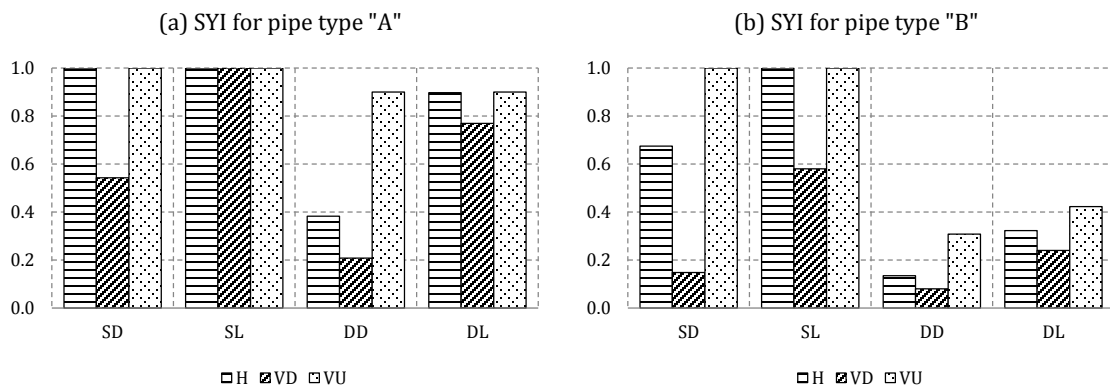


Figure 2-9: Soil yield index (SYI) for (a) pipe type “A” and (b) pipe type “B”. H, VD and VU denote horizontal, downward and upward end displacements, respectively.

To study the effect of length on the behaviour of the cases in which the soil yielded prior to collapse of pipe, a parametric study was performed for the cases subjected to horizontal

end displacement. For the type “A” buried in the loose and dense sands (SL and SD), L/D was changed from 105 to 786. The maximum bending moments (M) attained were 0.74 in L/D=577 and 0.83 in L/D=210 for loose and dense sands, respectively which means the pipes were only entered the nonlinear range and again soil yielded. However, the pipes were subjected to larger moments compared to the cases with L/D=105.

For the type “B” buried in the loose sand (SL), L/D was increased from 105 to 152 and the pipe reached to its peak bending capacity in L/D=152 and collapsed at M=1.10.

2.3.3 Pressurized pipelines

Based on CAN-CSA Z662, hoop stress in the pipe wall caused by the internal pressure is allowed to be as high as 80% of the SMYS. In the present study, the beneficial effect of the internal pressure on pipe failure was checked by gradually increasing the internal pressure from 0 to 80% of the SMYS. The same pipe types “A” and “B” as in the previous section are considered. For each numerical analysis, following the gravity loading, the internal pressure was increased and end displacements were applied. The pipe was assumed buried in dense sand with normalized depth H/D=10 due to the fact that for a large burial depth pipe failure governs. The simulated ovalization results just before the onset of instabilities are shown in Figure 2-10.

As can be seen from Figure 2-10a, compared to the pipe under zero internal pressure, bending capacity of the pipe type “A” has increased under low to moderate internal pressures (10-40% SMYS), whereas under high internal pressure (80% SMYS) it has drastically decreased. Also, it can be observed that the capacity ascends by increasing the internal pressure up to 20% SMYS and beyond that level, descends.

The increase of the internal pressure leads to an increase in the tension hoop stress in the pipe circumference. According to the Von Mises yield criterion for a bidirectional stress condition in the pipe wall, an increase of the tension hoop stress results in a reduction in the longitudinal compression stress capacity (Figure 2-11) where the longitudinal stress is induced by flexure. Consequently, in the pressurized pipes under flexure, yield occurs earlier compared to the unpressurized ones.

Furthermore, the ovalization factor at the critical section (Figure 2-10c) shows a similar trend under low, moderate and high pressures. The increase of the ultimate capacity in low pressures can be related to the stabilizing effect of internal pressure that tends to preserve the initial circular shape of the cross-section. In moderate and high pressures, large hoop stresses combined with small flexural compression stresses causes yield in a large portion of the circumference. As a result, the stiffness of the pipe wall drops in this region and the passive pressure exerted by the soil counterbalances the cross-section stability resulting from the internal pressure (Figure 2-11). Only, the pipe under internal pressures of 10% and 20% SMYS can reach the ALA's allowable ovalization factor (15%).

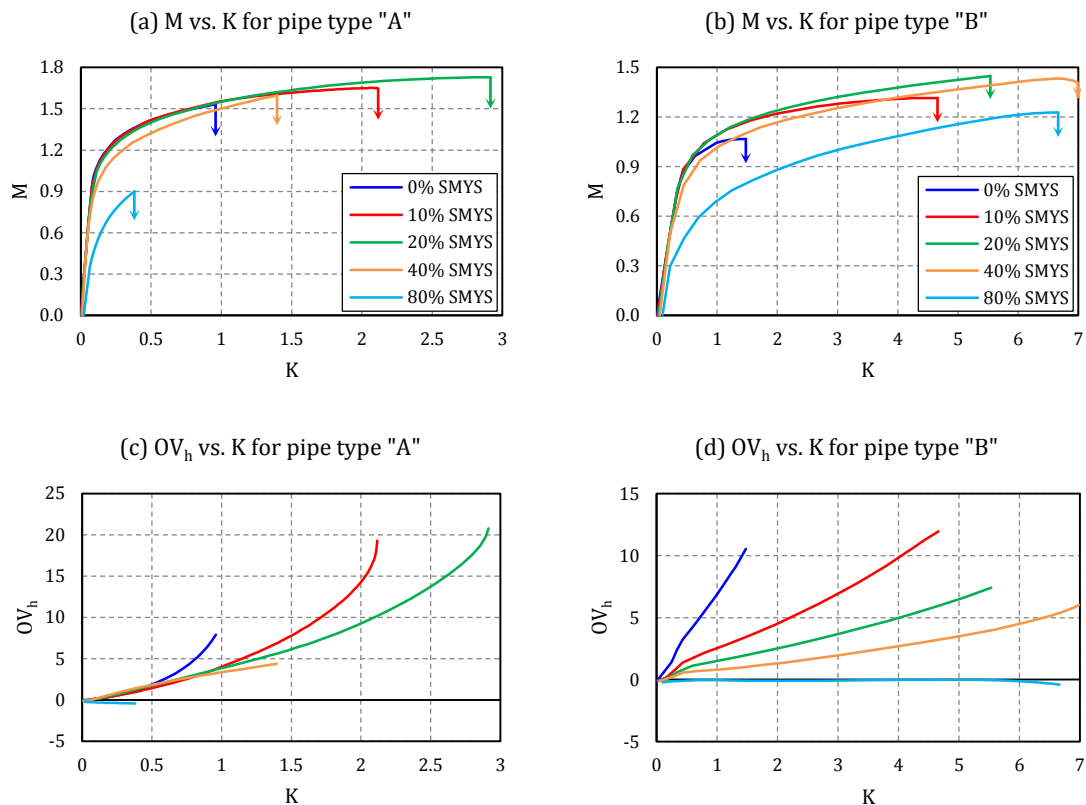


Figure 2-10: Ovalization of deep pipe ($H/D=10$) buried in dense sand for horizontal end displacement, (a) pipe type "A" ($D/t=18$) moment-curvature, (b) pipe type "B" ($D/t=86$) moment-curvature, (c) pipe type "A" ovalization-curvature and (d) pipe type "B" ovalization-curvature. Different levels of hoop stress in the pipe circumference are presented as percentages of SMYS.

The same curves for the pipe type “B” are presented in Figures 2-10b and d. In these figures, the ultimate flexural capacity under all levels of pressures has increased compared to the unpressurized case. However, for pipes subjected to higher internal pressures the ultimate flexural capacity shows lower values than for cases with lower internal pressure. The effect of the internal pressure on cross-sectional ovality is clearly observed as the increase of the internal pressure is accompanied by reduction of the out-of-roundness at the critical section. Similar behaviour can also be observed in Figure 2-10a. Thus, since the Brazier effect in the pipes with low D/t is insignificant, the results are less scattered. In other words, slender pipes with high D/t (pipe type “B”), show reduced out-of-roundness of the cross-section and increased flexural capacity even for small increase of the internal pressure. This, however, is not the case for more rigid pipes with low D/t (pipe type “A”) whose flexural capacity is considerably less sensitive to the variation of the internal pressure. At the same time, the level of critical ovalization just before the onset of instabilities in pipe type “B” subjected to all of the internal pressure levels is still lower than the ALA’s limit value (15%).

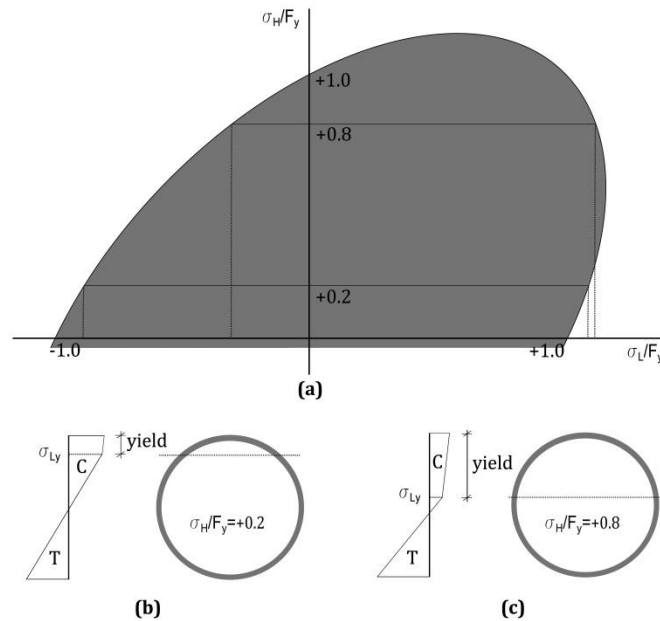


Figure 2-11: (a) Von Mises yield criterion, and approximate flexural stress distribution under (b) low and (c) high internal pressures.

2.4 Conclusions

Flexural behaviour and corresponding ovalization of buried pressurized and non-pressurized steel pipelines subjected to end displacement were studied. Non-dimensional stiffness functions were developed for saturated loose and dense sands based on the bilinear load-displacement curves suggested by ALA and CAN-CSA Z662. The loose and the dense sands were regarded as the lower and upper bounds of soil confinement with respect to vertical and lateral pipeline deformations. The flexural behaviour of hollow steel tubes was analyzed considering practical ranges of the diameter to wall-thickness ratio, D/t , between 18 (pipe type “A”) and 86 (pipe type “B”). Numerical modelling was conducted using Abaqus/CAE and was validated based on results obtained from laboratory experiments reported in the literature. Typical non-dimensional relationships between the bending moment and resulting ovalization for buried pipes were generated from 3D finite element analyses. The non-dimensional relationships can easily be extrapolated to other pipeline configurations and mechanical properties. The following conclusions can be drawn based on the obtained results:

- Two collapse mechanisms are identified: soil failure and pipe failure. The soil density and pipe flexural rigidity (function of D/t) are important factors that control failure mechanism of the soil-pipe system.
- Moment-curvature of non-pressurized type “A” pipes under horizontal and vertical deformations resembles to that of the in-air. The magnitude of the induced maximum bending moment and the corresponding curvature depends on the density of the surrounding soil and on the normalized burial depth. On the other hand, variation of moment-curvature for the type “B” is more sensitive to the density of soil and is different from that of the in-air. Generally, flexural capacity of the type “A” drops when it is buried, in contrast to the type “B” that its capacity increases when it is surrounded by soil. In none of the cases the cross-sectional ovalization reaches to the maximum allowable values determined by ALA and the pipe collapses earlier.

- Maximum bending moments in unpressurized pipes caused by vertical deformations in upward and downward directions are different as the soil stiffness and bearing capacity vary.
- Flexural behaviour of pressurized buried pipes is highly dependent on D/t and the level of internal pressure. Since the Brazier effect in pipes type “A” with low D/t is insignificant, the ovalization results are less scattered when compared to those of the pipe type “B”. Even a small increase in the internal pressure can reduce out-of-roundness of the cross-section of slender pipes of type “B”, and increase their flexural capacity considerably, which is not the case for pipe type “A”.
- The 3D finite element modelling using shell elements is rigorous but requires considerable computational time. The results of this study, however, enable simple beam finite elements to determine ovalization and predict local instabilities in buried pipelines with a lower computational cost.

Although the developed numerical model was partly validated against a few reported laboratory tests, it is necessary to conduct systematic experiments and validation to get better insight in the pipe response in the future studies. All findings of this study are applicable to the cases when the modelling assumptions are valid.

References

Abaqus 6.7 User Documentation. Dassault Systèmes, 2007.

Ades, C. S. "Bending strength of tubing in the plastic range." *Journal of Aeronautical Sciences* 24, no. 8 (1957): 605-610.

Guideline for the design of buried steel pipe. American Lifelines Alliance, 2001.

Bouwkamp, J. G., and R. M. Stephen. "Large diameter pipe under combined loading." *Transportation Engineering Journal (ASCE)* 99 (TE3) (1973): 521-536.

Brazier, L. G. "On the flexure of thin cylindrical shells and other "thin" sections." *Proceedings of the Royal Society of London, Series A 116*. London, 1927.

BS8010: Code of practice for pipelines - part 3: pipelines subsea, design, construction, installation. London: British Standards Institute, 1993.

CSA Z662-03 oil and gas pipeline systems. Mississauga, ON: Canadian Standards Association, 2003.

Gresnigt, A. M. "Plastic design of buried steel pipelines in settlement areas." *HERON* 31, no. 4 (1986): 3-113.

Houliara, S., and S. A. Karamanos. "Buckling and post-buckling of long pressurized elastic thin-walled tubes under in-plane bending." *International Journal of Non-Linear Mechanics* 41 (2006): 491-511.

Kim, H. O. "Plastic buckling of pipes under bending and internal pressure." *The second international offshore and polar engineering conference*. San Francisco, 1992.

Konuk, I., R. Phillips, S. Hurley, and M. J. Paulin. "Preliminary ovalisation measurements of buried pipelines subjected to lateral loading." *18th conference on offshore mechanics and arctic engineering*. St. Johns, 1999.

Limam, A., L. H. Lee, E. Corona, and S. Kyriakides. "Inelastic wrinkling and collapse of tubes under combined bending and internal pressure." *International Journal of Mechanical Sciences* 52 (2010): 637-647.

Mahdavi, H., S. Kenny, R. Phillips, and R. Popescu. "Significance of geotechnical loads on local buckling response of buried pipelines with respect to conventional practice." *Canadian Geotechnical Journal* 50 (2013): 68-80.

Murray, D. W. "Local buckling, strain localization, wrinkling and postbuckling response of line pipe." *Engineering Structures* 19, no. 5 (1997): 360-371.

- Nixon, J. F., K. A. Sortland, and D. A. James. "Geotechnical aspects of northern gas pipeline design." *Proceedings of the fifth Canadian permafrost conference*. Quebec City, 1990.
- O'Rourke, M., and G. Ayala. "Pipeline damage due to wave propagation." *Journal of Geotechnical Engineering* 119, no. 9 (1993): 1490-1498.
- Oswell, J. M. "Pipelines in permafrost: geotechnical issues and lessons." *Canadian Geotechnical Journal* 48 (2011): 1412-1431.
- Ramberg, W., and W. R. Osgood. *Description of stress-strain curves by three parameters*. Washington DC: Technical Note No. 902, National Advisory Committee For Aeronautics, 1943.
- Schaumann, P., C. Keindorf, and H. Bruggemann. "Elasto-plastic behavior and buckling analysis of steel pipelines exposed to internal pressure and additional loads." *24th International conference on offshore mechanics and arctic engineering*. Halkidiki, 2005.
- Schilling, C. G. "Buckling strength of circular tubes." *Journal of Structural Division (ASCE)* 91 (1965): 325-348.
- Sherman, D. R. "Inelastic flexural buckling of cylinders." *International Conference on Steel Structures, Recent Research Advances and Their Application to Design*. Amsterdam, 1986.
- Sherman, D. R. "Tests of circular steel tubes in bending." *Journal of Structural Division (ASCE)* 102 (1976): 2181-2195.
- Xie, X., et al. "Numerical modeling of buried HDPE pipelines subjected to normal faulting: a case study." *Earthquake Spectra* 29, no. 2 (2013): 609-632.

Chapter 3

3 Experimental and analytical study of seismic site response of discontinuous permafrost²

3.1 Introduction

Surface seismic ground motions are significantly influenced by local site conditions, e.g., surficial soil or bedrock conditions, depth and geometry of the sedimentary basin, topography, and by the characteristics of the incoming seismic waves. These parameters modify the amplitude, frequency content and duration of the bedrock motion in such a way that bedrock and surface motions are incoherent. The impact of these parameters on seismic site response is referred to as local site effects. In discontinuous permafrost regions, site effects can be accentuated by the intermittent presence of frozen soils. Permafrost or perennially frozen ground is a term used to describe the thermal condition of soils when their temperature remains continuously below 0°C for a number of years (Muller 2008). In the discontinuous zone, some portions of the soil mass are under frozen conditions whereas others are not. Discontinuous permafrost represents a particular challenge for geotechnical earthquake engineering because frozen soils have different geotechnical properties and relatively higher shear wave velocities than unfrozen soils. The relatively high impedance contrast between frozen and unfrozen soils in the lateral and/or vertical directions may contribute to important site effects.

Only a limited number of studies considering the effects of permafrost on free-field ground motion are found in the literature. These are mainly recent studies conducted in response to infrastructure developments in cold regions, mostly transportation systems and energy pipelines. Among the first studies is the investigation conducted by Finn and Yong (1978) and Finn et al. (1978), which focused on the seismic behaviour of frozen soils and liquefaction mechanisms in thawed layers. The authors concluded that the simultaneous presence of frozen and unfrozen soils increases the complexity of the free-field ground motion, in particular saturated unfrozen cohesionless soils sandwiched between a frozen surficial layer and underlying permafrost that could potentially cause

² A version of this chapter has been published in the Canadian Geotechnical Journal 53 (2016) 1-13.

ground instabilities during earthquakes. Characterization of ground motions at permafrost sites along the Qinghai-Tibet railway, China, was carried out by Wang et al. (2009). They conducted numerical simulations employing synthetic input seismic motions with different exceedance probabilities to investigate the influence of ground temperature on free-field ground motion parameters (acceleration, velocity, displacement and predominant period). Yang et al. (2011) performed one-dimensional (1D) equivalent linear analysis of vertically propagating horizontal shear waves in order to investigate the effects of permafrost on the seismic response of bridges in Alaska. The effects of variations in permafrost thickness and depth, and depth to bedrock were studied. They concluded that the presence of continuous permafrost changes the ground motion and should be considered in seismic design of structures.

All cited site response studies investigated the dynamic behaviour of frozen soils under continuous permafrost conditions. To date, however, there is no numerical or experimental published research (to the best of our knowledge) focusing on the soil dynamic behaviour under discontinuous permafrost conditions.

The objective of this chapter is to fill in the current knowledge gap related to the seismic site response under complex discontinuous permafrost conditions by conducting experimental and numerical analyses. Particular attention was given to the dynamic interaction between the portions of frozen soil and surrounding unfrozen soil, as shown in Figure 3-1. Nonlinear models were developed and validated against laboratory tests and a sensitivity analysis was conducted. The calibrated models were then used to run parametric studies in an effort to quantify the interaction. The findings of this study are important for the safety of infrastructure in discontinuous permafrost regions.

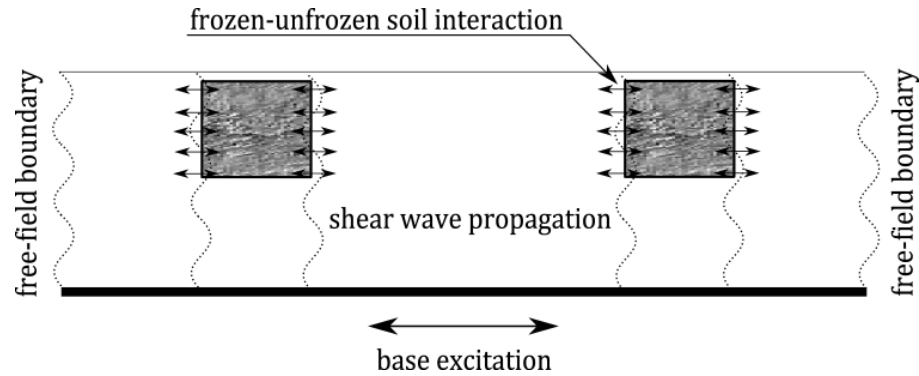


Figure 3-1: Dynamic interaction between frozen soil blocks (in gray color) and the surrounding unfrozen soil.

3.2 Physical modelling with reduced-scale 1g shaking table tests

The scaling relations map geometry, kinematics and dynamics of prototypes to those of models. They can be established by dimensional analysis, similitude theory and the method of governing equations (Kline 1965). As it is usually not feasible to fulfill all the similitude requirements, it is preferred to satisfy as many relations as possible giving priority to those relevant to the desired aspects of the problem. Based on the level of similarities, the model can be referred to as “true”, “adequate” or “distorted” where, the true model has the highest level of similarity and the distorted model has the lowest (Moncarz and Krawinkler 1981).

Shaking table tests in a 1g gravitational field are useful tools for studying the behaviour of soils and structures under seismic loading. Full-scale models on a shaking table can “truly” simulate the prototype response. Small-scale models, on the other hand, depending on the degree of satisfaction of the scaling relations, can predict the response quantitatively or qualitatively.

The constitutive behaviour of soil affects considerably the ground deformations. In dynamic problems, the undrained constitutive behaviour of cohesionless soils depends on the confining pressure and density. Due to the smaller confining pressures in the model soils, the stress-strain relations of prototype and model may become different when identical soil densities are considered (contractive and dilative behaviours). Verdugo and

Ishihara (1996) demonstrated this effect conducting undrained tests on Toyoura sands with different void ratios and confining pressures. Rocha (1957) presented similarities under total and effective stress conditions for problems involving elastic deformations. The author proposed scaling of the soil constitutive model according to the stress and strain scales. Considering Rocha's assumptions, Iai (1988) further derived scaling relations for soil-structure-fluid modelling in the elastic range. To deal with soil nonlinearities such as large deformations during liquefaction, Roscoe (1968) applied concepts of critical state soil mechanics and expressed the conditions of similarity based on the state parameters of prototype and model soils. The theoretical developments were with a few experiments. Towhata (2008) used the experimental results of Verdugo and Ishihara (1996) and Vargas-Monge (1998) to extend the similarity relationships within the full range of soil nonlinearity. To this end, the concept of brittleness index (Bishop et al. 1971) was suggested in replication of the strain softening of the constitutive model. Based on this approach it is not necessary to satisfy the similarity of the soil density and a looser soil can simulate the stress-strain relation of the prototype. However, to date there are no definitive scaling relations for the density of sand in the scaled models (Alam and Towhata 2008).

The primary goal of this research is to study the soil-permafrost interaction which depends heavily on the stiffness of both media expressed with respective shear wave velocities. It was therefore decided to keep constant the dimensionless ratios of the shear wave velocities of frozen and unfrozen materials measured in the field and in the scaled model. The primary simulation condition is satisfied when applying the field soil density in the model. However, introducing loose soils to satisfy the secondary effects of liquefaction will violate the primary similarity. In addition, preparing saturated experimental models consisting of a combination of high density material (representing permafrost) and low-density soil (representing unfrozen soil) is technically difficult. Therefore, the scaling relations of Iai (1988) were preferred to produce "adequate" scaled models with a primary focus on the soil-permafrost interaction.

3.2.1 Scaling relations

Similitude relations developed by Iai (1988) for reduced-scale models of saturated soil-structure-fluid interaction tests at a 1g gravitational field were used in this study. By satisfying the basic equations of the saturated soil-structure-fluid system for both the model and prototype, Iai obtained scaling relations. The basic equations were derived assuming that the soil skeleton is a continuum and the soil displacements and skeleton strains are small. He showed that the similitude relations give good approximation for seismic deformations of the prototype soil-structure. The applied similitude relations and corresponding scaling factors are shown in Table 3-1.

As can be noted from Table 3-1, only two of the scaling factors are independent, i.e., the length and density scale factors (λ_L and λ_ρ), whereas the remaining factors are related to one or both of them. Considering the capabilities of the available experimental facility and some additional technical considerations explained below, the appropriate scale factors for the length and density were selected to be 100 and 1, respectively.

Table 3-1: Scale factors for 1g shaking table tests on soil-structure-fluid models (Iai 1988).

Item	Scaling factor*	Value
Length	λ_L	100
Density	λ_ρ	1
Strain	$\lambda_L^{0.5}$	10
Time	$\lambda_L^{0.75}$	31.6
Stress	$\lambda_L \lambda_\rho$	100
Shear modulus	$\lambda_L^{0.5} \lambda_\rho$	10
Displacement	$\lambda_L^{1.5}$	1000
Velocity	$\lambda_L^{0.75}$	31.6
Acceleration	1	1
Frequency	$\lambda_L^{-0.75}$	0.03
Pore fluid viscosity	$\lambda_L^{-0.75} \lambda_\rho$	0.03
Shear wave velocity	$\lambda_L^{0.25}$	3.16

* Item in prototype divided by the same item in model

3.2.2 Shaking table and soil container

The shaking table tests were conducted on soil models enclosed in a laminar soil container placed on a 1.22 m × 1.22 m 1D shaking table at The University of Western Ontario, Canada. The shaking table can be excited by either an electrical or hydraulic actuator controlled by a digital control module, which allows simulation of various types

of dynamic displacement time-histories. In this study, an electrical actuator was used because of the high frequency range of the scaled input motion. The electrical actuator has a maximum displacement stroke of 12 mm and can generate up to 3 kN base shear within the broad frequency range of 1-150 Hz. Scaled records of the El Centro Earthquake (1940) were used as an input motion at the base of the shaking table. Each model was excited by three levels of shaking intensity: low (PGA=0.15g), medium (PGA=0.3g) and high (PGA=0.5g). The original duration of the record was 30 sec, which in accordance with the similitude relation for time was reduced approximately to 1 sec (Table 3-1).

The infinite boundaries in the prototype and the 1D vertical shear-wave propagation were simulated by containing the soil models in a laminar (flexible) soil container that does not impose unrealistic rigid boundary conditions and reduces the reflection of the dynamic waves back into the box. The laminar container comprised 12 horizontal lamina supported individually on linear bearings and steel guide rods connected to an external frame as shown in Figure 3-2. The inner dimensions of the container are 404 mm, 900 mm and 450 mm corresponding to the height, length and width, respectively. The laminar container does not have a bottom plate, allowing the soil to rest on the shaking table directly. Further details about specifications and fabrication of this container can be found in Turan et al. (2009). The test setup included the shaking table, flexible container, electric control module, and data acquisition system, which are shown in Figure 3-2.



Figure 3-2: Test setup including (from left to right): data acquisition system, the electric control module, shaking table with the mounted flexible container with 12 frames; and sand-cement blocks representing frozen soils.

3.2.3 Material properties and preparation

Sand: North America permafrost is often formed of cohesionless soils (Finn and Yong 1978). For this study, the soil types and stratigraphy were selected based on the information in the borehole database of the Yukon-Alaska highway and of the pipeline projects along the Mackenzie Valley-Delta region in Canada and the USA (Yukon Geological Survey 2014, and Geological Survey of Canada 2014). Both project routes pass through regions with predominantly discontinuous permafrost conditions. To simulate the field soil conditions, a simplified soil profile consisting of uniformly-graded sand (Ottawa sand) underlain by better-graded sand (construction sand) was considered. The respective gradation curves and geotechnical parameters are shown in Figure 3-3 and in Table 3-2, respectively.

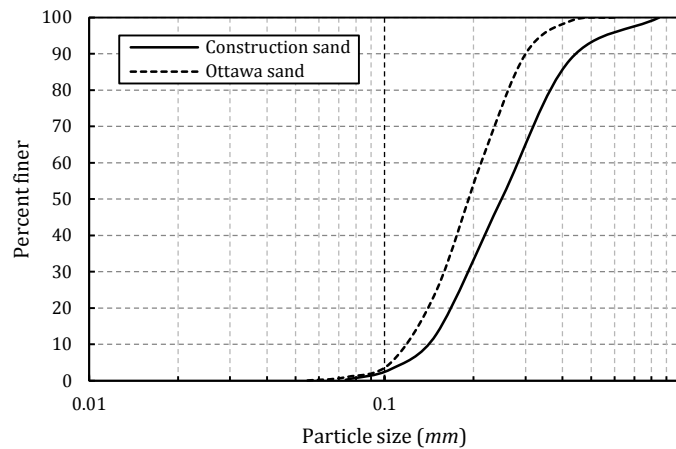


Figure 3-3: Particle size distribution curves.

Table 3-2: Soil properties.

Soil	G_s	e_{min}	e_{max}	D_{50}	C_u^*	C_c^\dagger
Ottawa sand	2.66	0.61	0.79	0.19	1.69	1.01
Construction sand	2.66	0.46	0.81	0.25	1.87	0.91

* Coefficient of uniformity

† Coefficient of curvature

The thickness of the active layer in permafrost is a few centimetres to a few metres exposed to seasonal and sometimes daily freeze-thaw cycles (Johnston 1981). Thus, these soils experience microstructural changes as shown by Viklander (1998) and Qi et al.

(2008). They demonstrated that initially loose and dense soils (silty soil and silty till) end up with the same constant residual void ratio after a few freezing cycles. In this study, considering the effect of freeze-thaw cycles on the void ratio and its small range in the Ottawa sand, a relative density of 50% was considered for the surficial active layer.

Frozen soil: As the investigation of the interaction between the frozen and unfrozen soils is the main goal of this research, only mechanical properties of frozen soil, i.e., shear wave velocity, friction angle, and cohesion, are considered and parameters related to the thermal behaviour and long-term mechanical response (creep) are not considered in the scope of this work. Having this in mind as well as the challenges in working in laboratory temperatures with frozen and unfrozen soils at the same time, a sand-cement mixture (SCM) was used to represent the blocks of frozen soil. SCM is a cured mixture of sand, Portland cement and water that has a higher shear wave velocity compared to ordinary sand (El Naggar et al. 2013). In addition, application of the SCM allows the control of the required shear wave velocity and to some extent unconfined compressive strength (in order to satisfy similitude relations) by using a proper mix design.

Most of the ultimate shear strength of frozen soil is provided by cohesion where internal friction has an insignificant role (even in sandy soils) (Tsytoovich 1975). The ultimate shear strength of frozen soils (subjected to normal pressures of up to 2 MPa) under instant loading can be determined from the Mohr-Coulomb equation:

$$\tau_{ult} = c_{\theta} + \sigma \tan \phi_{\theta} \quad (3-1)$$

where, τ_{ult} is the ultimate shear strength, σ is the normal stress, c_{θ} is the cohesion and ϕ_{θ} is the internal friction angle. Subscript θ for cohesion and friction denotes function of temperature. Table 3-3 gives examples of the variation of cohesion with temperature for a silty sand with a moisture content of 23%, as reported by Tsytoovich (1975).

Table 3-3: Variations of cohesion with temperature (θ) for a silty sand (Tsytoovich 1975).

	$-0.4^{\circ}\text{C} \leq \theta \leq -0.3^{\circ}\text{C}$	$-1.2^{\circ}\text{C} \leq \theta \leq -1.0^{\circ}\text{C}$	$-4.2^{\circ}\text{C} \leq \theta \leq -4.0^{\circ}\text{C}$
c_{θ} (MPa)	1.1	1.4	2.0

On the other hand, the compressive strength of frozen soils depends on temperature, moisture content and their composition and structure (Tsytoovich 1975). Results of uniaxial compression tests on structurally undisturbed frozen silty sand sampled from permafrost reported in Tsytoovich (1975) are presented in Table 3-4.

Table 3-4: Uniaxial compression resistance of structurally undisturbed permafrost (silty sand) (Tsytoovich 1975).

Moisture content (%)	Temperature (°C)	Strength (MPa)
19.8	-1.3	10.3
19.1	-3.9	13.7
19.8	-12.0	17.1
29.3	-11.0	9.5

Experiments show that frozen soils have an elastic modulus tens to hundreds of times larger than that of unfrozen soils. The elastic modulus of frozen soil is a function of the ice content, negative temperature, external pressure and composition of soils. At the same time, the Poisson’s ratio for frozen soils increases from typical values for solids in low temperatures to almost 0.5 for temperatures close to 0°C (Tsytoovich 1975).

The ultrasonic studies of Nakano and Froula (1973) on artificially frozen samples of Ottawa sand and Hanover silt and investigations of Zimmerman and King (1986) on undisturbed permafrost soils from the Mackenzie River valley, Beaufort Sea and the Canadian Arctic Islands show typical ranges of shear wave velocity of 1200-1900 m/sec for silt and 1750-2500 m/sec for sand. Furthermore, the seismic cone penetration tests and seismic tomographic imaging performed by LeBlanc et al. (2004) in silty sand permafrost at Umiujaq, northern Quebec, Canada, revealed a shear wave velocity between 900 and 1750 m/sec. Based on the above observations, an average value of 1500 m/sec was chosen for the shear wave velocity of the frozen soils.

Viscous fluid: It is not possible to simultaneously satisfy the similitude relations for both “dynamic” and “diffusion” times in small-scale saturated geotechnical models without changing soil permeability or pore fluid viscosity (Muir Wood 2004). The former controls the dynamic aspects of loading and related parameters, whereas the latter regulates the phenomenon of excess pore pressure build-up. In this study, the diffusion time scale was adjusted by increasing the viscosity of the pore fluid. To this end, a glycerine-water

solution was used instead of water. After the required value of viscosity was determined from Table 3-1, the glycerine was diluted with water (25% water, 75% glycerine) to reach the target viscosity based on the proportions presented by Cheng (2008).

Preparation of soil model: The bottom layer of construction sand with relative density of 80% and total height of 20 cm was placed in the laminar container in five successive sublayers of equal height compacted using the moist compaction method. The overlying layer comprised Ottawa sand and was placed using the same method to a total thickness of 18.75 cm and relative density of 65%. The top layer, representing the active layer, with thickness of 1.25 cm and relative density of 50% was also composed of Ottawa sand and was deposited using the water sedimentation method. A sand pluviator consisting of a funnel, sieve, and two sliding rods was designed for this purpose to move over the flexible container and to uniformly distribute the sand over the desired area. The pluviator was first calibrated with the glycerine-water solution (the pore fluid) and an appropriate sieve size was selected such that the target relative density was attained. Following the preparation of each test model, it was left for 24 hours to ensure that the excess pore pressure was dissipated completely.

3.2.4 Instrumentation

A number of accelerometers and miniature pressure transducers were installed in each test model. The accelerometers were fixed to the top layer (by rigid glue to the SCM blocks) in order to monitor the ground surface accelerations and one was rigidly attached to the table top to monitor the base input acceleration. Miniature pressure transducers were employed to monitor the changes of pore water pressure. The transducers were small and light-weight enough for the least possible interaction with the surrounding soil. To measure the net water pressure a bronze filter was added to the tip of the transducers. The maximum capacity of the transducers was 1 bar (1 bar=100 kPa) and they were calibrated before application. Technical specifications of the instruments are given in Appendix A. A schematic view of the test setup is illustrated in Figure 3-4. The geometric parameters of the experiments are presented in Table 3-5.

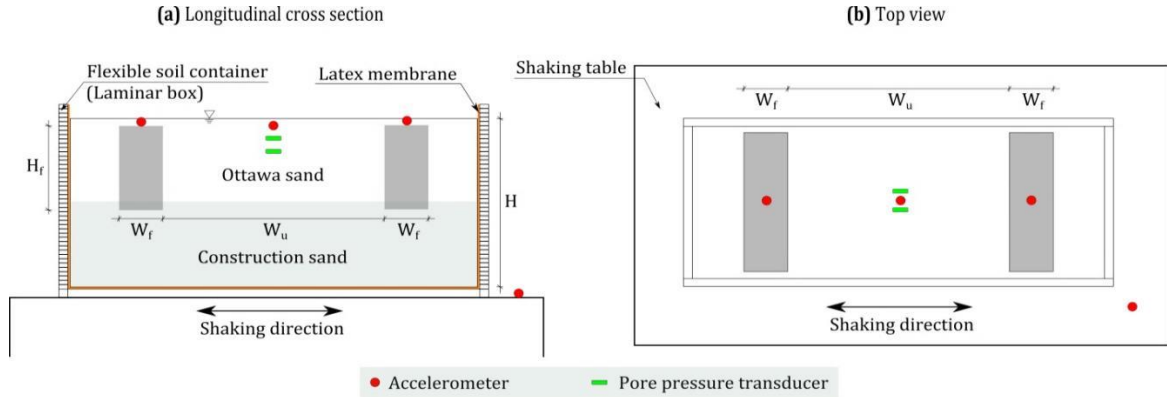


Figure 3-4: Schematic presentation of typical test setup (a) longitudinal cross-section and (b) top view. Frozen soil blocks are indicated in grey color. H_f , height of frozen block; W_f , width of frozen block; W_u , distance separating frozen blocks.

Table 3-5: Configurations of soil models used in experimental program (all dimensions in centimetres).

Experiment No.	No. of blocks	Total thickness of soil (H)	Block thickness* (H_f)	Block width (W_f)	Span length (W_u)
1	0	40	-	-	-
2	1	40	20	10	-
3	2	40	10	10	50
4	2	40	20	10	50
5	2	40	38.75	10	50
6	2	40	20	10	30
7	2	40	10	10	30
8	2	40	10	10	10-50 [†]

* Top of the frozen blocks was at 1.25 cm from the surface of the model, the thickness representing the active layer.

[†] Refer to Figure 3-15 for details.

3.3 Numerical simulations

The direct nonlinear method is suitable for site response analysis because of its ability to describe the behaviour of soils subjected to cyclic loads in a realistic manner (Kramer 1996). Important practical issues and developments related to this technique were highlighted by Hashash et al. (2010). FLAC software (Itasca Consulting Group, Inc. 2002) has capabilities to simulate many of the advanced features of the nonlinear dynamic method in the site response analysis. It applies an explicit finite difference scheme to solve the full equations of ground motion in continua. Discontinuous permafrost regions in North America often comprise saturated cohesionless and potentially liquefiable soils (Finn and Yong 1978). Therefore, a representative

constitutive model has to be employed to simulate pore-water pressure changes in the unfrozen soils during the application of seismic loads. The constitutive model proposed by Byrne (1991) that relates the increment of volumetric strain to the cyclic shear strain and uses the Mohr-Coulomb plasticity to define the soil behaviour under effective stress, can be used in FLAC.

The results of the site response experiments conducted in the current study explained some of the effects of a number of parameters and provided data to calibrate and verify the numerical models established using FLAC. The verified numerical models were then used to predict site behaviour in cases that were otherwise not feasible to test in the lab.

The finite difference grid of the model had 468 zones distributed in 13 rows and 36 columns. The width of each zone was 2.5 cm and zone heights varied between 1.25 and 5 cm depending on the location and geometry of the blocks. In this section, assumptions made for the numerical modelling are discussed.

3.3.1 Soil stiffness degradation and damping

Soil stiffness and damping are parameters required for seismic site response analysis. The stiffness of a sand deposit is represented by the shear modulus at very low strain level (G_{\max}) and the secant shear modulus (G_{sec}), which varies as a function of the relative density, overburden pressure, cyclic strain amplitude, and number of loading cycles (Kramer 1996). There is ample research investigating soil stiffness degradation (Iwasaki et al. 1978, Kokusho 1980, and Seed and Idriss 1970). In contrast, only a few studies considered frozen soils (Singh and Donovan 1977). Results of some of the few studies characterizing degradation of frozen soil are shown in Figure 3-5, which presents two degradation curves reported by Seed and Idriss (1970) and Singh and Donovan (1977) for average sand and frozen sand, respectively.

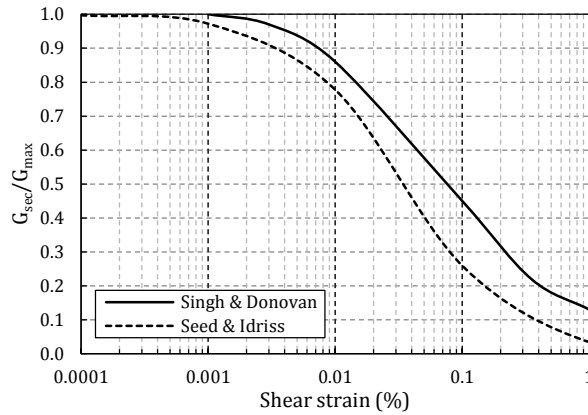


Figure 3-5: Shear modulus reduction curves for frozen sand at -1°C by Singh and Donovan (1977) and average unfrozen sand by Seed and Idriss (1970).

Hardin and Drnevich (1972) developed an equation to describe the shear modulus degradation (G_{sec}/G_{max}), which was used to establish EPRI (1993) curves representing the shear modulus reduction under different levels of overburden pressure. This equation is given by:

$$G_{sec}/G_{max} = [1 + (\gamma/\gamma_{ref})]^{-1} \quad (3-2)$$

where, γ and γ_{ref} are the shear strain and the reference shear strain, respectively. In the current study, Equation (3-2) was employed to model the variation of G_{sec} with shear strain. The reference strain, γ_{ref} , was varied until the best fit to the target curves, shown in Figure 3-5, was obtained.

Soil deposits undergoing cyclic loading dissipate energy, which is manifested by their hysteresis loops. The energy dissipation during nonlinear response, defined as material damping, is obtained by computing the area confined by the hysteresis loops. For moderate to high strain levels, the material damping represents the nonlinearity of the material, whereas for low strain levels the damping is assumed to be zero because the material remains in the linear elastic range. However, lab experiments show that even for small strains, soil dissipates some energy and has some form of damping (Zhang et al. 2005). Thus, a minimum value of damping should usually be considered in the analysis.

In this study, a 0.5% Rayleigh damping over the range of predominant frequencies (Itasca Consulting Group, Inc. 2002) was used.

3.3.2 Excess pore-water pressure model

Changes of pore-water pressure can be calculated by employing either the Martin et al. (1975) equation or the simplified Byrne's formula (Byrne 1991). In the current study, excess pore-water pressure build-up under seismic excitation was modelled employing the simplified Byrne's formula, which relates the incremental volumetric strain ($\Delta\varepsilon_{vd}$) to the cyclic shear and volumetric strains (γ and ε_{vd} , respectively) as (Byrne 1991)

$$\Delta\varepsilon_{vd} = C_1\gamma \exp\left[-C_2\left(\frac{\varepsilon_{vd}}{\gamma}\right)\right] \quad (3-3)$$

where, C_1 and C_2 are constants that in many cases are related to each other by $C_1.C_2=0.4$. C_1 can be calculated from the relative density (D_r) as follows:

$$C_1 = 7600(D_r)^{-2.5} \quad (3-4)$$

The relative density in turn, may be defined as a function of the corrected standard penetration test (SPT) blow count ($(N_1)_{60}$),

$$D_r = 15\sqrt{(N_1)_{60}} \quad (3-5)$$

Another constant, C_3 , is used in the model to define a threshold strain below which no excess pore pressure is generated. Following the calculation of the excess pore pressure, the program computes the effective stresses and applies them in the Mohr-Coulomb shear failure criterion.

3.4 Experimental and numerical results

Initially, experiment No. 1 was performed on the unfrozen saturated soil model to establish the mean shear wave velocity of the material, vital for realistic numerical modelling. To this end, the model was excited by the El Centro record and the natural frequency was estimated. The intensity of the original acceleration time-history was scaled down to $PGA=0.05g$ in order to ensure that the soil would remained within the

linear range. The obtained transfer function is defined as the ratio of the Fourier amplitudes of the soil surface acceleration to those of the base motion acceleration. The obtained transfer function is displayed in Figure 3-6.

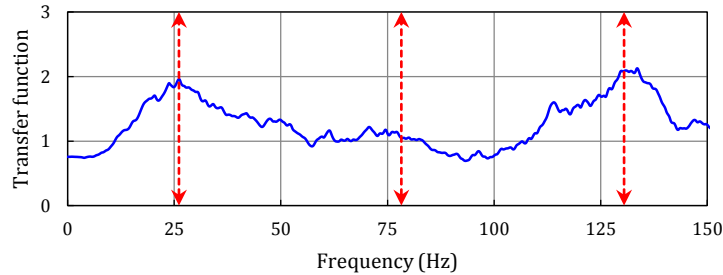


Figure 3-6: Transfer function of unfrozen soil deposit under low-intensity base excitation, PGA=0.05g. Dashed arrows indicate the first three natural frequencies of the model.

From the transfer function, the frequency corresponding to the first peak value was considered as the potential fundamental frequency (f_1) of the deposit. The natural frequencies of a soil layer can be approximated from (Kramer 1996):

$$f_n \approx \frac{\bar{V}_s}{4H} (2n - 1) \quad n = 1, 2, 3, \dots, \infty \quad (3-6)$$

where, \bar{V}_s is the average shear wave velocity, H is the thickness of deposit, and n is the mode number. Considering $f_1=26$ Hz and substituting $n=1$ and $H=0.4$ m in the formula, the average shear wave velocity was estimated to be 42 m/sec. In order to examine the accuracy, two consecutive higher frequencies that were in the range of the input frequencies were also approximated by the formula ($f_2=78$ Hz, and $f_3=130$ Hz) and are indicated in Figure 3-6 by dashed arrows. As it can be observed from Figure 3-6, they coincide with the global and local peaks of the transfer function. This confirms the validity of the computed average shear wave velocity.

The variation of soil stiffness along the soil profile considered in the numerical model was assumed to be parabolic based on the empirical equations for G_{max} of sand (Seed and Idriss 1970). The distribution function was determined by trial and error such that its

average value is close to the value back-calculated from the experiment. This is accomplished by varying the stiffness distribution and comparing the calculated response with the measurements from the physical model test until the best match is achieved. The minimized error function was indeed the difference of the acceleration response spectra (SA) of the soil surface motion obtained from the numerical and experimental models. Figure 3-7 demonstrates the best match of the responses after performing height-wise stiffness corrections. It should be noted that the spectra presented in this study are derived from the ground motions converted to the original time scales.

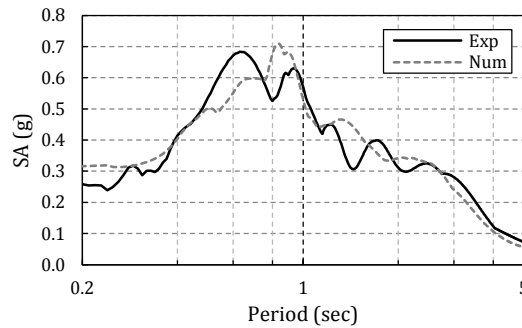


Figure 3-7: Experimental and numerical acceleration response spectra (respectively denoted by Exp and Num) after performing vertical stiffness corrections.

In experiment No. 2, an SCM block with thickness of 0.5H (20 cm) was buried in the centre of the model leaving 1.25 cm of unfrozen soil above the block. The results of this test under the high level of excitation (PGA=0.5g) are shown in Figure 3-8. It can be seen from Figure 3-8a that the recorded response at the top of the frozen block is higher than that of the unfrozen soil for the period range of 0.2-5 sec. This is confirmed by the ratio of both responses displayed in Figure 3-8b, which shows that the spectral response at the top of the frozen block (SA_f) can be up to 60% higher than the response of the unfrozen soil (SA_u).

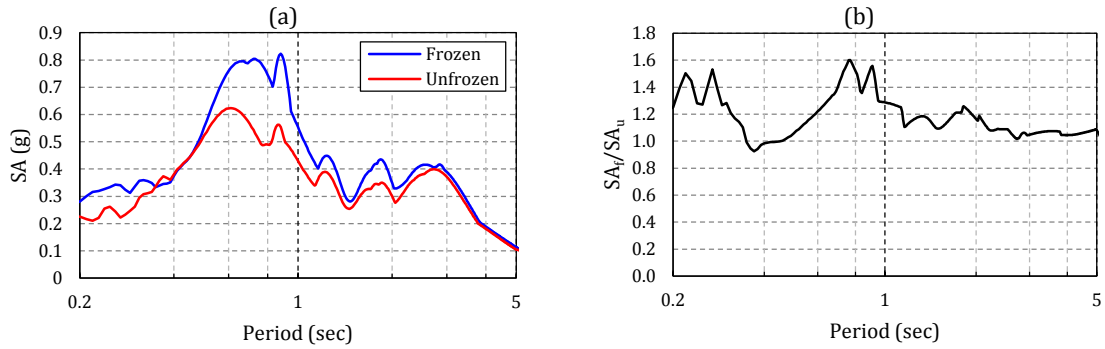


Figure 3-8: Results of experiment No. 2: (a) acceleration response spectra and (b) ratio of the frozen block and unfrozen soil response spectra.

Effect of block thickness: The effect of the frozen block thickness on the site response was investigated in experiment Nos. 3, 4 and 5 with block heights of 0.25H (10 cm), 0.5H (20 cm) and H (40 cm) as per Table 3-5. In each test, two blocks were placed at a distance equal to five times the block width (50 cm). The unfrozen soil thickness remained constant and equal to 40 cm. Results of the three tests under the high level of shaking intensity, i.e., $PGA=0.5g$, are illustrated in Figure 3-9. Only minor differences in the responses of frozen and unfrozen soils were observed, thus suggesting that the relative thickness of the frozen blocks has insignificant effect on the site response.

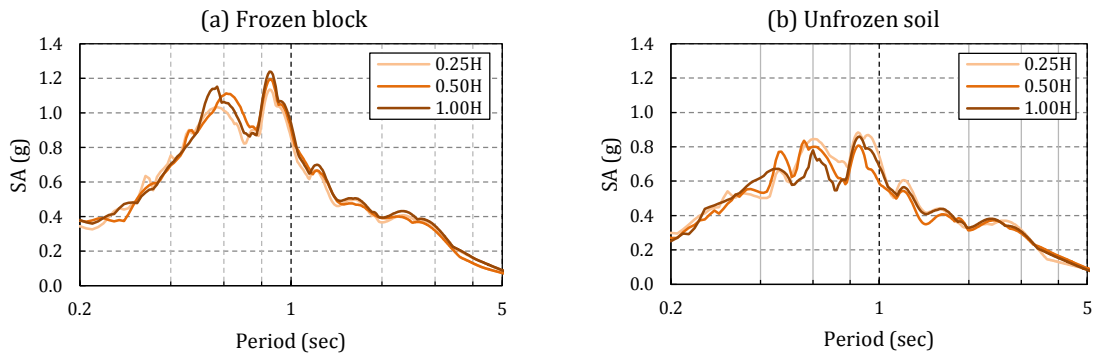


Figure 3-9: Acceleration response spectra at the top of (a) frozen blocks, and (b) unfrozen soil. Legends indicate thickness of frozen blocks, where H denotes total thickness of soil layers.

Effect of distance between frozen blocks: Two of the experiments, Nos. 4 and 6 (Table 3-5), were conducted to investigate the effect of the distance separating the frozen blocks (or span), W_u , on their interaction with unfrozen soil. Figures 3-10a and b compare the experimental and numerical spectral acceleration responses obtained at the top of the model for experiment Nos. 4 and 6. For both tests, favourable agreement can be observed between the experimental and numerical response spectra (SA). In addition, the excess pore-water pressure ratio, r_u , was obtained at a depth of 5 cm within the unfrozen soil between the blocks. The excess pore-pressure ratio is defined as:

$$r_u = \frac{\Delta u}{\sigma'_v} \quad (3-7)$$

where, Δu is the excess of pore water pressure and σ'_v is the vertical effective stress. Figures 3-10c and d compare the experimental and numerical r_u values obtained at a depth of 5 cm within the unfrozen soil between the blocks. Again, favourable agreement can be observed between the experimental and numerical results.

Theoretically, when the excess pore water pressure reaches the value of the vertical effective stress, i.e., $r_u=1$, the soil particles lose their contact and liquefaction occurs. No evidence of liquefaction, such as large displacements at the surface, could be observed in either experiment under the high level of shaking intensity (PGA=0.5g), but at the end of the vibrations the unfrozen soil seemed to be on the verge of liquefaction with relatively high r_u ($0.7 < r_u < 0.9$).

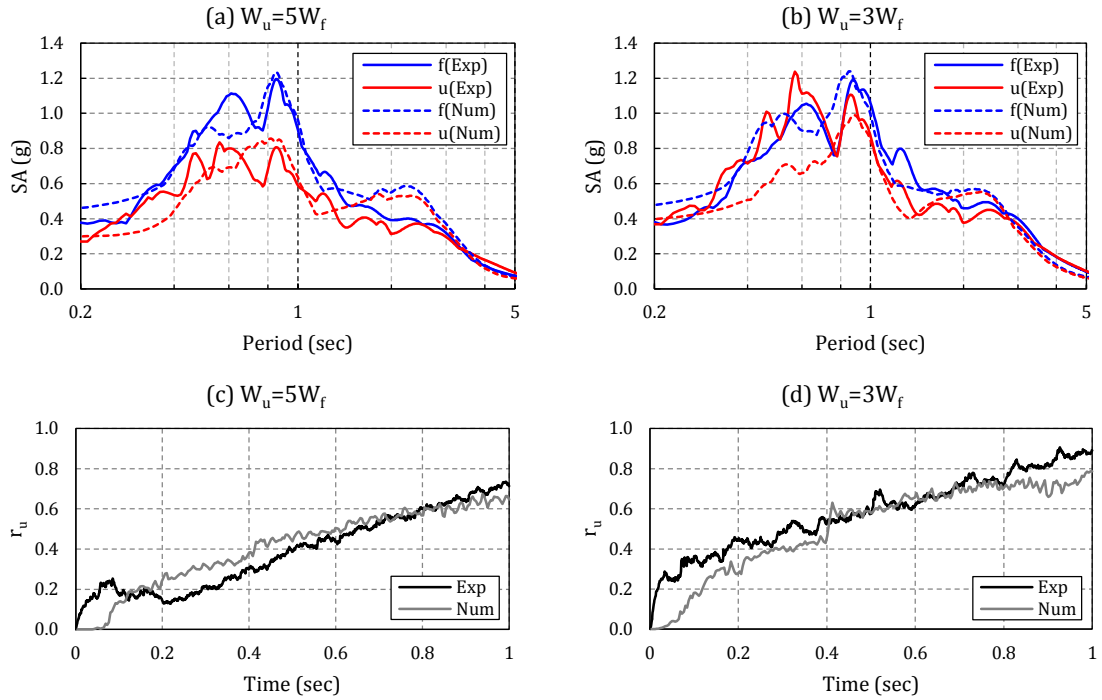


Figure 3-10: Spectral acceleration obtained from shaking table experiments (Exp) and numerical modelling (Num) for (a) $W_u=5W_f$ and (b) $W_u=3W_f$. Time histories of r_u in unfrozen soils measured at depth of 5 cm at mid-distance between blocks for (c) $W_u=5W_f$ and (d) $W_u=3W_f$. Subscripts f and u indicate frozen and unfrozen soil responses, respectively.

The verified numerical model was used to predict soil behaviour for other distance combinations of the frozen soil blocks. Results of the parametric study for frozen blocks and unfrozen soil are depicted in Figure 3-11. The spectral responses of frozen blocks remain almost constant, whereas those of unfrozen soils generally decrease by increasing the span, W_u . The highest reduction for unfrozen soils is 36% and is observed at the peak spectral acceleration. Similar reduction was observed in PGA as well. In summary, W_u has higher influence on the dynamic response of the unfrozen soils than that of the frozen blocks.

Theoretically, when the span approaches infinity, the spectral response of the unfrozen soil between the frozen blocks should reach the values of the unfrozen soil obtained in experiment No. 1, and response of the frozen soil should attain the site response of a

single block (experiment No. 2). To check the results, the two mentioned boundary cases are also depicted by dashed lines in Figure 3-11. In both cases, the dashed lines reside below the continuous curves, indicating that the numerical model predicts the trends correctly.

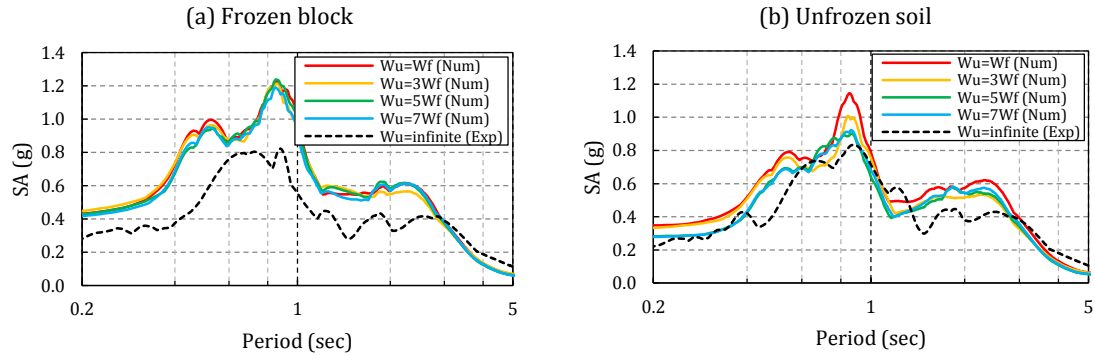


Figure 3-11: Study of effect of span length (W_u) on site response in (a) frozen and (b) unfrozen soils. Experimental and numerical responses are respectively denoted by **Exp and **Num**.**

Effect of block width: The parametric study results of the effect of block width (W_f) on the site response are presented in Figure 3-12. The span (W_u) remained constant and equal to 50 cm. As it can be noted from Figure 3-12, the frozen soil response is considerably more sensitive to W_f than the unfrozen soil. The highest spectral accelerations of the frozen soil are obtained for the smallest widths ($W_f < 0.2W_u$). It seems that the shear stiffness of the frozen blocks, which is proportional to their width, plays a major role in their dynamic interaction with unfrozen soil. With the increase of W_f , the response decreases and becomes almost constant beyond $W_f = 0.6W_u$. For the considered widths, the maximal difference between the peak spectral accelerations was 33% in frozen soil, compared to the only 5% decrease in unfrozen soil. Similar ratios were obtained for the PGA values.

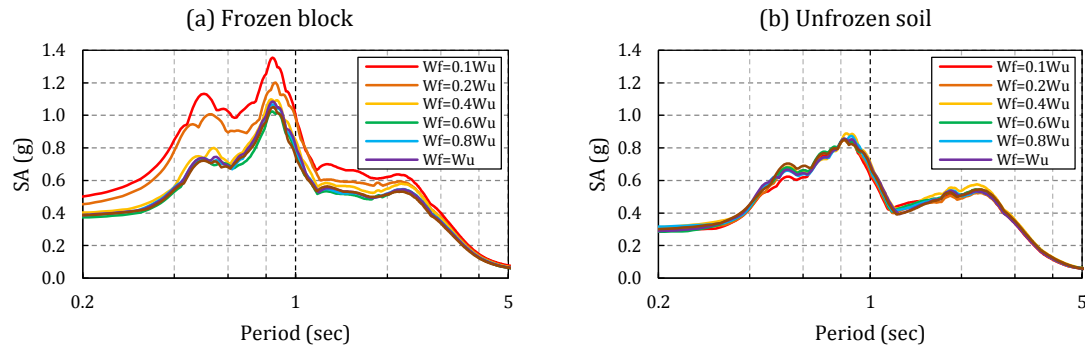


Figure 3-12: Study of effect of block width (W_f) on site response in (a) frozen and (b) unfrozen parts. The distance between the blocks remained constant, $W_u=50$ cm.

Effect of number of blocks (numerical simulations only): In the above lab experiments and accompanying numerical models, a maximum of two frozen blocks were considered. In the field, however, the intermittent character of the discontinuous permafrost can contribute to frequent occurrence of the frozen and unfrozen areas. To investigate the interaction when more than two frozen blocks are present, numerical simulations were performed in which the number of blocks was increased gradually from two to five while the distance between the blocks (span) remained constant (50 cm). The response of all the considered frozen blocks and the unfrozen soil between them was calculated. As the results displayed low scattering and no specific trend could be observed in the responses, the minimum and maximum envelopes are shown in Figure 3-13. The maximal differences between the peak spectral accelerations were in the order of 10% for both frozen blocks and unfrozen soil indicating that the soil response is not sensitive to the number of frozen blocks considered when it is higher than two.

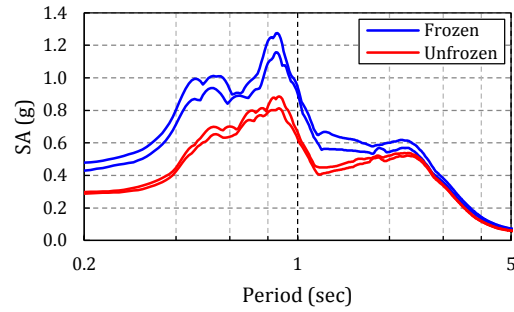


Figure 3-13: Envelopes of maximum and minimum spectral response for the number of frozen blocks varying between two and five. Distance between the blocks remained constant, $W_u=50$ cm.

Sensitivity to shear wave velocity (numerical simulations only): As discussed in Section 3.2.3, the shear wave velocity of frozen sand and silty sand varies in a broad range of 900-2500 m/sec. In the above experiments (SCM blocks) and numerical simulations, the shear wave velocity, V_s , of frozen soil was assumed equal to 1500 m/sec. To examine the sensitivity of the site response to the shear wave velocity of the frozen soils, a series of numerical analyses was performed in which V_s was increased gradually from 1000 m/sec to 2500 m/sec. In Figure 3-14, only the results of the two extreme cases are presented with the other results falling between them. As can be observed in Figure 3-14, the response of the frozen soil shows a descending trend with increase of the shear wave velocity, with a maximal difference of about 12% for the peak spectral response. At the same time, spectral response of the unfrozen soil remains almost constant.

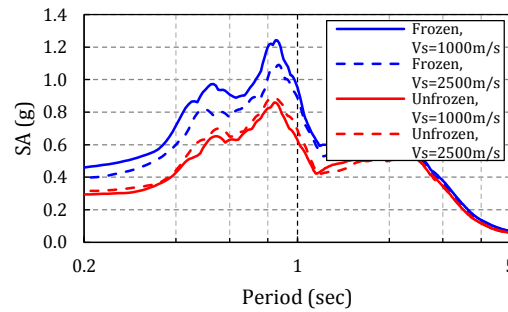


Figure 3-14: Sensitivity of site response to varying shear wave velocity of frozen blocks. Distance between blocks remained constant, $W_u=50$ cm.

Intensity of base excitation (laboratory experiments only): The experimental results presented above were obtained under the “high” base excitation. Most of the experiments were also repeated for different base excitations referred to as “low” (PGA=0.15g), “medium” (PGA=0.3g) and “high” (PGA=0.5g). To investigate the impact of the different levels of seismic excitation on the site response, the measured PGA values at the ground surface during all conducted shaking table experiments are presented in Figure 3-15 for all the considered frozen block configurations. As expected, the obtained ground response of the frozen soil is systematically higher than that of the unfrozen soil for all three levels of seismic excitation. This is clearly demonstrated by comparing the average PGA response of the frozen and unfrozen soils indicated with dashed lines in Figure 3-15. The ratio between the average PGAs of the frozen to unfrozen soils increased from about 1.25 for low-intensity, to 1.30 for medium-intensity and to 1.42 for high-intensity earthquakes.

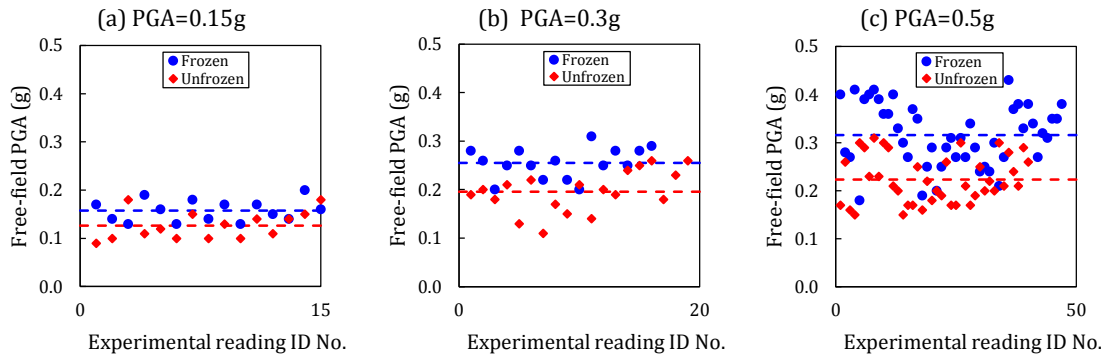


Figure 3-15: Experimental readings of PGA in frozen blocks and unfrozen soils for (a) low, (b) medium and (c) high intensities of base excitations. Dashed lines depict average of the PGAs.

Interaction of nonparallel blocks (laboratory experiments only): All experiments studied in this section were planned in a way that conditions of plane strain were satisfied. To investigate a general case in which the frozen blocks are not perpendicular to the direction of the input motion and are not parallel to each other (three-dimensional (3D) conditions), an additional experiment was conducted (experiment No. 8) with a test setup as shown in Figure 3-16. The distance between the frozen blocks varies from 10 cm to 50 cm with an average of 30 cm at the centre of the blocks.

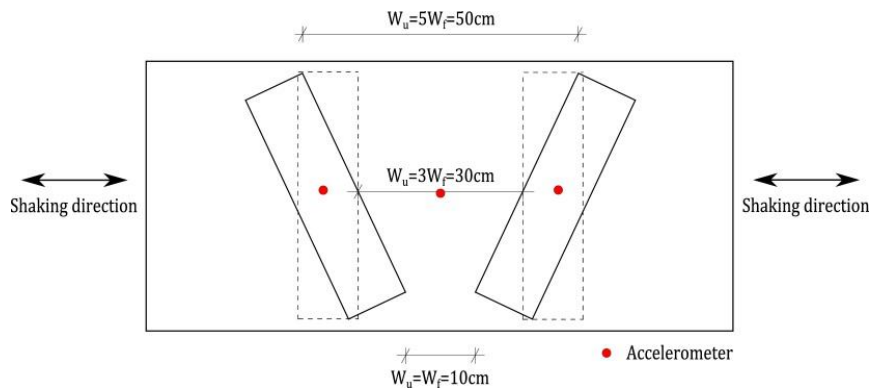


Figure 3-16: Top view of test setup of experiment No. 8. Dashed lines represent location of blocks in experiment No. 7 for comparison.

To determine the effect of the direction of the frozen blocks on the site response motion, the acceleration of the unfrozen soil was recorded at the mid-distance between the frozen

blocks by using a biaxial accelerometer. Under “low”, “medium” and “high” excitation levels, the transverse PGAs were 13.3%, 13.1% and 12.6% of the longitudinal ones respectively. Furthermore, the ground responses were compared to those of a plane strain case in which the unfrozen span was 30 cm, i.e., equal to the average of the current variable span. The specifications of the plane strain case are presented in Table 3-5 (experiment No. 7) and the corresponding block layout is shown by dashed lines in Figure 3-16. The results of the two experiments are presented in Figure 3-17. As it can be seen, the spectra derived from both experiments agree well for both frozen and unfrozen soils. Also, PGAs of frozen blocks and unfrozen soil show 4.1% and 2.5% variations respectively. The results of experiment Nos. 7 and 8 demonstrate that the response of the 3D case can be approximated by the response of the simplified 2D plane strain model with reasonable accuracy.

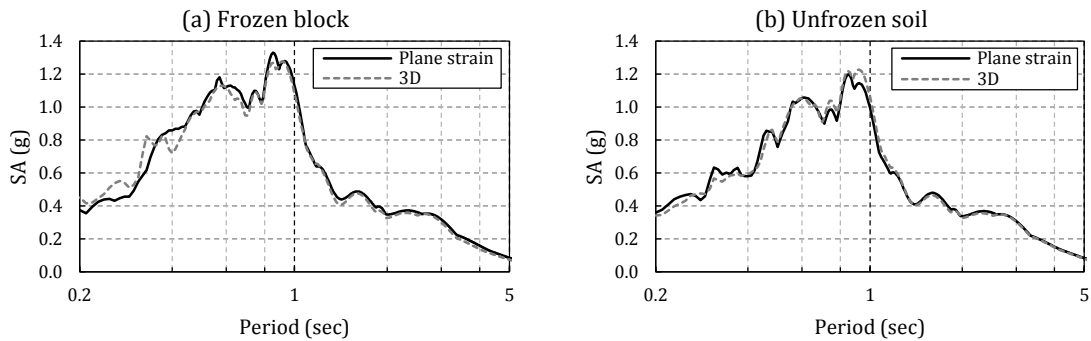


Figure 3-17: Comparison of free-field responses of plane strain and 3D cases in (a) frozen and (b) unfrozen soils.

3.5 Practical application of results

Performing controlled lab experiments fully satisfying the physical aspects of a complex phenomenon such as permafrost is, in many cases, theoretically and technically impossible. Therefore, making some assumptions and simplifications is inevitable. For example, the shear wave velocity of the permafrost is a temperature-dependent parameter. As permafrost is subjected to a vertical temperature gradient, a certain variation of the shear wave velocity with depth can be expected. LeBlanc et al. (2004) studied cryostratigraphy of a permafrost near Umiujaq in northern Quebec, Canada, performing

seismic cone penetration and tomography tests. Based on their results typical temperature and V_s schematic profiles are illustrated in Figure 3-18. As it can be seen, below a specific depth where the temperature approaches zero, degradation of V_s starts. Between the top of permafrost and this depth, V_s has its largest values and the smallest fluctuations and can be replaced by an average constant value as shown in Figure 3-18. As below the effective depth V_s of the frozen soil tends to that of the adjacent unfrozen soil, dynamic interaction between them reaches to its minimum, particularly at greater depths. Therefore, simulating only the effective depth of permafrost was a reasonable approximation in the experiments. For practical applications and according to the local temperature gradient an appropriate effective depth should be selected as the thickness of the frozen block (H).

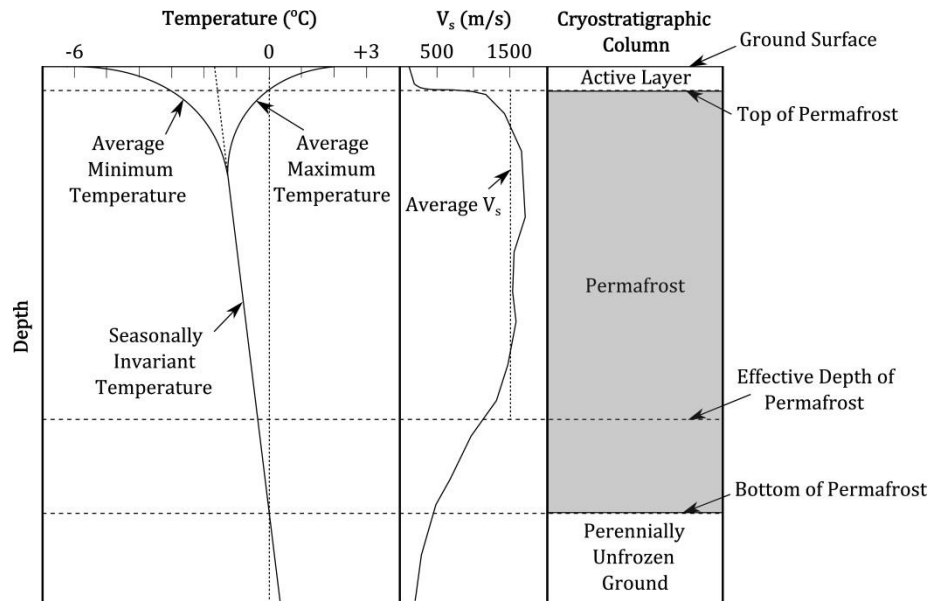


Figure 3-18: Schematic profile of temperature and shear wave velocity (V_s) in depth of permafrost based on LeBlanc et al. (2004).

In discontinuous permafrost regions, soil conditions change spatially from frozen to unfrozen and vice versa. A schematic presentation of such a transition zone over which shear wave velocity changes gradually is given in Figure 3-19. Due to practical difficulties such transitions could not be simulated in the experiments and the obtained results correspond to cases with abrupt changes of shear wave velocity. This

simplification affects the magnitude of the measured parameters. To make the laboratory results transferable to real field conditions, the lateral interaction of frozen and unfrozen soils has to be considered. Due to the considerably higher shear wave velocity, frozen soil acts like an embedded vertical shear beam that affects the site response by having interaction with unfrozen soil. According to this simple shear model, at any depth permafrost and transition zones can be treated as parallel springs with different stiffness factors. Thus, assuming the shear stiffness at any depth as proportional to the product of the shear modulus and the cross-sectional area of the frozen block, one can account for the effects of the transition zones by modifying the shear stiffness of permafrost. The total stiffness of such a frozen block system of permafrost and transition zones is:

$$K_f = K_p + K_t \quad (3-8)$$

where, K_f , K_p and K_t are the stiffness factors of the frozen block system, permafrost and the transition zones, respectively. As the shear modulus is proportional to the square of shear wave velocity, in a deposit with unit thickness (cross-sectional area equals width) Equation (3-8) can be written as:

$$W_f V_s^2 = W_p V_{sp}^2 + W_t V_{st}^2 \quad (3-9)$$

where, W_f is the total width of the frozen block system, W_p is the width of the permafrost, W_t is the total width of the transition zones, and V_{sp} and V_{st} are the corresponding average shear wave velocities. According to the results presented in Section 3.4, an increase of the lateral shear stiffness of the frozen block by increasing either V_s or W_f leads to a decrease of the frozen block response (Figures 3-12 and 3-14). However, this does not affect the unfrozen soil response. Therefore, response of the frozen block is conservatively higher if the effect of transition zones is neglected.

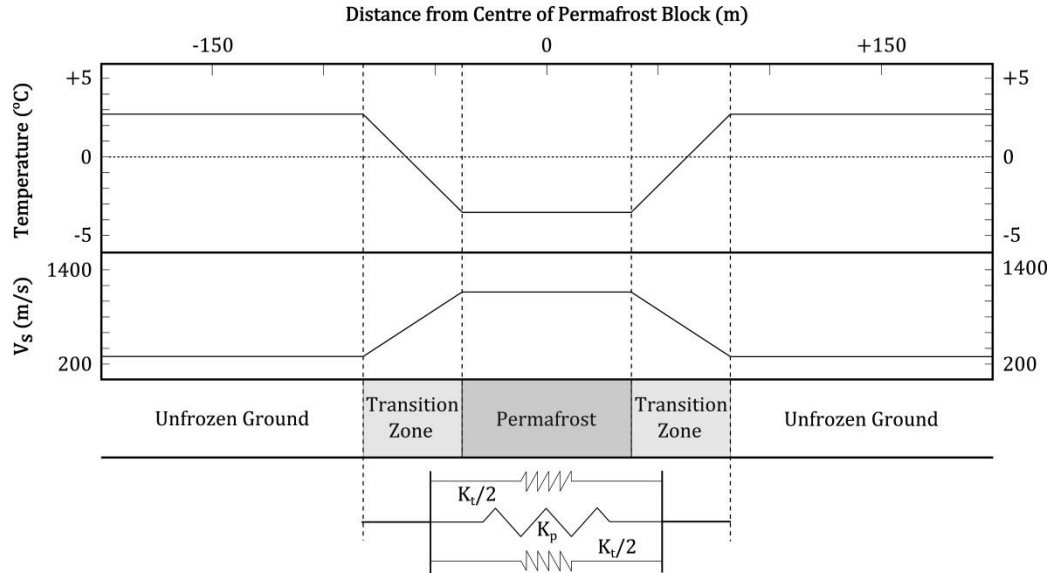


Figure 3-19: Schematic horizontal distribution of temperature and shear wave velocity in discontinuous permafrost regions and spring model of permafrost-transition zones system.

Another parameter to be considered is the presence of some unfrozen water in permafrost and its potential viscoelastic effects on energy dissipation. Two major damping mechanisms should be considered in wave propagation problems: hysteretic and viscous. The former is strain-dependent and proportional to the level of nonlinearity that the material experiences and the latter is frequency-dependent and increases with increase of wave frequency. In the case of seismic site response analysis, as strain levels in the prototype are high and frequency levels are low, the damping is predominantly hysteretic rather than viscous. However this is not the case in a model. As discussed earlier, the simulation rule for the stiffness of the frozen material (V_s) was satisfied but the shear strength of the blocks was not scaled down properly and the sand-cement mixture had some overstrength. Therefore, the blocks had a wider linear range and the generated hysteretic damping was smaller than anticipated. On the other hand, according to the simulation rules, the frequency content of the dynamic loading was scaled up (increased 32 times and up to 150 Hz) and consequently, the contribution of the viscous damping in energy dissipation in the model was higher when compared to the prototype. This

suggests that the model was still subjected to a reasonable amount of damping despite the different predominant damping mechanism compared to the prototype.

3.6 Conclusions

Laboratory experiments and numerical simulations were conducted to investigate the site effects in discontinuous permafrost conditions characterized by the intermittent presence of frozen soils. Particular attention was given to the dynamic interaction between the frozen soil blocks with the surrounding unfrozen soil. A series of shaking table tests with small-scale physical models was designed to conduct the experiments and to provide data to validate the numerical FLAC models. The following conclusions are drawn from this study:

- The obtained spectral response of the frozen soils is systematically higher than that of the unfrozen soils.
- The distance between the frozen blocks had a notable influence on the response of unfrozen soil, whereas frozen block responses were less sensitive. The spectral acceleration values of unfrozen soil generally decreased by increasing the distance.
- The unfrozen soil response was not sensitive to the width of the frozen blocks. At the same time, the frozen block response showed a decreasing trend (about 30%) for a 10 fold increased width.
- The relative thickness of the frozen blocks was not an important parameter in both the frozen and unfrozen soil response.
- Including more than two frozen blocks did not contribute to any observable trend in the soil responses. The envelopes of the minimum and maximum spectral accelerations showed about 10% differences for both frozen blocks and unfrozen soils.

- The increase of the shear wave velocity of the frozen blocks from 1000 m/sec to 2500 m/sec contributed to a decrease of the response spectral accelerations of the frozen blocks of about 12%. At the same time, the response of the unfrozen soils remained fairly constant.
- Free-field response of a physical model in which plane strain conditions were violated (with nonparallel blocks) was successfully simulated by a simplified 2D plane strain model in the lab. The experiments also further revealed that the perpendicular-to-excitation component of the free-field response is small compared to the parallel-to-excitation component.

The simplified physical model along with the numerical model used in this research generally addressed the dynamic soil-permafrost interaction phenomenon and revealed some significant pieces of information regarding the seismic site response of regions with discontinuous permafrost. Site investigations and monitoring are required to examine the reliability of the achieved results and to discover further aspects of the problem.

References

Alam M. J., and I. Towhata. "Some important aspects of physical modelling of liquefaction in 1-g shaking table." *2008 Seismic Engineering Conference: Commemorating the 1908 Messina and Reggio Calabria Earthquake*. Reggio Calabria, Italy: American Institute of Physics, 2008.

Bishop, A. W., G. E. Green, V. K. Garga, A. Andresen, and J. D. Brown. "A new ring shear apparatus and its application to the measurement of residual strength." *Geotechnique* 21, no. 4 (1971): 273–328.

Byrne, P. "A cyclic shear-volume coupling and pore-pressure model for sand." *Second International Conference on Recent Advances in Geotechnical Earthquake Engineering and Soil Dynamics*. St. Louis, 1991.

Cheng, N. "Formula for the viscosity of a Glycerol-water mixture." *Industrial and Engineering Chemistry Research* 47 (2008): 3285-3288.

El Naggar, M. H., A. Saeed, and O. Drbe. *Static and dynamic properties of fillcrete*. London: Geotechnical Research Centre, Western University, 2013.

EPRI (1993): Guidelines for determining design basic ground motions. Volume 1. Electric Power Research Institute, 1993.

Finn, W. D. L., and R. N. Yong. "Seismic response of frozen ground." *Journal of the Geotechnical Engineering Division (ASCE)* 104, no. 10 (1978): 1225-1241.

Finn, W. D. L., R. N. Yong, and K. W. Lee. "Liquefaction of thawed layers in frozen soils." *Journal of the Geotechnical Engineering Division (ASCE)* 104, no. 10 (1978): 1243-1255.

FLAC, fast lagrangian analysis of continua, user's guide. Minneapolis, MN: Itasca Consulting Group, Inc., 2002.

Geological Survey of Canada. "Digital borehole geotechnical database for the Mackenzie Valley/Delta region." <http://geogratias.gc.ca/api/en/nrcan-rncan/ess-sst/13a48ecb-e6e4-5dd1-84cc-078d9ddc0b87.html> (accessed 2014).

Hardin, B. O., and V. P. Drnevich. "Shear modulus and damping in soils: design equations and curves." *Journal of Soil Mechanics and Foundations Division (ASCE)* 98, no. 7 (1972): 667-692.

Hashash, Y. M. A., C. Phillips, and D. R. Groholski. "Recent advances in non-linear site response analysis." *Fifth International Conference on Recent Advances in Geotechnical Earthquake Engineering and Soil Dynamics*. San Diego, 2010.

Iai, S. "Similitude for shaking table tests on soil-structure-fluid model in 1g gravitational field." Yokosuka: The Port and Harbour Research Institute, 1988.

Iwasaki, T., F. Tatsuoka, and Y. Takagi. "Shear modulus of sands under torsional shear loading." *Soils and Foundations* 18, no. 1 (1978): 39-56.

Johnston, G. H. *Permafrost: engineering, design and construction*. Toronto: John Wiley & Sons, 1981.

- Kline, S. *Similitude and approximation theory*. New York, NY: McGraw-Hill, 1965.
- Kokusho, T. "Cyclic triaxial test of dynamic soil properties for wide strain range." *Soils and Foundations* 20, no. 2 (1980): 45-60.
- Kramer, S. L. *Geotechnical earthquake engineering*. Upper Saddle River, NJ: Prentice Hall, 1996.
- LeBlanc, A. M., R. Fortier, M. Allard, C. Cosma, and S. Buteau. "Seismic cone penetration test and seismic tomography in permafrost." *Canadian Geotechnical Journal* 41 (2004): 796–813.
- Martin, G. R., W. D. L. Finn, and H. B. Seed. "Fundamentals of liquefaction under cyclic loading." *Journal of the Geotechnical Engineering Division (ASCE)* 101, no. 5 (1975): 423-438.
- Moncarz, P., and H. Krawinkler. *Theory and application of experimental model analysis in earthquake engineering. Report No. 50*, Stanford, CA: John A. Blume Earthquake Engineering Center, Stanford University, 1981.
- Muir Wood, D. *Geotechnical modelling*. New York: Spon Press, 2004.
- Muller, S. W. *Frozen in time: permafrost and engineering problems*. Reston: ASCE, 2008.
- Nakano, Y., and N. H. Froula. "Sound and shock transmission in frozen soils." *2nd International Conference on Permafrost*. Washington DC, 1973.
- Qi, J., W. Ma, and C. Song. "Influence of freeze-thaw on engineering properties of a silty soil." *Cold Regions Science and Technology* 53 (2008): 397–404.
- Rocha, M. "The possibility of solving soil mechanics problems by use of models." *Proceedings of the Fourth International Conference on Soil Mechanics and Foundation Engineering*. London, UK, 1957.
- Roscoe, K. "Soils and model tests." *Journal of Strain Analysis* 3, no. 1 (1968): 57-64.

- Seed, H. B., and I. M. Idriss. *Soil moduli and damping factors for dynamic response analyses*. Earthquake Engineering Research Center, 1970.
- Singh, S., and N. C. Donovan. "Seismic response of frozen-thawed soil systems." *6th International Conference on Earthquake Engineering*. New Delhi, 1977.
- Towhata, I. *Geotechnical earthquake engineering*. Berlin: Springer-Verlag, 2008.
- Tsyтович, N. A. *The mechanics of frozen ground*. Washington DC: McGraw-Hill Book Company, 1975.
- Turan, A., S. D. Hinchberger, and H. El Naggar. "Design and commissioning of a laminar soil container for use on small shaking tables." *Soil Dynamics and Earthquake Engineering* 29 (2009): 404-414.
- Vargas-Monge, W. *Ring shear tests on large deformation of sand*. PhD dissertation, Tokyo: University of Tokyo, 1998.
- Verdugo, R., and K. Ishihara. "The steady state of sandy soils." *Soils and Foundations* 36, no. 2 (1996): 81-91.
- Viklander, P. "Permeability and volume changes in till due to cyclic freeze/thaw." *Canadian Geotechnical Journal* 35 (1998): 471-477.
- Wang, L., Z. Wu, J. Sun, X. Liu, and Z. Wang. "Characteristics of ground motion at permafrost sites along the Qinghai-Tibet railway." *Soil Dynamics and Earthquake Engineering* 29 (2009): 974-981.
- Yang, Z., U. Dutta, G. Xu, K. Hazirbaba, and E. E. Marx. "Numerical analysis of permafrost effects on the seismic site response." *Soil Dynamics and Earthquake Engineering* 31 (2011): 282-290.
- Yukon Geological Survey. "Alaska Highway geotechnical borehole database." <http://ygsftp.gov.yk.ca/YukonPermafrostNetwork/AK%20HWY%20borehole%20DB.htm> (accessed 2014).

Zhang, J., R. D. Andrus, and C. H. Juang. "Normalized shear modulus and material damping ratio relationships." *Journal of Geotechnical and Geoenvironmental Engineering (ASCE)* 131, no. 4 (2005): 453-464.

Zimmerman, R. W., and M. S. King. "The effect of the extent of freezing on seismic velocities in unconsolidated permafrost." *Geophysics* 51, no. 6 (1986): 1285-1290.

Chapter 4

4 Vulnerability of buried energy pipelines subject to seismic wave propagation in discontinuous permafrost³

4.1 Introduction

Rich in hydrocarbon resources, Canada's north is substantially covered by continuous and discontinuous permafrost or perennially frozen ground conditions (Natural Resources Canada 2016). Current and future pipeline corridors are exposed to geohazards typical for northern climate such as frost heave, thaw settlement, slope instabilities, etc. (Nixon et al. 1990, DeGeer and Nessim 2008, Blais-Stevens et al. 2010, and Oswell 2011). The relatively high seismic activity along the Mackenzie valley, the Richardson Mountains and in the offshore region of Yukon and Northwest Territories in the Beaufort Sea represents additional threat to the safety and integrity of the existing and projected energy pipelines in this region (Hyndman et al. 2005). Earthquakes impacts can be divided into two categories: transient ground deformations caused by wave propagation and permanent ground deformations as a result of landslides, faulting and liquefaction. These impacts should be considered in the design and risk assessment of buried pipelines (Atkinson et al. 1982, Hyndman et al. 2005, and Savigny et al. 2015).

The literature review revealed that the majority of the site response studies in northern climate conditions focused on numerical simulations of the continuous permafrost (e.g., Finn et al. 1978, Finn and Yong 1978, Wang et al. 2009, and Yang et al. 2011). In Chapter 3 the effects of horizontally discontinuous frozen soil conditions on site response was investigated with laboratory experiments and numerical simulations. It was concluded that the top response of the frozen soils parts can be considerably higher than that on top of the adjacent unfrozen soils. Consequently, during strong earthquake events, the pipelines in discontinuous permafrost regions can be exposed to different amplitudes of the transient seismic deformations within a short distance.

³ A version of this chapter has been submitted to the journal of Soil Dynamics and Earthquake Engineering.

In general, under transient ground deformations pipelines buried in heterogeneous soils or at sites with irregular topography have suffered comparably higher damage rates than those buried in uniform grounds (Nishio 1994, Liang and Sun 2000). The observed damage was most frequent in the transitional zones between soil irregularities. Only a few occurrences of damage were reported in the literature for modern steel-welded pipelines associated with transient ground motion (e.g., O'Rourke and Ayala, 1990).

This chapter aims to determine the vulnerability of continuous buried pipelines under discontinuous permafrost conditions. A finite element analysis program developed specifically for simulating soil-pipe interaction and quantification of pipe strains was used to assess the impacts of parameters such as soil density, size of frozen blocks, types of seismic waves, frequency of particles vibration, pipe cross-sectional parameters and burial depth.

4.2 Seismic wave propagation

Shallow underground structures are impacted by earthquake-induced transient ground deformations resulting from a combination of body waves (i.e., primary, P, and secondary, S) and surface waves (e.g., Rayleigh, R, and Love, L) (Kramer 1996). However, S and R waves develop significantly larger strains compared to P and L waves (O'Rourke and Liu 1999). Therefore, the dynamic response of buried pipelines under transient ground deformations are predominantly induced by the S and R waves. In the absence of detailed information, the general assumption is that S waves dominate within short epicentral distances, whereas R waves are the dominant type for longer epicentral distances. Determination of the contribution of S and R waves to the peak ground motion parameters is not straightforward and involves performing detailed seismological studies (ALA 2001). Due to several latent complexities in the seismic wave propagation, there is not a unified definition for the "short" and "long" epicentral distances. For example, epicentral short distances such as 2 to 5 focal depths (ASCE 1984), twice of the thickness of the earth's crust (Kramer 1996) and 20 km (ALA 2001) are suggested in the literature.

Seismic waves are characterized by their apparent propagation velocity with respect to ground surface, C_w , and the associated soil particles peak motion parameters such as peak

ground acceleration (PGA) and peak ground velocity (PGV) (Hindy and Novak 1979). The generated ground strains are in inverse relationship to C_w , meaning that R waves that travel slower than S waves develop larger strains. The soil particles when affected by S waves vibrate along lines perpendicular to the direction of the wave propagation; they follow a vertical elliptical shape and experience vibrations in perpendicular and parallel directions to the wave propagation of the R waves (Bolt 1993). Not considering the vertical components of the apparent seismic waves in the studies, the soil particle vibration directions, regardless of the wave type can be resolved into two horizontal components. Under this assumption, the pipeline response can be analyzed for horizontal wave propagation direction at an angle of incidence α with respect to the pipeline axis (Figure 4-1).

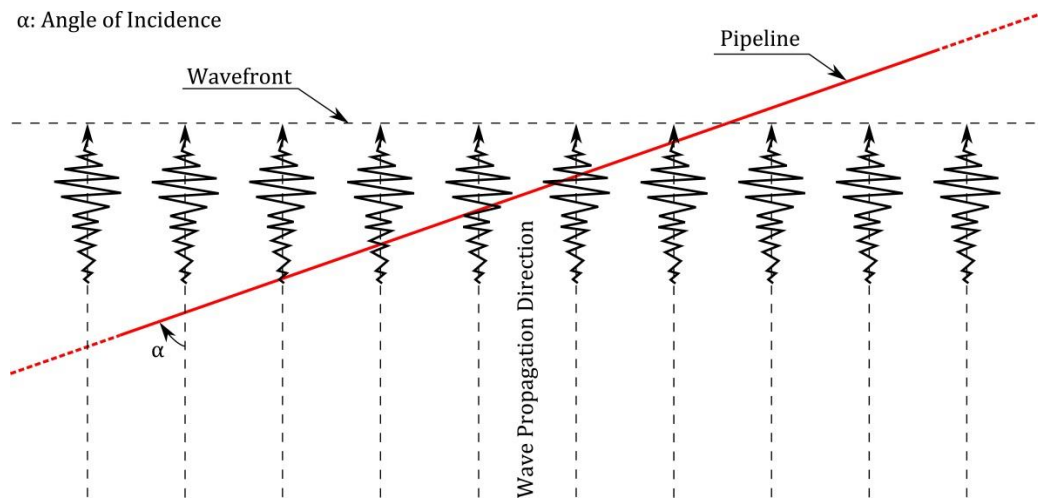


Figure 4-1: Top view of a pipeline impacted by seismic waves propagating in a homogeneous medium with the angle of incidence α .

The distinction between S and R waves is solely made based on their C_w values and direction of soil particles vibration with respect to wave propagation direction. C_w is related to the shear wave velocity of the surficial soils (C_s) and the angle of incidence of the S wave with respect to the vertical (γ_s) as follows (O'Rourke et al. 1982):

$$C_w = \frac{C_s}{\sin \gamma_s} \quad (4-1)$$

Based on the estimated C_w of S waves for some major seismic events in California and Japan, O'Rourke and Liu (1999) reported the range of 2.1 to 5.3 km/sec with an average of 3.4 km/sec. For the design purposes, the American Lifelines Alliance (ALA) suggests a conservative C_w estimate for S waves of 2 km/sec.

In case of R waves, since they are surface waves C_w can be assumed equal to their phase velocity, C_{ph} , (O'Rourke and Liu 1999). In fact, C_{ph} represents the velocity at which a transient vertical disturbance with frequency f is radiated through the ground surface. Therefore, for R waves and a given frequency f , C_w can be written as,

$$C_w = \lambda \cdot f \quad (4-2)$$

where, λ is the wave length. Analytical and numerical procedures are available in the literature to determine the variations of C_w with frequency (Haskell 1953, and O'Rourke et al. 1984). For example, for a single layer underlain by a stiff half space with 6 times larger shear wave velocity, O'Rourke et al. (1984) suggest C_w values between C_s and $5.25C_s$ of the top soft layer. Therefore, the lower bound which is equal to the average shear wave velocity of the soft layer represents the critical value of C_w . ALA (2001) suggests $C_w=0.5$ km/sec as a conservative selection for the R wave propagation velocity.

Having defined the seismic wave apparent horizontal velocity C_w , the wave propagation velocity along the pipeline, C_{wp} , can be expressed according to Figure 4-1 as follows,

$$C_{wp} = \frac{C_w}{\cos \alpha} \quad (4-3)$$

4.3 Discontinuous permafrost site response

Equation (4-3) assumes that the pipeline undergoes fully correlated ground motion that is incoherent due to a time-lag. In the following, the pipeline response will be analysed considering additional spatial variability of the ground motion due to discontinuous permafrost conditions typical for northern regions. The first step toward this goal is the study of seismic site response in these regions.

4.3.1 The site geology

The Northern Canadian Mainland Sedimentary Basin, referred to as the Mackenzie Valley, comprises seven sedimentary areas: Anderson-Horton Plain, Colville Hills, Peel Basin, Mackenzie Plain, Great Bear Plain, Great Slave Plain and Liard Plateau (Drummond 2012). These areas are mostly covered by glacial and postglacial Quaternary deposits, e.g., till, lacustrine and glaciofluvial silt, clay and sand, with a thickness that varies from a few centimeters to over 30 meters (Aylsworth et al. 2000).

There are still knowledge gaps in mapping spatial and temporal permafrost conditions and soil-pipe interactions in cold regions (Lawrence 2004). The geophysical surveys along the Norman Wells pipeline route in the Mackenzie Valley determined the state of transitions between the frozen and unfrozen terrains for the design of the pipeline against frost heave- and thaw settlement-induced displacements (Kay et al. 1983). During trenching, the geotechnical and thermal conditions of the ground at 9000 points were recorded along the same route. The compiled “ditchwall” database and the geophysical study results were interpreted by Nixon et al. (1991) and Geo-engineering (M.S.T.) Ltd. (1992). Figure 4-2 shows the distribution of the widths of frozen and unfrozen portions, denoted by W_f and W_u , respectively, encountered along the pipeline route. The distance was measured from Norman Wells to the north toward Zama to the south. As it can be seen, the portions of frozen ground are considerably higher to the north.

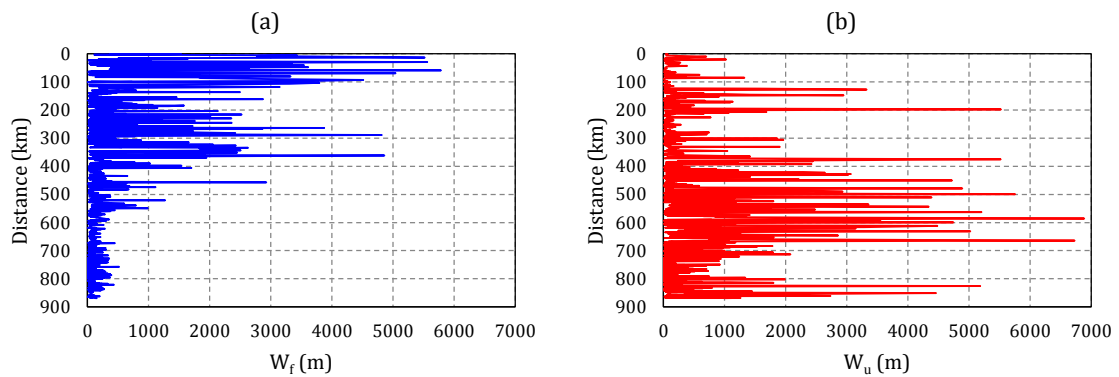


Figure 4-2: Distribution of width of (a) frozen parts (W_f), and (b) unfrozen parts (W_u) along the Norman Wells oil pipeline based on geophysical surveys of Kay et al. (1983). The distance is measured from Norman Wells toward Zama.

The distribution of W_f and W_u can be presented by the generalized extreme value (GEV) probability density function (PDF) (Kotz and Nadarajah 2000):

$$f(x|k, \mu, \sigma) = \left(\frac{1}{\sigma}\right) \exp\left\{-\left[1 + k\left(\frac{x-\mu}{\sigma}\right)\right]^{-\frac{1}{k}}\right\} \left[1 + k\left(\frac{x-\mu}{\sigma}\right)\right]^{-1-\frac{1}{k}} \quad (4-4)$$

where, k , μ and σ are the shape, location and scale parameters, respectively, and $1 + k\left(\frac{x-\mu}{\sigma}\right) > 0$. Figure 4-3 shows the GEV distributions in 100 km intervals of the Norman Wells to Zama oil pipeline route. The corresponding parameters are given in Table 4-1. The Kolmogorov-Smirnov test is used to evaluate the goodness-of-fit (Appendix C).

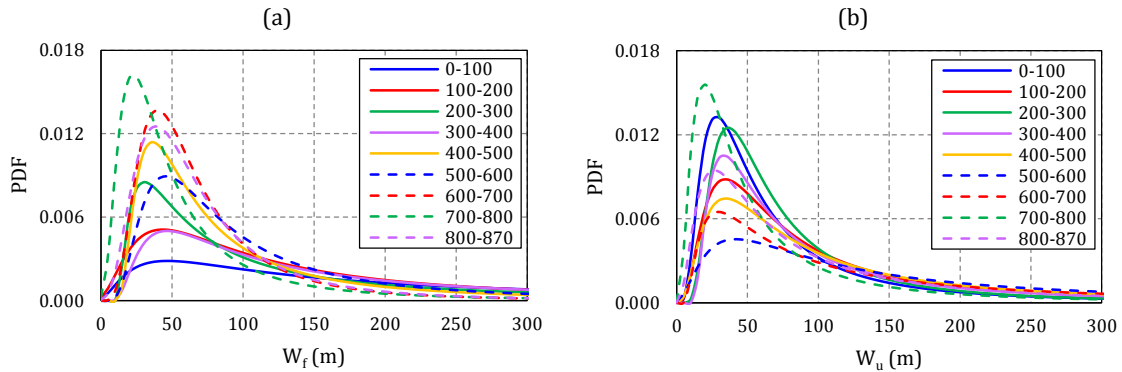


Figure 4-3: Generalized extreme value distributions of (a) W_f , and (b) W_u in 100 km intervals of the Norman Wells to Zama oil pipeline route. The distance is measured from Norman Wells, Northwest Territories, toward Zama, Alberta, Canada.

Table 4-1: GEV distribution parameters of W_f and W_u in 100 km intervals of the Norman Wells to Zama oil pipeline route.

Kilometerpost range	W_f					W_u				
	k	σ	μ	Mean (m)	SD* (m)	k	σ	μ	Mean (m)	SD* (m)
0-100	1.37	252.7	174.7	1056	1468	0.67	33.3	42.5	118	205
100-200	0.91	99.9	92.4	356	594	0.78	53.5	59.2	222	567
200-300	1.20	73.8	68.2	368	666	0.61	34.4	50.5	116	181
300-400	1.13	118.3	106.6	458	712	0.94	49.2	57.4	269	638
400-500	0.79	41.5	55.5	150	267	0.90	67.7	67.6	328	765
500-600	0.63	48.5	66.0	144	170	1.08	126.3	105.6	537	1036
600-700	0.38	28.6	48.4	80	64	1.28	103.0	81.8	479	872
700-800	0.54	25.7	32.4	67	69	0.73	29.4	32.6	103	191
800-870	0.36	31.1	47.7	80	65	0.90	53.4	52.6	244	591

* SD stands for the standard deviation.

4.3.2 Experimental study

The ground shaking can be altered by the local site effects from unconsolidated sediments and presence of permafrost conditions (Hyndman et al. 2005). In Chapter 3 the site response in discontinuous permafrost was simulated experimentally and analytically. The response of small-scale models was investigated by shaking table tests (Figure 4-4a). The discontinuous permafrost conditions were represented with intermittent cemented blocks buried in sand. Figure 4-4a shows a parallel block configuration that satisfies plane strain conditions with respect to the direction of shaking. Several models that satisfy plane strain conditions were tested. Their measured responses were then utilized to calibrate numerical models that were established employing FLAC software (Itasca Consulting Group, Inc. 2002). Based on the obtained experimental and numerical results, the effects of parameters such as W_u , W_f , shear wave velocity of frozen soil (V_{sf}) and number of frozen blocks on the site response were investigated. It was concluded that the site response at the top of the frozen blocks is generally higher than that at the top of the unfrozen parts and also, W_u , W_f and V_{sf} are the most significant parameters. Accordingly, PGA_f at the top of frozen blocks, and unfrozen soils (at the middle of span), PGA_u , are functions of W_f and W_u , respectively. Also, PGA_f is inversely related to V_{sf} , whereas, PGA_u is almost independent of V_{sf} .

Next, the response of an experimental model in which the plane strain conditions were violated, was investigated (Figure 4-4b). The satisfactory agreement between the results obtained from plane and non-plane strain conditions showed that plane strain conditions along the shaking direction can be a reasonable assumption for estimation of the parallel-to-excitation component of the site response.

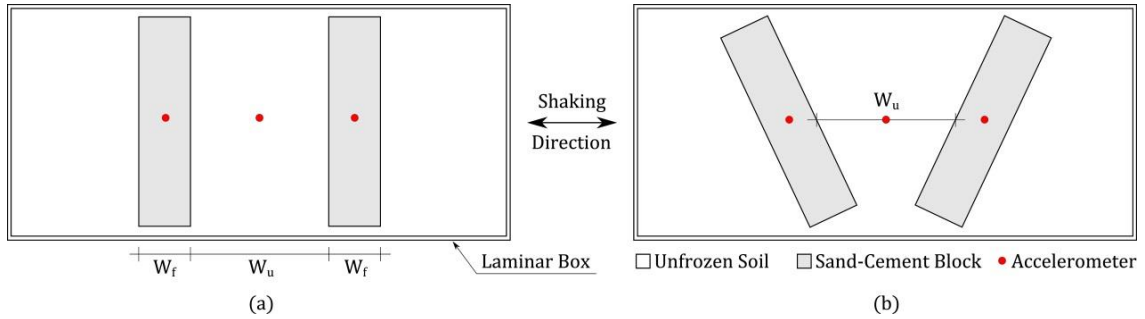


Figure 4-4: Top view of the shaking table test setups and the configurations of permafrost representing buried blocks for (a) plane strain, and (b) 3D cases used in Chapter 3 in site response study.

4.3.3 The proposed model

According to the findings of Chapter 3, a predictive model is proposed herein to describe the observed intermittent differential ground motions (IDGM) in discontinuous permafrost regions. The PGA component aligned with the shaking direction can be calculated according to the PGA_f and PGA_u expressions that will be introduced in this section. It is assumed that PGA_f on top of the frozen blocks is constant, whereas PGA_u is equal to the PGA_f at the contact with the adjacent frozen blocks to gradually decrease to the minimal value at the mid-distance between the frozen blocks. This model is graphically illustrated in Figure 4-5.

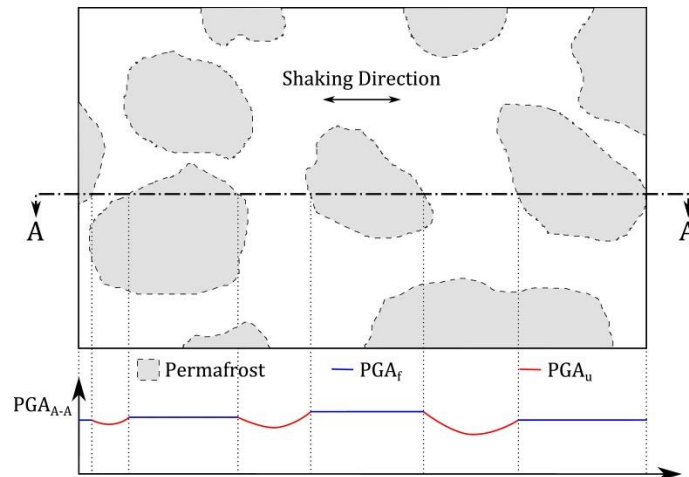


Figure 4-5: Top view of a hypothetical discontinuous permafrost region and the distribution of PGA along the Section A-A.

The variation of PGA_f with respect to W_f can be characterized by two important boundary values at $W_f=0$ and $W_f \rightarrow \infty$ (Figure 4-6a). PGA_f at $W_f=0$ represents the site response of unfrozen deposits (PGA_{u0}); it attains its maximal value for a given W_f ; and with W_f approaching infinity it equals the site response of continuous permafrost (PGA_{f0}). The variation of PGA_u with respect to W_u can be characterized by two boundary values as well (Figure 4-6b): PGA_u equals PGA_f for $W_u=0$; and as W_u approaches infinity, PGA_u equals the response of the unfrozen site (PGA_{u0}).

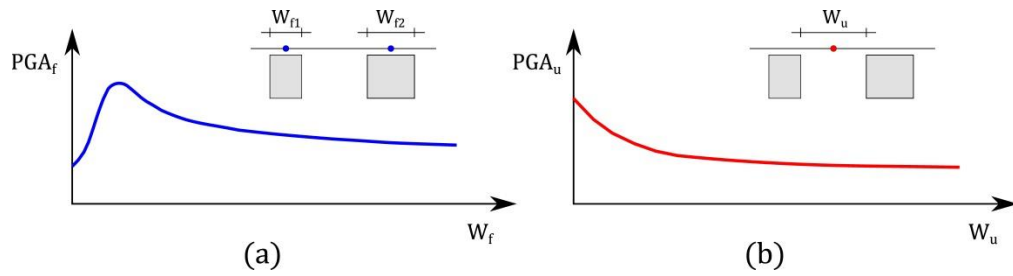


Figure 4-6: PGA at the top of (a) frozen blocks, and (b) unfrozen soil (at the middle of unfrozen span) based on the experimental and numerical findings of Chapter 3.

Based on the experimental and analytical results, PGA_f can be expressed as a function of W_f by the following expression,

$$PGA_f = PGA_{u0} + \frac{(\eta W_f)^2}{\mu \sqrt{[1 - (\eta W_f)^2]^2 + (2\eta \xi W_f)^2}} \quad (4-5)$$

where, η , μ and ξ are the regression parameters which provide the best fit to the site response data.

Figure 4-7a illustrates the numerical results (Chapter 3) and the PGA_f vs. W_f relationship computed for $PGA_{u0} = 0.20$, $\eta = 0.19$, $\mu = 5.90$ and $\xi = 0.32$. On the other hand, PGA_u at the mid-distance between the frozen blocks can be presented by the following function,

$$PGA_u = PGA_{u0} + (PGA_f - PGA_{u0}) \exp(-\beta W_u) \quad (4-6)$$

where, β is a site-dependent regression parameter and PGA_f is determined from Equation (4-5). This function computed for $PGA_{u0} = 0.20$, $PGA_f = 0.42$ and $\beta = 0.025$ is shown against the numerical results in Figure 4-7b.

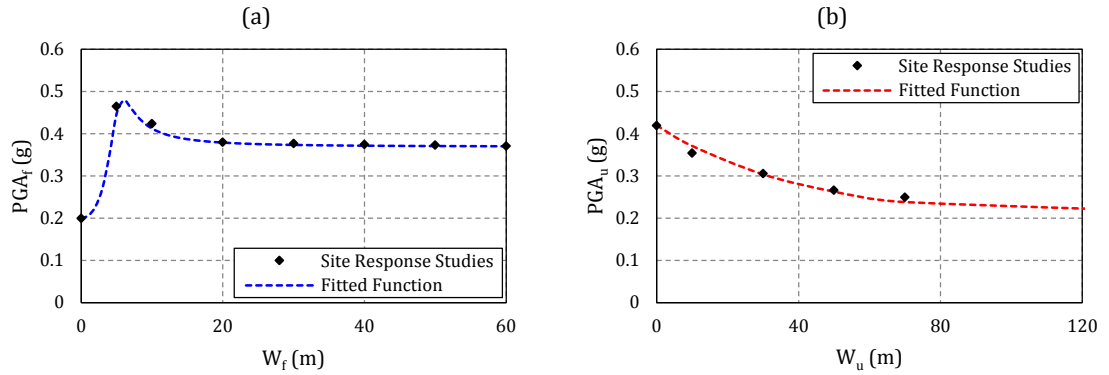


Figure 4-7: The functions fitted to the simulated site response results of Chapter 3: (a) PGA_f , and (b) PGA_u for $PGA_f=0.42g$.

4.3.4 Model corrections

Permafrost shear wave velocity, V_{sf} : Even though PGA_f is inversely proportional to the shear wave velocity of the frozen block, V_{sf} has no appreciable impact on PGA_u . Within the practical range of V_{sf} , 1000 to 2500 m/sec, using the results of Chapter 3 and selecting $V_{sf}=1500$ m/sec as the baseline, a correction factor of shear wave velocity for PGA_f can be given as:

$$C_V = -0.0969 \left(\frac{V_{sf}}{1500} \right) + 1.0969 \quad (4-7)$$

Seismic input and deposit thickness: The effect of the base (bedrock) excitation intensity (PGA_r) on the frozen and unfrozen ground surface response (PGA_f , PGA_u), was experimentally investigated in Chapter 3. The relationships between the PGA on bedrock (PGA_r) and the PGA ratio at the surface, PGA_f/PGA_u , for the simulated deposit thickness of $H=40$ m under three levels of base excitations: 0.15, 0.3 and 0.5g were presented. It was shown that the PGA_f/PGA_u ratio increases by the increase of PGA_r . Utilizing the calibrated FLAC model, variations of PGA_f and PGA_u with deposit thickness ($H=10, 20, 30$ and 40 m) are numerically studied herein. A set of seismic base excitations is used as an input motion and the average of the PGA responses for each model is considered. The set of selected accelerograms consisted of representative seismic records from Western North America (WNA) with different frequency contents: M6.7 Nahanni earthquake (Canada, 1985), M7.9 Denali earthquake (USA, 2002), and M5.3 Nelchina earthquake

(USA, 2004) occurred close to or within the permafrost regions; and California’s M6.9 Imperial Valley (1940), M6.7 Northridge (1994), M7.0 Cape Mendocino (1992), and M6.9 Loma Prieta (1989) earthquakes (PEER 2016, and USGS 2016). The acceleration response spectra of these ground motions are shown in Figure 4-8.

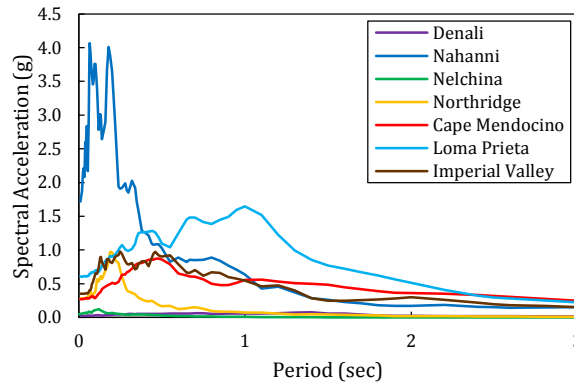


Figure 4-8: The acceleration response spectra of the input motion records. Data from PEER (2016) and USGS (2016).

Spectral scaling was employed over the fundamental site period to standardize the seismic input. The results of the simulations are given in Figure 4-9.

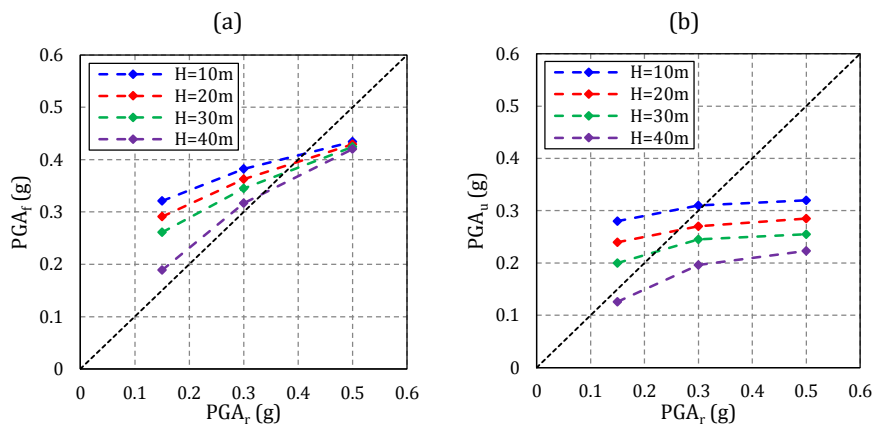


Figure 4-9: Variations of the PGA response of (a) frozen and (b) unfrozen parts with PGA of the bedrock, PGA_r and deposit thickness (depth to bedrock), H .

It can be observed in Figure 4-9 that under the considered “low” to “moderate” input acceleration, the response of the frozen soils is amplified compared to that of the bedrock,

$PGA_f/PGA_r > 1$. The response of frozen soils is de-amplified under the considered “high” input acceleration, due to the degradation of the soil stiffness properties. The de-amplification in unfrozen soils occurs at lower input acceleration levels. These site responses are in favourable agreement with the relationship between the peak ground accelerations at bedrock and those at surface of deposits suggested by Idriss (1990).

4.4 Pipeline response to wave propagation

Simplifying seismic wave propagation to the travel of harmonic waves in a linear elastic homogeneous medium and assuming identical displacements for the pipeline and the ground, Newmark (1967) proposed the first solution for the pipeline response to wave propagation. Yeh (1974) generalized the Newmark’s solution by incorporating the effect of different types of seismic waves with arbitrary angles of incidence. Accordingly, for waves travelling with apparent velocity C_w , angle of incidence of α , and direction of the soil particles motion perpendicular to the wave propagation, the maximum axial (ϵ_a) and bending (ϵ_b) strains induced in the ground and the pipeline can be expressed as follows,

$$\epsilon_a = \frac{PGV}{C_w} \sin \alpha \cos \alpha \quad (4-8a)$$

$$\epsilon_b = \frac{D.PGA}{2C_w^2} \cos^3 \alpha \quad (4-8b)$$

On the other hand, for direction of the soil particles motion parallel to the wave propagation, ϵ_a and ϵ_b can be calculated from,

$$\epsilon_a = \frac{PGV}{C_w} \cos^2 \alpha \quad (4-9a)$$

$$\epsilon_b = \frac{D.PGA}{2C_w^2} \cos^2 \alpha \sin \alpha \quad (4-9b)$$

In Equations (4-8) and (4-9), the axial strains are a function of the peak ground velocity, PGV, whereas the bending strains are a function of peak ground acceleration, PGA. Neglecting the soil-pipe interactions (SPI), when the pipeline is considerably stiffer than the neighbouring soils or is subject to intense shakings, this solution results in unrealistically large strains.

4.4.1 Soil-pipe interaction

The finite element modelling is employed herein to account for SPI and overcome the limitations of the above method in modelling soil heterogeneities. The soil-pipe interaction is numerically simulated applying the dynamic nonlinear Winkler model where: the pipeline segment is discretized by frame elements with lumped masses, the soil stiffness and hysteretic damping are accounted for by nonlinear inelastic springs and the soil viscoelastic damping is modelled by viscous dashpots (Figure 4-10). The pipeline structural nodes have 6 degrees of freedom (DOF) among which the 3 translational DOFs are considered in the dynamic analysis. The assembled global mass and stiffness matrices of a pipeline segment are respectively denoted by \mathbf{M}_p and \mathbf{K}_p , where, the former matrix is diagonal because the masses considered to be lumped at the nodes.

The soil spring force-displacement relationships suggested by the ALA (2001) are employed in the model. The global soil stiffness matrix, \mathbf{K}_s , is assembled by summing up the nodal spring stiffness factors corresponding to the translational DOFs.

In the analysis, only the soil damping is considered since the pipeline damping is comparatively much lower. The soil damping is determined from the imaginary part of the buried pipe's complex dynamic soil stiffness developed by Hindy and Novak (1979) as follows,

$$c_l = \frac{G\bar{S}_{u2}D}{2V_s} \quad (4-10a)$$

$$c_a = \frac{G\bar{S}_{v2}D}{2V_s} \quad (4-10b)$$

where, c_l and c_a are, respectively, the equivalent viscous damping per unit length in the lateral and axial directions, G is the soil shear modulus, V_s is the shear wave velocity, D is the pipe outer diameter, and, \bar{S}_{u2} and \bar{S}_{v2} are the dimensionless damping parameters associated with the lateral and axial directions, respectively. They are shown in Figure 4-11 as functions of the ratio between the burial depth and D . The global soil damping matrix, \mathbf{C}_s , is assembled computing c_l and c_a for each element.

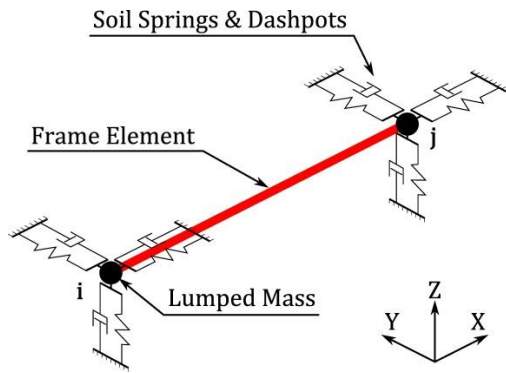


Figure 4-10: A dynamic Winkler element i-j for buried pipes comprised of frame element with lumped masses, soil springs and dashpots.

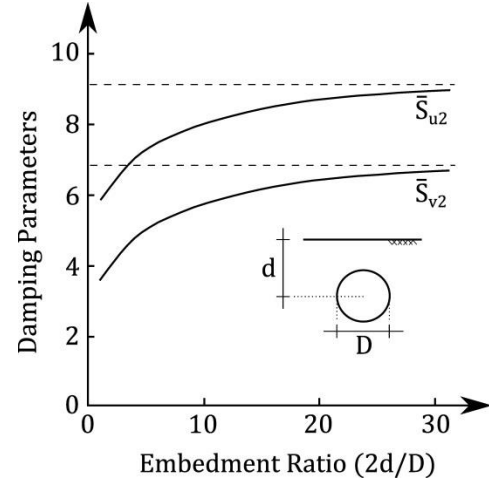


Figure 4-11: Dimensionless parameters of soil damping for lateral (\bar{S}_{u2}) and axial (\bar{S}_{v2}) directions. (Adapted from Hindy and Novak 1979)

4.4.2 Equation of motion

The displacement response of buried pipeline subject to earthquake-induced multiple support excitations is shown in Figure 4-12. The response is composed of two components, quasi-static and dynamic components as follows,

$$\mathbf{U} = \mathbf{U}_{qst} + \mathbf{U}_{dyn} \quad (4-11)$$

where, \mathbf{U} , \mathbf{U}_{qst} and \mathbf{U}_{dyn} are the vectors of the total, quasi-static and dynamic displacements, respectively. The quasi-static response at each time step is obtained by statically applying the corresponding ground displacement vector, \mathbf{U}_g :

$$(\mathbf{K}_p + \mathbf{K}_s)\mathbf{U}_{qst} = \mathbf{K}_s\mathbf{U}_g \quad (4-12)$$

where, the quasi-static response relative to the condition at rest is given by:

$$\mathbf{U}_{qst} = (\mathbf{K}_p + \mathbf{K}_s)^{-1}\mathbf{K}_s\mathbf{U}_g \quad (4-13)$$

According to Figure 4-12, the quasi-static response can be expressed as the sum of the ground deformation and quasi-static response relative to the deformed ground, \mathbf{U}_{qst}^g ,

$$\mathbf{U}_{qst} = \mathbf{U}_g + \mathbf{U}_{qst}^g \quad (4-14)$$

Rearranging the terms and substituting \mathbf{U}_{qst} from Equation (4-13) into Equation (4-14), \mathbf{U}_{qst}^g is obtained as,

$$\mathbf{U}_{qst}^g = \mathbf{U}_{qst} - \mathbf{U}_g = \left[(\mathbf{K}_p + \mathbf{K}_s)^{-1} \mathbf{K}_s - \mathbf{I} \right] \mathbf{U}_g \quad (4-15)$$

To determine the dynamic part of the response, the equation of motion is derived recalling that the pipeline inertial and internal resisting forces depend on the total response and the soil damping and resistance are functions of the dynamic response. The equation of the dynamic motion is given by Hindy and Novak (1979):

$$\mathbf{M}_p \ddot{\mathbf{U}} + \mathbf{C}_s \dot{\mathbf{U}}_{dyn} + \mathbf{K}_p \mathbf{U} + \mathbf{K}_s \mathbf{U}_{dyn} = \mathbf{0} \quad (4-16)$$

The total displacement, \mathbf{U} , is obtained, combining Equations (4-11) and (4-14) as follows,

$$\mathbf{U} = (\mathbf{K}_p + \mathbf{K}_s)^{-1} \mathbf{K}_s \mathbf{U}_g + \mathbf{U}_{dyn} \quad (4-17)$$

The equation of motion can then be expressed with respect to a single variable, i.e.,

$$\mathbf{M}_p \ddot{\mathbf{U}}_{dyn} + \mathbf{C}_s \dot{\mathbf{U}}_{dyn} + (\mathbf{K}_p + \mathbf{K}_s) \mathbf{U}_{dyn} = \mathbf{P}_{eff} \quad (4-18)$$

where, the effective load vector, \mathbf{P}_{eff} , is defined as:

$$\mathbf{P}_{eff} = - \left[\mathbf{M}_p (\mathbf{K}_p + \mathbf{K}_s)^{-1} \mathbf{K}_s \ddot{\mathbf{U}}_g + \mathbf{K}_p (\mathbf{K}_p + \mathbf{K}_s)^{-1} \mathbf{K}_s \mathbf{U}_g \right] \quad (4-19)$$

Therefore, according to Equation (4-19) the time histories of ground displacement and acceleration are necessary to perform a dynamic analysis on a pipeline segment.

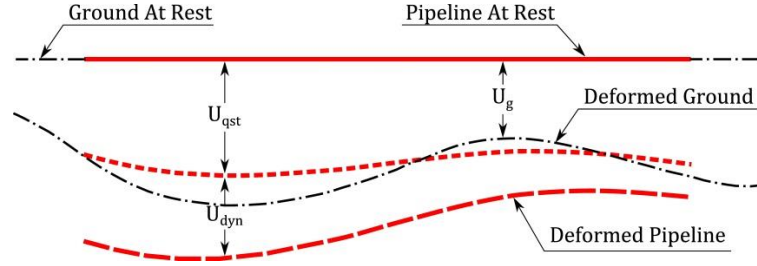


Figure 4-12: Top view of the displacement response of a pipeline segment subjected to transient ground deformations. U_{gst} and U_{dyn} represent the quasi-static and dynamic parts of the response, respectively, and U_g is the ground deformation.

4.4.3 Response calculation and damage detection

A large deformation nonlinear finite element program was developed in Matlab (The MathWorks, Inc. 2011). It applies the Wilson's theta time domain step-by-step analysis to calculate the pipeline response. The program incorporates the effect of geometrical and material nonlinearities employing a special plastic hinge model and determines the onset of potential damage in the pipe. The nonlinear behaviour of the pipe is simulated at the location of the plastic hinge discretizing its cross-section with a number of nonlinear frame elements. The Ramberg-Osgood equation (Ramberg and Osgood 1943) is used to determine the material nonlinearity of the elements and enables the program to compute the longitudinal stresses and strains to detect the tensile rupture and/or local buckling failure modes. The ALA's tensile strain limit of 0.5% and the compressive strain limit of 75% of the suggested value presented for the pipes under permanent ground deformation are considered as threshold values under wave propagation. According to the Canadian standard for oil and gas pipeline systems (CAN-CSA Z662 2003), the ultimate compressive strain under permanent ground deformation is obtained from the following equation,

$$\epsilon_c^{ult} = 0.5 \left(\frac{t}{D} \right) - 0.0025 + 3000 \left[\frac{(p_{int} - p_{ext})D}{2tE} \right]^2 \quad (4-20)$$

where, t is the pipe wall-thickness, D is the pipe outside diameter, E is the steel modulus of elasticity, and p_{int} and p_{ext} are the internal and external pressures, respectively.

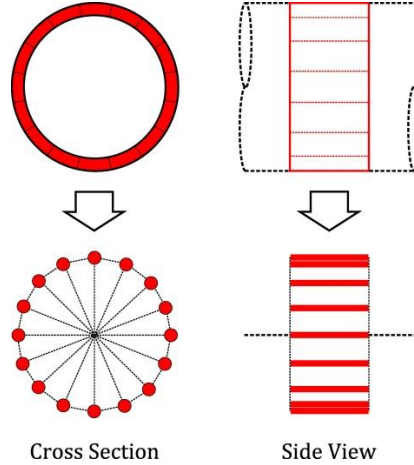


Figure 4-13: Discretization of pipe cross-section at plastic hinge.

The geometric nonlinearity of the pipe cross-section under bending moment, referred to as ovalization, causes premature failure. ALA (2001) defines the ovalization factor as,

$$OV_{ALA} = \frac{D - D_{min}}{D} \quad (4-21)$$

with the maximum permissible value of $OV_{ALA}=0.15$. CAN-CSA Z662, on the other hand, uses the following equation:

$$OV_{CSA} = 2 \left(\frac{D_{max} - D_{min}}{D_{max} + D_{min}} \right) \quad (4-22)$$

with maximum limit of $OV_{CSA}=0.06$. In these equations D_{max} and D_{min} are the maximum and minimum outside diameters of the pipe when it is deformed under bending moment. Also, in Chapter 2 ovalization-curvature relationships for several cases of buried pipes were studied and their ultimate ovalization factors were presented. In the current chapter, the ovalization is simulated by the step-by-step evolution of the spatial configuration of the nonlinear elements according to ovalization-curvature relationships of Chapter 2. In cases of inelastic ovalization under the cyclic loading, the accumulated permanent ovalization is modelled applying the results of Shaw and Kyriakides (1985). Figure 4-14 shows the computed normalized moment-curvature and ovalization-curvature diagrams for a pipe made of X65 steel with $D/t=96$ subjected to cyclic bending moment.

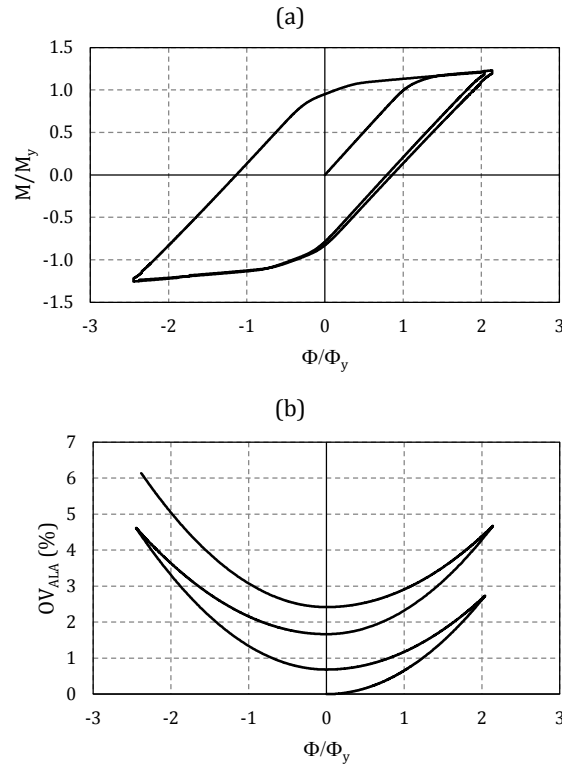


Figure 4-14: (a) The moment-curvature and (b) the ovalization-curvature for a pipe made of X65 steel with $D/t=96$ subjected to cyclic bending moment. The bending moment and curvature are normalized with respect to the yield moment and curvature, M_y and Φ_y , respectively.

4.4.4 Validation

An example of a 500 m-length segment of straight pipeline with $D=1.0$ m and $D/t=100$, buried 1.5 m below the ground surface in homogenous soil and made of X52 steel is considered to evaluate the performance of the developed software. The assumed tensile strain limit is 0.0050 and the compressive strain limit obtained from Equation (4-20) multiplied by 0.75 is 0.0019. The pipeline is subjected to horizontal components of S and R harmonic waves with different angles of incidence varying from 0 to 90 degrees. The waves propagate with frequency of 2 Hz, peak acceleration of 0.35g and apparent propagation velocities of 2 and 0.5 km/sec for S and R waves, respectively. To check the influence of the soil stiffness on the SPI, three soil types are considered: loose, medium dense and very dense soil or rock. Parameters characterizing the first two cases are given

in Table 4-2. For the case of very dense soil, apparently there is no interaction between the pipe and soil, i.e., both have same dynamic responses (intensity and phase). In this case, the theoretical solution of Newmark (1967) and Yeh (1974) is applicable to evaluate the response.

Table 4-2: Parameters of loose and medium dense soils denoted by L and D in this study.

Soil Type	ϕ (Deg)	c (kPa)	γ (kN/m ³)	V_s (m/sec)
L	25	2.5	16	100
D	35	2.5	18	300

The results are presented in Figure 4-15; Figures 4-15a and b show the responses under S waves and Figures 4-15c and d represent those under R waves. The figure shows that the bending strains are about two orders of magnitude smaller than the axial strains. This is in agreement with the results of previous studies suggesting that the axial strains are dominant in the response of pipelines to wave propagation (Yeh 1974, Ariman and Muleski 1981, O'Rourke and Liu 1999, and Scandella and Paolucci 2010). As well, comparison of bending and axial strains resulting from the two wave types reveals that the effect of SPI on the bending strains is negligible, whereas its effect on the axial strains is important. The axial strains determined from the theoretical solution, shown in Figures 4-15b and d with dashed line, represent a conservative response compared to the axial strains obtained considering SPI, i.e., loose and dense soils. These results demonstrate that when buried in loose soils, the pipeline response is less severe than that when it is buried in dense soils.

The above results are compatible with the numerical results obtained by Mavridis and Pitilakis (1996). However, they are different from those reported by Hindy and Novak (1979). All the reported results, except for the axial strains under R waves, show small differences with those calculated from the Newmark's solution; however, this is not the case for the results of Hindy and Novak (which are not plotted in Figure 4-15). This is due to their unrealistic assumption that the apparent wave propagation velocities of the S and P waves are, respectively, equal to the soil shear and compressive wave velocities.

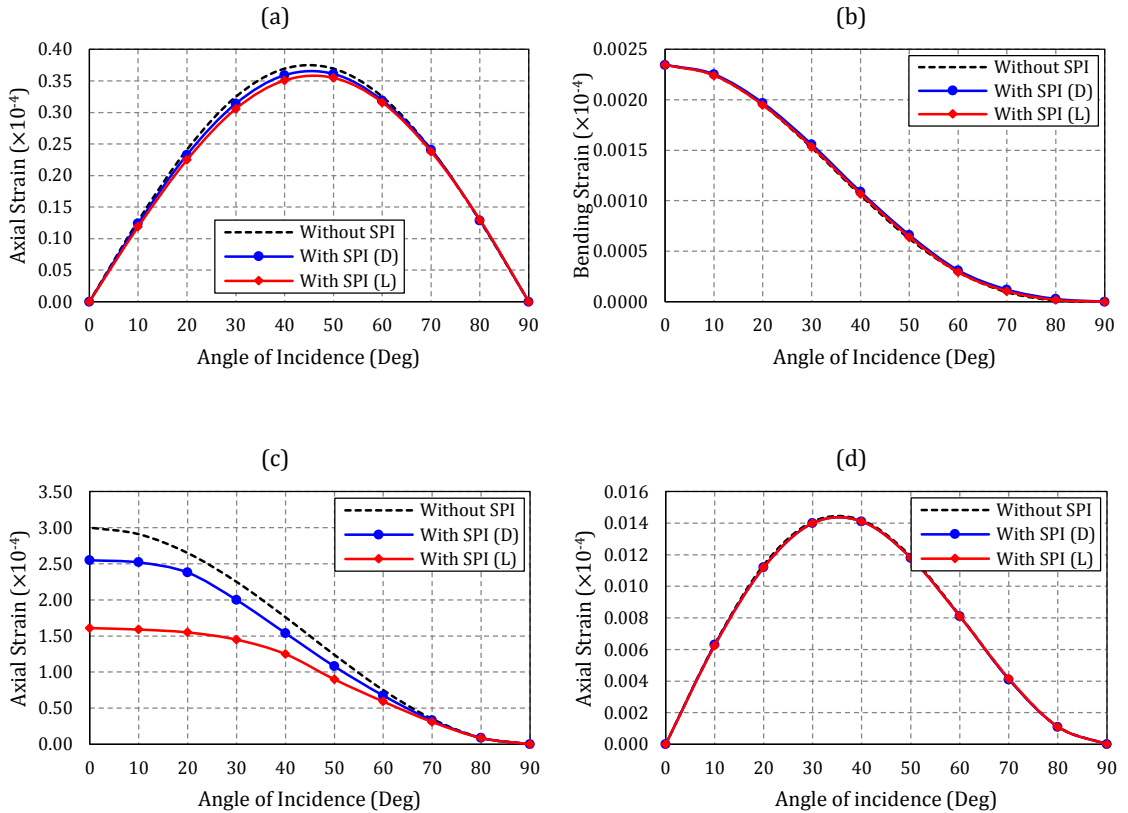


Figure 4-15: Response of a straight pipeline segment to S and R waves with and without considering soil-pipe interaction (SPI): (a) axial strains under S waves, (b) bending strains under S waves, (c) axial strains under R waves, and (d) bending strains under R waves.

4.5 Response to wave propagation in discontinuous permafrost

Following the validation of the developed software, it was employed to predict the seismic response of a buried pipeline in a discontinuous permafrost region. The dimensions of the frozen soil portions along the pipeline, even those located beyond the right-of-way's width, should be determined first. Then, according to Section 4.3 the IDGM along the wave propagation direction can be determined. For the purpose of preliminary design and damage assessment; however, it is sufficient to find IDGM by using the average dimensions of the frozen/unfrozen parts. Also, in the absence of detailed geophysical information, it can be assumed that the statistical distributions of

frozen/unfrozen parts' dimensions around a pipeline are isotropic, that is, the available statistical distributions of the frozen/unfrozen parts are applicable to wave propagation in all directions. The parameters associated with the Norman Wells oil pipeline route given in Table 4-1 were used. Two different permafrost scattering conditions, i.e., the intervals between kilometerposts 200 to 300 and 700 to 800 of the route, are considered which for the sake of brevity will henceforth be referred to as kmp 200-300 and kmp 700-800. In addition, to calculate the highest seismic strain demands, a soil thickness of 40 m which generates the largest PGA_f/PGA_u ratio (Figure 4-9) was considered.

Two conditions for burial depth were considered: (i) the pipe is fully buried in the active layer, and (ii) the pipe is fully/partly buried in the frozen layer. These conditions are illustrated in Figure 4-16. When buried in the active layer, the pipe is surrounded by unfrozen soil that provides identical support stiffness (ISS) along the pipeline (Sections C-C and D-D in Figure 4-16). On the other hand, when fully/partly buried in frozen parts of the ground, the intermittent characteristic of discontinuous permafrost provides a multiple support stiffness (MSS) along the pipeline in transverse and vertical directions (Sections B-B and C-C in Figure 4-16). However, in both cases the pipeline is subjected to IDGM. Both cases of ISS and MSS are considered in finding the seismic strain demand of the pipelines.

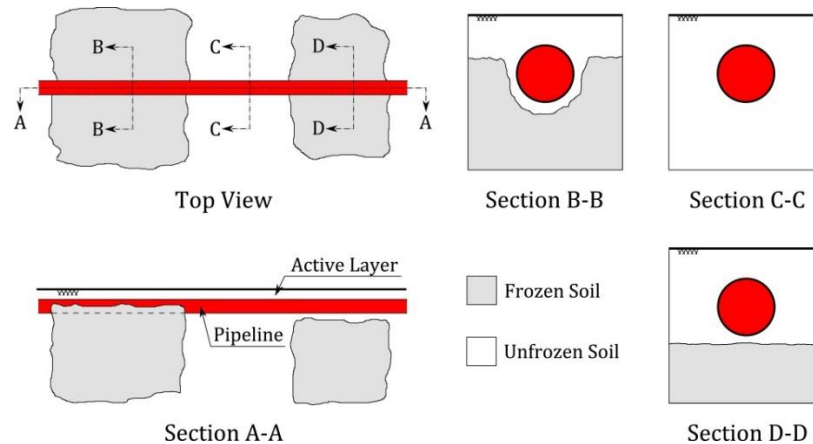


Figure 4-16: Different burial conditions considered in this study. Sections A-A to D-D indicate the longitudinal pipeline view, the partial burial, the unfrozen span burial, and the full burial in active layer, respectively.

4.5.1 Identical support stiffness (ISS)

An ISS pipeline ($D=1.0$ m, $D/t=100$ and $d/D=3.75$) was subjected to S and R waves with corresponding conservative apparent propagation velocities of 2 and 0.5 km/sec. Effect of dense and loose soils (Table 4-2) on the response was investigated. The results are plotted in Figure 4-17 (In all cases the ovalization factors were less than 0.5% and therefore are not presented). Compared to the responses under wave propagation in the homogeneous terrain (Figure 4-15), bending strains under S waves (Figure 4-17b) and axial strains under R waves (Figure 4-17c) show almost similar trends as functions of the angle of incidence. However, variations of axial strains under S waves (Figure 4-17a) and bending strains under R waves (Figure 4-17d) with the angle of incidence are different from those given in Figure 4-15. Here, in contrast to the case of homogeneous ground the mentioned strains corresponding to the angles of incidence that falling within the range of 60 to 90° do not approach zero. Since in that range of angle of incidence the wave propagation velocity along the pipeline drastically increases and tends to infinity at 90° (Equation 4-3), the wave propagation along the pipeline gradually transforms to rigid body motions. Therefore, in the case of homogeneous terrain the pipeline undergoes identical support excitations. However, due to IDGM the supports still experience multiple excitations and some level of strain develops in the pipe.

Magnitude of the strains obtained from homogeneous and non-homogeneous terrains are different, as well. Comparison of the maximum strains obtained from both terrain types reveals that increase of bending strains are considerably higher than axial strains (Table 4-3). Nevertheless, the axial strains are still one order of magnitude larger than the bending strains under both wave types.

Table 4-3: Comparison of the pipe strains obtained from homogeneous and non-homogeneous grounds.

Wave type	Soil type "D"		Soil type "L"	
	$\max\left(\frac{\epsilon_{a,ISS}}{\epsilon_a}\right)$	$\max\left(\frac{\epsilon_{b,ISS}}{\epsilon_b}\right)$	$\max\left(\frac{\epsilon_{a,ISS}}{\epsilon_a}\right)$	$\max\left(\frac{\epsilon_{b,ISS}}{\epsilon_b}\right)$
S	2.56	75.00	1.86	50.00
R	1.28	12.00	1.09	9.29

Note: Average of kmp 200-300 and kmp 700-800 responses are considered.

Another notable difference between the results obtained from homogeneous and non-homogeneous terrains is about the effect of soil density, where in the former terrain, only the axial strains under R waves were affected but in the latter case axial and bending strains under S and R waves are altered. Again, the looser the soil the smaller the pipe strains. Finally, no considerable difference is observed between the strains obtained from the two cases of geothermal conditions (permafrost scattering), i.e., kmp 200-300 and kmp 700-800 in Figure 4-17.

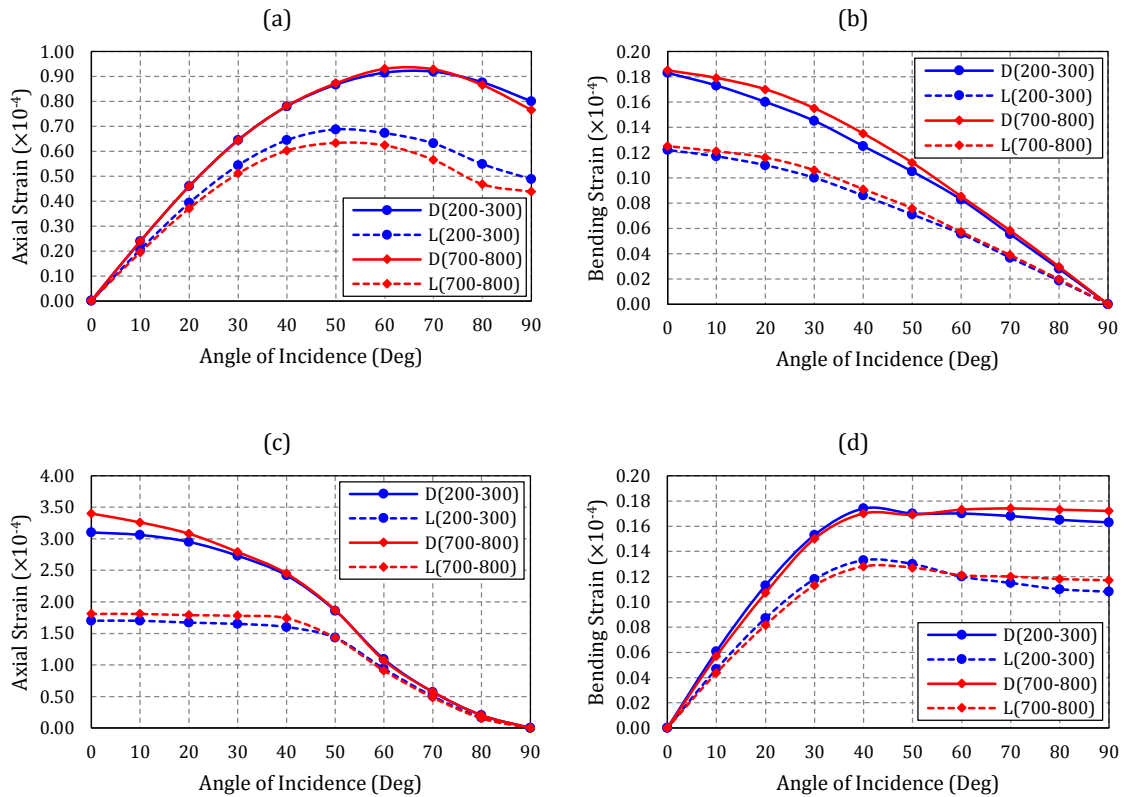


Figure 4-17: Response of an ISS straight pipeline segment to S and R waves: (a) axial strains under S waves, (b) bending strains under S waves, (c) axial strains under R waves, and (d) bending strains under R waves. D and L respectively represent dense and loose soils, and the kilometerpost of the considered intervals of the Norman Wells pipeline route are denoted in parentheses.

4.5.2 Multiple support stiffness (MSS)

Having higher temperature compared to the surrounding soil, the MSS buried pipes in permafrost regions are surrounded by a thin layer of unfrozen soil (Section B-B in Figure 4-16) which means in longitudinal direction ISS condition is confirmed. Also from previous section, applying the R waves with the apparent propagation velocity of 0.5 km/sec resulted in the most critical axial strains in the pipe. Consequently, response of the MSS pipelines only subjected to R waves is studied. The properties of frozen soil are assumed as: $V_{sf}=1500$ m/sec and $c=100$ kPa. The unit weight of soil and the angle of internal friction were assumed to be identical to those of the unfrozen soil. In Figure 4-18, results of analysis for the MSS and ISS pipelines buried in permafrost with average geothermal conditions of kmp 700-800 are compared (Again, in all cases the ovalization factors were less than 0.5% and therefore are not presented). As it can be seen in Figure 4-18a, due to having similar longitudinal soil stiffness distributions, the axial strains obtained from the two analyses are identical. However, in the case of dense and loose soils, the bending strains increased up to 41 and 67%, respectively (Figure 4-18b). Nevertheless, axial strains that did not change are still one order of magnitude larger than the intensified bending strains and therefore, remain critical for the safety evaluation.

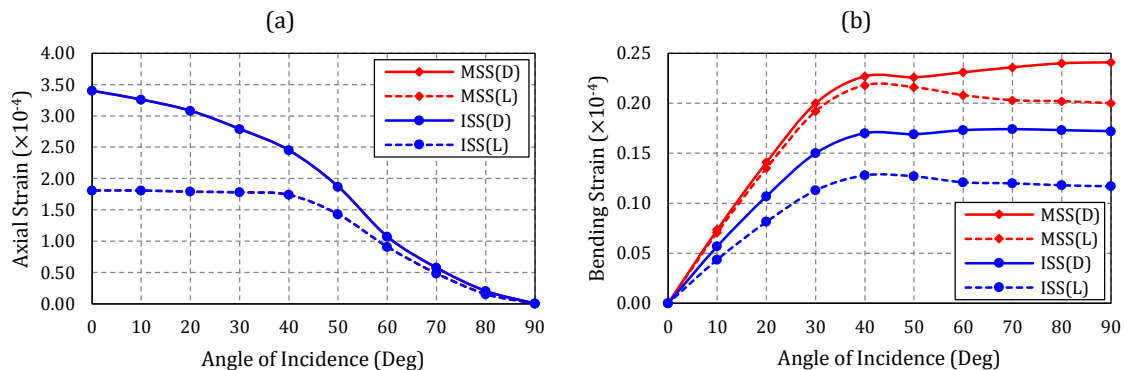


Figure 4-18: Response of a MSS straight pipeline segment to R waves buried in a terrain with average geothermal conditions of kmp 700-800: (a) axial strains, and (b) bending strains. D and L respectively represent dense and loose soils, and MSS and ISS stand for multiple and identical support stiffness pipelines, respectively.

4.5.3 Effect of frequency content

To evaluate the effect of soil particle vibration frequency on the strains, response of the pipeline subjected to R waves under three frequency levels of 1, 2 and 4 Hz was calculated. The results of this study, depicted in Figure 4-19, revealed that the induced strains are inversely proportional to the frequency of vibration of soil particles. The ovalization factors were also negligible.

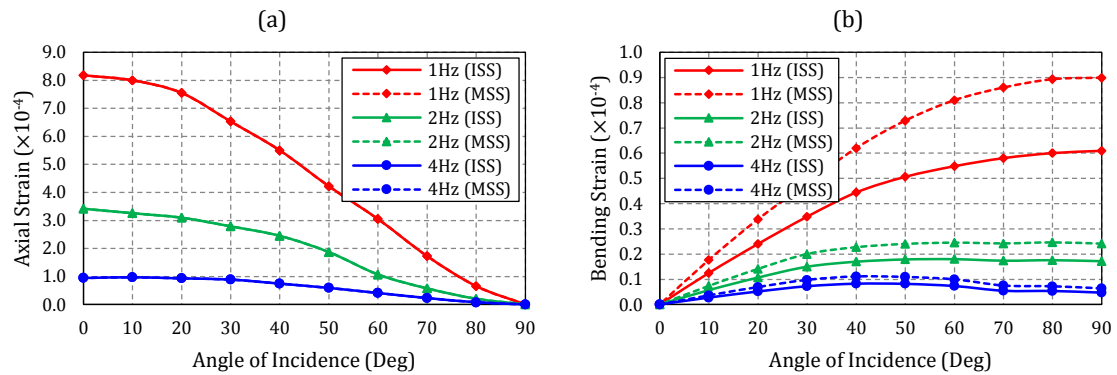


Figure 4-19: Effect of frequency content on the response of a straight pipeline segment to R waves: (a) axial strains, and (b) bending strains.

4.5.4 Effect of pipe dimensions and burial depth

According to Kyriakides and Corona (2007), the diameter and diameter to wall-thickness ratio of major onshore energy pipelines usually fall in the ranges of 0.9 to 1.6 m and 40 to 80, respectively. In all the presented results so far, the cross-sectional properties of the pipe as well as the burial depth were held constant, that is $D=1.0$ m, $D/t=100$ and $d=1.5$ m. To investigate the effect of pipe dimensions and burial depth, more analyses are performed on the pipes with lower bounds of D , D/t and d , i.e., 0.4 m and 40 and 0.7 m. It is assumed that the soil is dense and the pipeline has MSS condition. Under moderate level of base excitations and frequency of soil particles vibration the results are presented in Figure 4-20. From Figure 4-20a, the axial strains obtained for the small-diameter pipe in the D/t range of 40 to 100 are larger than those obtained for the large-diameter pipe in the same range of D/t . Consequently, the small-diameter slender pipes experience higher levels of strains during seismic events. On the other hand, as shown in Figure 4-20b the

bending strains induced in the large-diameter pipe are larger due to the fact that both pipes have virtually followed the ground motion in the dense soil. This is also in agreement with previous post-seismic strain estimations in large- and small-diameter pipes (Sakurai and Takahashi 1969).

The effect of burial depth is studied on the small diameter pipe with ($D/t=100$), which is subjected to larger axial strains. Two depths are considered: 1.5 m ($d/D=3.75$) and 0.7 m ($d/D=1.75$) and the results are plotted in Figures 4-20c and d. The maximum decrease in the respectively axial and bending strains of 25% and 2%, resulting from smaller burial depth, suggests that larger depths with larger axial strains induced in pipes are more critical.

To evaluate the possibility of rupture and buckling failures, the results should be compared with the ultimate strains corresponding to each case. According to Section 4.4.3, the ultimate tensile strain for all cases is equal to 0.0050, and the ultimate compressive strains calculated from Equation (4-20) for D/t of 40 and 100 when $p_{int}=p_{ext}=0$ are 0.0075 and 0.0019, respectively. The maximum axial strain, developed in the pipe with $D=0.4$ m and $D/t=100$ at the angle of incidence of 0° , is about 10 and 25% of the ultimate values of tensile and compressive strains, respectively. This shows a good margin of safety for the pipeline integrity.

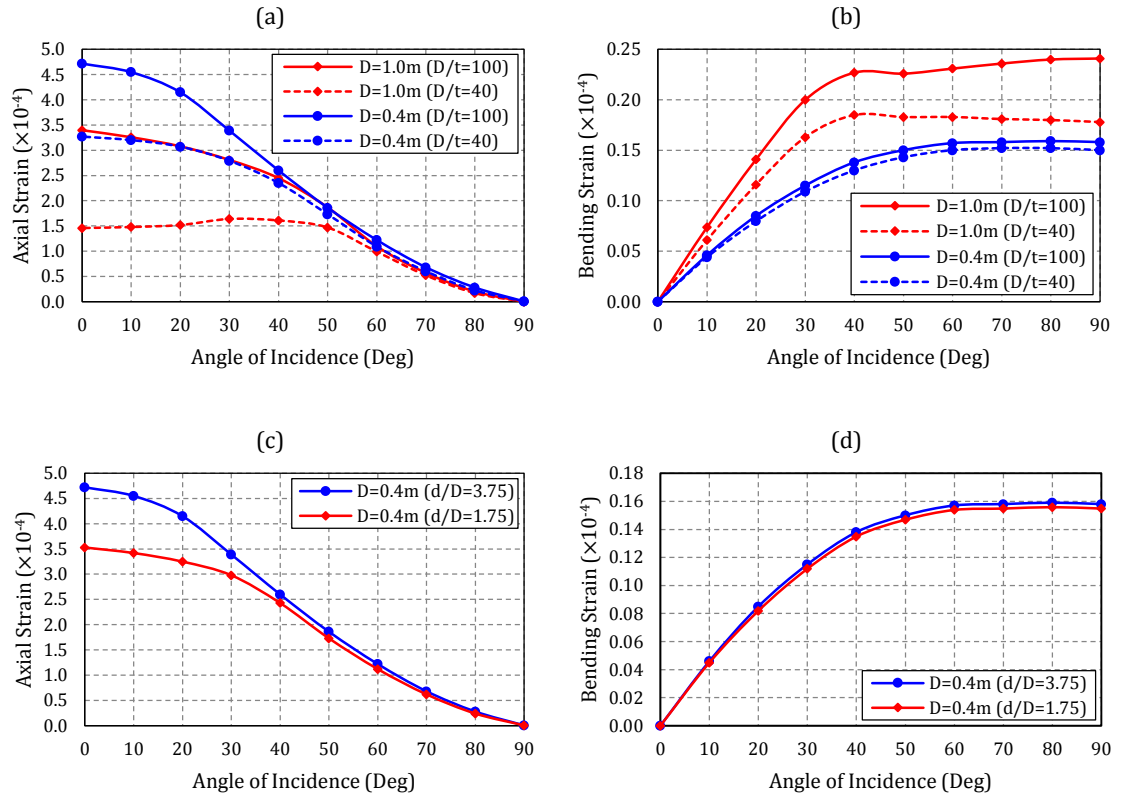


Figure 4-20: Effect of pipe diameter, D , and diameter to wall-thickness ratio, D/t , on (a) axial strains, and (b) bending strains, and effect of burial depth, d , on (c) axial strains, and (d) bending strains.

4.5.5 The worst case scenario

Based on the findings of this study, the highest level of strains would develop in a small-diameter pipe with large D/t and d/D under high intensity of bedrock excitations that result in R waves with low-frequency particle motion at ground surface level while having MSS condition. Therefore, a pipe with $D=0.4$ m, $D/t=100$ and $d/D=3.75$ is modelled under base excitation with $PGA_r=0.5g$. Variation of the resulted total strains (axial+bending) with respect to the angle of incidence is plotted in Figure 4-21. Comparing to the ultimate values for tensile and compressive strains, i.e., 0.0050 and 0.0019, respectively, the magnitude of peak strains are 32 and 58% of the ultimate values. The ovalization factor was still below 1%. For a corrosion-free straight pipeline this can still be a reliable margin of safety.

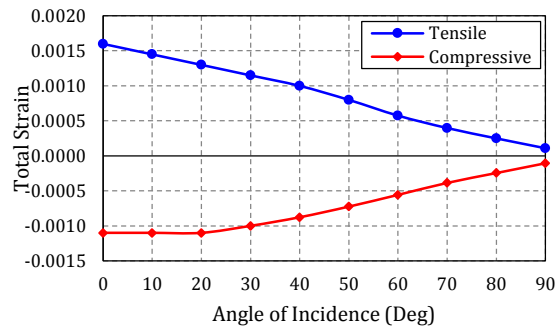


Figure 4-21: Variation of total strain (axial+bending) with the angle of incidence for the worst case scenario.

4.6 Summary and conclusions

Seismic behaviour of buried continuous pipelines that traverse discontinuous permafrost regions was studied. According to the experimental and numerical findings of Chapter 3 and using FLAC numerical modelling, a model was developed for prediction of the intermittent differential ground motions in discontinuous permafrost sites of northern Canada.

After formulation of the equation of motion considering soil-pipe interactions, response of buried pipelines was modelled by means of a finite element structural analysis program developed in Matlab. Different orientations of the pipeline with respect to wave angle of incidence were considered. Two major cases for the relative burial depth with respect to the permafrost table were investigated as well: identical support stiffness (ISS) and multiple support stiffness (MSS). The following conclusions can be made from the study on ISS and MSS cases:

- Under the ISS conditions the pipeline is subject to higher strains compared to the homogeneous ground conditions.
- Axial strains resulted from the R waves were shown to be dominant, whereas bending strains were realized to be secondary.

- Dense soils induce larger strains into the pipes during wave propagation events.
- Study of the MSS condition revealed that only bending strains are larger than those in the ISS. Though bending strains rose they were still smaller than the axial strains.
- Frequency content of the ground particles motion was found to be a significant parameter that has an inverse relationship with pipe strains.
- Pipe diameter, D , and diameter to wall-thickness ratio, D/t , were shown to be very important. It was concluded that the small-diameter pipes with large D/t have larger strain demands.
- Increase of the burial depth leads to development of larger axial strains in the pipe.
- Study of the worst case scenario showed that there is still a good factor of safety against tensile rupture, local buckling and premature cross-sectional failure.

Based on the findings of this research the followings are proposed for the future studies:

- Installing dense arrays of strong motion seismographs in discontinuous permafrost regions to validate the findings of the experimental and numerical models.
- Extending this study to the case of bending pipelines with different geometries.
- Evaluation of the effect of corrosion and other types of weakness on the strain demand.

References

Ariman, T., and G. E. Muleski. "A review of the response of buried pipelines under seismic excitations." *Earthquake Engineering and Structural Dynamics* 9 (1981): 133-151.

Atkinson, G. M., A. G. Davenport, and M. Novak. "Seismic risk to pipelines with application to northern Canada." *Canadian Journal of Civil Engineering* 9 (1982): 248-264.

Aylsworth, J. M., M. M. Burgess, D. T. Desrochers, A. Duk-Rodkin, T. Robertson, and J. A. Traynor. "Surficial geology, subsurface materials, and thaw sensitivity of sediments."

In *The physical environment of the Mackenzie Valley, Northwest Territories: a base line for the assessment of environmental change*. Edited by L. D. Dyke, & G. R. Brooks. Geological Survey of Canada, Bulletin 547, 2000. 41-48.

Blais-Stevens, A., R. Couture, A. Page, J. Koch, J. J. Clague, and P. S. Lipovsky. "Landslide susceptibility, hazard and risk assessments along pipeline corridors in Canada." *GEO2010*. Calgary, AB, 2010.

Bolt, B. A. *Earthquakes*. New York: W. H. Freeman, 1993.

CSA Z662-03 oil and gas pipeline systems. Mississauga, ON: Canadian Standards Association, 2003.

DeGeer, D., and M. Nessim. "Arctic pipeline design considerations." *Proceedings of the ASME 27th International Conference on Offshore Mechanics and Arctic Engineering*. Estoril, Portugal, 2008.

Drummond, K. J. *Mackenzie Valley quantitative hydrocarbon assessment*. Drummond Consulting, 2012.

Finn, W. D. L., and R. N. Yong. "Seismic response of frozen ground." *Journal of the Geotechnical Engineering Division (ASCE)* 104, no. 10 (1978): 1225-1241.

Finn, W. D. L., R. N. Yong, and K. W. Lee. "Liquefaction of thawed layers in frozen soils." *Journal of the Geotechnical Engineering Division (ASCE)* 104, no. GT10 (1978): 1243-1255.

FLAC, fast lagrangian analysis of continua, user's guide. Minneapolis, MN: Itasca Consulting Group, Inc., 2002.

Geo-engineering (M.S.T.) Ltd. *Ditchwall database for the Norman Wells to Zama oil pipeline. Volume I: ditchwall database documentation*. Geological Survey of Canada, 1992.

Guideline for the design of buried steel pipe. American Lifelines Alliance, 2001.

Guidelines for the seismic design of oil and gas pipeline systems. Committee on Gas and Liquid Fuel Lifelines, ASCE, 1984.

Haskell, N. A. "The dispersion of surface waves in multilayered media." *Bulletin of the Seismological Society of America* 43, no. 1 (1953): 17-34.

Hindy, A., and M. Novak. "Earthquake response of underground pipelines." *Earthquake Engineering and Structural Dynamics* 7 (1979): 451-476.

Hyndman, R. D., J. F. Cassidy, J. Adams, G. C. Rogers, and S. Mazzotti. "Earthquakes and seismic hazard in the Yukon-Beaufort Mackenzie." *CSEG Recorder*, 2005.

Idriss, I. M. "Response of soft soil sites during earthquakes." Edited by J. M. Duncan. *Proceedings of H. Bolton Seed Memorial Symposium.* Vancouver, BC: BiTech Publishers, 1990. 273-289.

Kay, A. E., A. M. Allison, W. J. Botha, and W. J. Scott. "Continuous geophysical investigation for mapping permafrost distribution, Mackenzie Valley, N.W.T., Canada." *Proceedings of the Fourth International Permafrost Conference.* Fairbanks: National Academy Press, 1983. 578-583.

Kotz, S., and S. Nadarajah. *Extreme value distributions: theory and applications.* London, UK: Imperial College Press, 2000.

Kramer, S. L. *Geotechnical earthquake engineering.* Upper Saddle River, NJ: Prentice Hall, 1996.

Kyriakides, S., and E. Corona. *Mechanics of offshore pipelines, Vol. I Buckling and collapse.* Oxford, UK: Elsevier, 2007.

Lawrence, D. E. *Survey of expert opinion on permafrost and geotechnical issues for northern pipelines.* Ottawa: Geological Survey of Canada, 2004.

Liang, J., and S. Sun. "Site effects on seismic behavior of pipelines: a review." *Journal of Pressure Vessel Technology* 122 (2000): 469-475.

Matlab and Statistics Toolbox Release 2011b. Natick, MA: The MathWorks, Inc, 2011.

Mavridis, G. A., and K. D. Pitilakis. "Axial and transverse seismic analysis of buried pipelines." *Eleventh World Conference on Earthquake Engineering*. Acapulco, Mexico, 1996.

Natural Resources Canada. 11 25, 2015. <http://www.nrcan.gc.ca/earth-sciences/science/permafrost-ice-snow/permafrost/10990> (accessed 3 4, 2016).

Newmark, N. M. "Problems in wave propagation in soil and rocks." *Proceedings of the International Symposium on Wave Propagation and Dynamic Properties of Earth Materials*. Albuquerque, USA: University of New Mexico Press, 1967. 7-26.

Nishio, N. "Damage ratio prediction for buried pipelines based on the deformability of pipelines and the nonuniformity of ground." *Journal of Pressure Vessel Technology* 116 (1994): 459-466.

Nixon, J. F., K. A. Sortland, and D. A. James. "Geotechnical aspects of northern gas pipeline design." *The Fifth Canadian Permafrost Conference*. Quebec City, 1990.

Nixon, J. F., R. Saunders, and J. Smith. "Permafrost and thermal interfaces from Norman Wells pipeline ditchwall logs." *Canadian Geotechnical Journal* 28 (1991): 738-745.

O'Rourke, M. J., and G. Ayala. "Seismic damage to pipeline: case study." *Journal of Transportation Engineering (ASCE)* 116, no. 2 (1990): 123-134.

O'Rourke, M. J., and X. Liu. *Response of buried pipelines subject to earthquake effects*. Buffalo, NY, USA: Multidisciplinary Center for Earthquake Engineering Research, 1999.

O'Rourke, M. J., G. Castro, and I. Hossain. "Horizontal soil strain due to seismic waves." *Journal of Geotechnical Engineering (ASCE)* 110, no. 9 (1984): 1173-1187.

O'Rourke, M. J., M. C. Bloom, and R. Dobry. "Apparent propagation velocity of body waves." *Earthquake Engineering and Structural Dynamics* 10 (1982): 283-294.

Oswell, J. M. "Pipelines in permafrost: geotechnical issues and lessons." *Canadian Geotechnical Journal* 48 (2011): 1412-1431.

PEER (Pacific Earthquake Engineering Research Center). http://peer.berkeley.edu/products/strong_ground_motion_db.html (accessed 3 1, 2016).

Ramberg, W., and W. R. Osgood. *Description of stress-strain curves by three parameters*. Washington DC: Technical Note No. 902, National Advisory Committee For Aeronautics, 1943.

Sakurai, A., and T. Takahashi. "Dynamic stresses of underground pipelines during earthquakes." *Proceedings of the 4th World Conference of Earthquake Engineering*. Santiago, Chile, 1969.

Savigny, W., A. Isherwood, and A. Baumgard. *Mackenzie gas project, review of strain-based design- loadings, Appendix B*. Vancouver, BC: BGC Engineering Inc, 2005.

Scandella, L., and R. Paolucci. "Earthquake induced ground strains in the presence of strong lateral soil heterogeneities." *Bulletin of Earthquake Engineering*, no. 8 (2010): 1527–1546.

Shaw, P. K., and S. Kyriakides. "Inelastic analysis of thin-walled tubes under cyclic bending." *International Journal of Solids and Structures* 21, no. 11 (1985): 1073-1100.

USGS Earthquake Science Center. U.S. Geological Survey. <http://escweb.wr.usgs.gov/> (accessed 1 1, 2016).

Wang, L., Z. Wu, J. Sun, X. Liu, and Z. Wang. "Characteristics of ground motion at permafrost sites along the Qinghai-Tibet railway." *Soil Dynamics and Earthquake Engineering* 29 (2009): 974-981.

Yang, Z., U. Dutta, G. Xu, K. Hazirbaba, and E. E. Marx. "Numerical analysis of permafrost effects on the seismic site response." *Soil Dynamics and Earthquake Engineering* 31 (2011): 282-290.

Yeh, G. C. K. "Seismic analysis of slender buried beams." *Bulletin Seismological Society of America* 64 (1974): 1551–1562.

Chapter 5

5 Quantifying exposure of buried pipelines to earthquake-triggered transverse landslides in permafrost thawing slopes⁴

5.1 Introduction

Southwestern Yukon, British Columbia, the Mackenzie and Richardson Mountains and beneath the Beaufort Sea are zones of high seismicity in Western Canada (Hyndman et al. 2005). In particular, the high seismicity along the Mackenzie Valley, Richardson Mountains and offshore beneath the Beaufort Sea represents a potential threat to the safety and integrity of the existing and projected energy pipelines in the region. Two seismic effects can develop critical stress and strain levels in pipelines and impact their integrity: the transient ground shaking that can further be altered by the local site effects with respect to the presence of permafrost and unconsolidated sediments (Hyndman et al. 2005); and the significantly more dangerous PGD due to earthquake induced landslides, slope instabilities and sediment liquefaction. For example, as a result of the M6.9 and M6.7 Nahanni earthquakes (1985), rock falls and rock avalanches occurred in the Mackenzie Mountains and liquefaction was observed at Little Doctor Lake, located 80 km away from the Mackenzie gas project right-of-way (Savigny et al. 2005).

The active-layer detachment (ALD) is probably the most common type of landslide observed in permafrost terrains (Aylsworth et al. 2000, Dyke 2004, and Lipovsky and Huscroft 2006). The active layer, located on top of the permafrost table, is the surficial soil layer that is subject to annual freeze-thaw cycles. Instability and downslope movement over the permafrost table surface is generally referred to as active-layer detachment. ALDs have been detected in the Mackenzie Valley and Fosheim Peninsula in Northwest Territories, in the Canadian Arctic Archipelago, and in Alaska (Lewkowicz 1990). The concept of ALD in the literature may refer to two different types of failure mechanisms (Lewkowicz 1990): flow (Hughes et al. 1973, McRoberts and Morgenstern 1974, and Aylsworth et al. 2000), and slide (Lewkowicz 1990, Harris and Lewkowicz

⁴ A version of this chapter has been submitted to the Canadian Geotechnical Journal.

1993 and 2000, and Lewkowicz and Harris 2005). Despite the different failure mechanisms and material transfer, McRoberts and Morgenstern (1974) and Lewkowicz and Harris (2005) have employed the concept of infinite slope stability analyses to characterize the ALD. Warm summer temperatures, intensive rainfalls and loss of vegetation cover due to forest fires or construction can trigger ALD. In low-permeability fine-grained soils, rapid ice melting can lead to excess pore water pressure build up within the active layer and cause instability in slopes even at small angles (McRoberts and Morgenstern 1974, and Morgenstern and Nixon 1971). As elsewhere, the seismic shaking also causes slope instability in otherwise relatively stable permafrost terrains, e.g., in the Mackenzie Valley following the Nahanni earthquakes (1985) (Savigny et al. 2005). It is therefore desirable to address the ALD hazard and develop a systematic risk assessment framework for existing and future pipelines.

5.2 Objectives and scope of work

The objective of this study is to analytically quantify the potential and the extent of transverse ALD landslides that poses threats to the integrity of extended infrastructures. This study will specifically focus on buried energy pipelines that are good examples of extended structures. The occurrence of ALDs along a specified pipeline route will be represented by a Poisson distribution. Then, probabilistic seismic slope stability analysis will be carried out by Monte Carlo simulation technique. The output will determine the portion of potential ALDs that impact the pipeline (probability of exposure) as well as the extent of PGD that the pipeline will be subjected to.

5.3 Pipeline exposure to transverse ALD hazard

Transverse ALDs represent a significant threat when their runout zone crosses the aboveground linear infrastructure axis. In case of underground infrastructure, however, the threat is more likely where the infrastructure is located within the detached layer. To assess the likelihood of a pipeline segment being exposed to PGD resulting from an earthquake-induced ALD, mechanisms of material transfer should be identified first. According to Mathewson and Mayer-Cole (1984) and Lewkowicz (1990), the ALD transfer mechanism integrates both the translational and compressional movement of a

block of active soil material (Figure 5-1). In cases where the resistance against the detachment of the block is not sufficient, the movement tends to be translational. Assuming that the geometry of the block remains constant, the PGD extent along the scar zone is uniform and equal to the scar length (L_S) at each point (Figure 5-1a). In this case, a pipeline buried in the active layer is exposed to the PGD if its axis is located within a maximum distance of $(L - L_S)$ from the scar crown, i.e., $S < (L - L_S)$. On the other hand, for cases where considerable resistance is exerted against the movement, the material is compressed and piled at the toe of the landslide and the block length is shortened. Assuming that the PGD extent vary linearly along the landslide length (L), as indicated in Figure 5-1b, a pipeline will be subject to PGD for $S < L$ and the PGD is inversely proportional to the distance (S) between the pipeline axis and the scar crown.

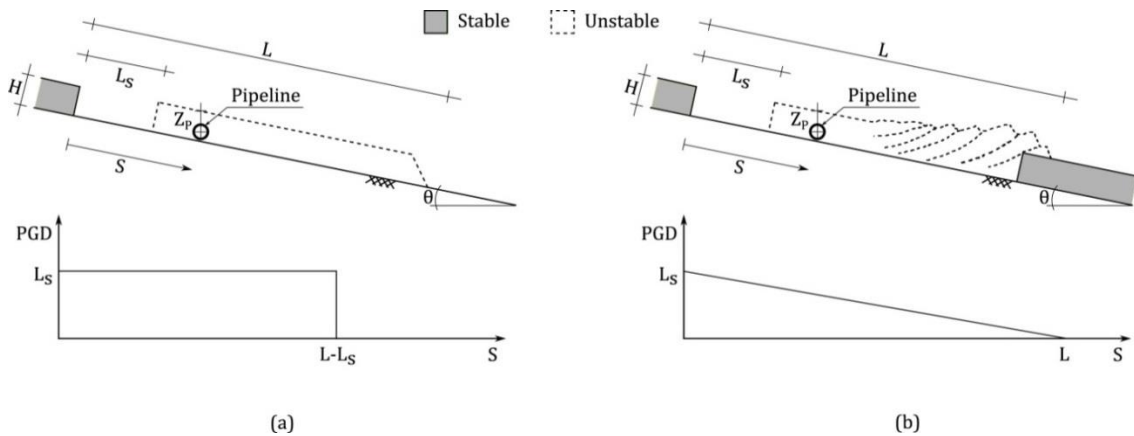


Figure 5-1: Mechanisms of material transfer and distribution of the transverse PGD for: (a) translational and (b) compressional movement. L represents the total landslide length, L_S is the scar zone length and S is the distance of scar crown to pipeline axis.

It is now important to determine the probability of pipeline exposure to PGD. The distance S from the pipeline axis to the scar crown is a site-specific parameter that depends on the surficial geology and soil mechanical properties, vegetation cover, slope angle, slope aspect, permafrost coverage and ice content (Blais-Stevens et al. 2010). Due to its flexibility in representing natural phenomena, the standard lognormal distribution is proposed herein as a theoretical distribution for S . For a detached layer with thickness (H)

large enough to impact the pipeline with burial depth of Z_p ($H \geq Z_p \cdot \cos \theta$), the index of exposure (I_E) can be defined as:

$$I_E = L - S \quad (5-1)$$

Accordingly, the pipeline will be impacted by transverse ALD only for positive I_E . Then, the probability of the exposure event outcome (E) defined for $I_E > 0$ is given by:

$$P(E) = P(I_E > 0) = 1 - P(I_E < 0) \quad (5-2)$$

As it can be seen in Figure 5-2, both L and S are required to determine the pipeline exposure to transverse PGD. The occurrence of transverse ALDs along a specified pipeline route can be expressed by a Poisson distribution with mean occurrence rate of v_{ALD} (Figure 5-2).

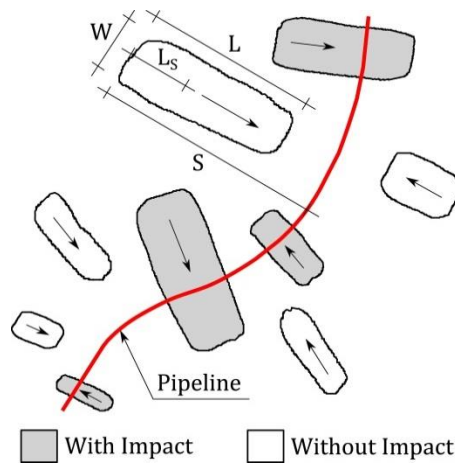


Figure 5-2: Top view of a hypothetical pipeline segment exposed to potential transverse active-layer detachments (ALD) and the relevant parameters: ALD width (W) and length (L), length of scar zone (Ls) and distance of scar crown to pipeline axis (S). ALDs that impact the pipeline are shown in grey.

5.4 ALD geometry

Based on the inventory of meteorologically-triggered ALDs at three different sites in the Fosheim Peninsula, a continuous permafrost region in the Canadian territory of Nunavut, Lewkowicz (1990) presented certain statistical aspects of typical ALD morphological

characteristics. The distribution of the ALD slide length (L) and width (W) at the three sites appear more or less similar and positively skewed and the depths of failure range between 0.2 and 0.65 m. Combining the results of this study with those of the Lewkowicz and Harris (2005) on ALDs in the discontinuous permafrost region of the central Mackenzie Valley, it was concluded that ALD may occur anywhere from the slope top to its bottom. The statistical averages for the morphology and morphometry of the ALD were quite similar for both studies. Two typical geometries were observed: compact and elongated. The compact ALD forms are characterised with length-to-width ratios less than 30 m and runout distances of only a few meters. The elongated forms, on the other side, may extend all the way from the top to the bottom of the slope with length-to-width ratios greater than 20 and runout distances attaining more than 500 m. The ALD widths in both regions were lognormally distributed, whereas the ALD lengths were lognormally distributed only in Fosheim Peninsula. At the Mackenzie Valley site, ALD lengths seem slightly better represented by the normal distribution. As an example, Table 5-1 shows the estimated lognormal distribution parameters based on the data presented in Lewkowicz (1990) for ALDs at “Hot Weather Creek” site on the Fosheim Peninsula.

Table 5-1: Statistical parameters of active-layer detachments at “Hot Weather Creek” site, Fosheim Peninsula, estimated based on Lewkowicz (1990).

ALD parameter	μ_{ln}	σ_{ln}	Median	Mean	Standard deviation
Width (m)	2.284	0.707	9.8	12.6	10.1
Length (m)	3.420	0.811	30.6	42.5	41.0
Length/Width	1.136	1.076	3.1	5.6	8.2
Area (m ²)	5.704	1.076	300.1	535.3	790.9

Note: μ_{ln} and σ_{ln} are the lognormal distribution parameters.

In parallel, investigating well-documented non-permafrost landslide events including about 25,000 cases occurred in USA, Italy and Guatemala with different triggering mechanisms, i.e., earthquake, rapid snow melt and heavy rainfall, Malamud et al. (2004) suggested a three-parameter inverse-gamma distribution to represent the frequency of occurrence of a given landslide area. The area distribution of ALDs at “Hot Weather Creek” and the one suggested by Malamud et al. are compared in Figure 5-3. The two distributions show major differences in case of smaller landslide areas and different mean and standard deviation.

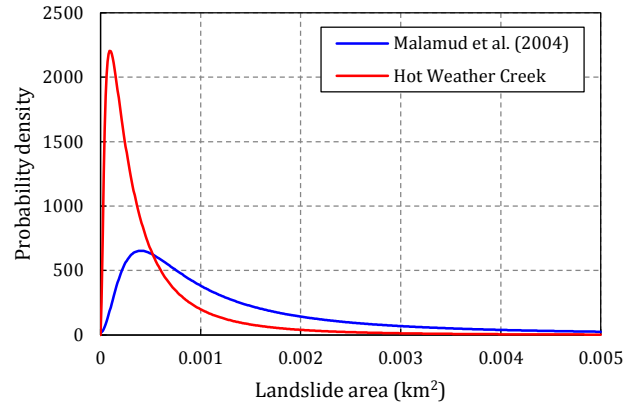


Figure 5-3: Landslide area distributions of active-layer detachments in permafrost region and some global landslides from Malamud et al. (2004).

Although “Hot Weather Creek” averages were derived using a relatively restrained number of ALDs (146 ALDs), when compared to those of Malamud et al., due to the peculiar triggering mechanism and shallow depths it is assumed that the mean and the standard deviation for the ALD area are statistically representative. As evidence, the medians of ALD width and length for the locations of “Black Top Creek”, “Hot Weather Creek” and “Big Slide Creek” reported by Lewkowicz (1990) are compared in Table 5-2 with those presented later by Lewkowicz and Harris (2005) based on the updated data base. As it can be seen, the increase of the number of the landslides contributes to only slight decrease of the medians of the width and length.

Table 5-2: ALD width and length medians at three locations on the Fosheim Peninsula: “Black Top Creek” (BTC), “Hot Weather Creek” (HWC) and “Big Slide Creek” (BSC).

	Width (m)			Length (m)			Number of ALDs		
	BTC	HWC	BSC	BTC	HWC	BSC	BTC	HWC	BSC
Pre-year 1989 median*	23	10	15	54	31	55	217	146	148
Pre-year 2000 median**	20	10	13	42	30	38	237	159	191

* Estimated from data of Lewkowicz (1990).

** Reported by Lewkowicz and Harris (2005).

Lewkowicz (1990) and Lewkowicz and Harris (2005) also reported statistical parameters for the ALD normalized scar length ($\bar{L}_S = L_S/L$) for the same three study areas in northern Canada. Based on the pre-year 1989 data, the normalized scar length (\bar{L}_S) varied between 5 to 80% and was correlated to particle size distribution of the active layer

material. It was concluded that ALD results in shorter scar zones in fine-grained soil when compared to sand-size material. The mean values of the normalized scar length for the fine-grained and sandy soils were 33 and 53%, respectively. Based on the pre-year 2000 updated data, medians of the normalized scar lengths are only slightly different: 50% for the sites covered by fine-grained soils (including a site in Mackenzie Valley) and 35% for the site with sandy soil.

Considering the lower and upper bounds as well as the means and medians of the normalized scar length, it appears that beta distribution appropriately represents the variations. For the random variable \bar{L}_S in the range between 0.05 and 0.80, the beta distribution can be given by (Ang and Tang 2007):

$$f_{\bar{L}_S} = \frac{1}{B(q,r)} \frac{(\bar{L}_S - 0.05)^{q-1} (0.80 - \bar{L}_S)^{r-1}}{0.75^{q+r-1}} \quad (5-3)$$

where, q and r are the parameters and B is the beta function. Assuming a symmetric distribution (skewness=0), q=r, the mean and the variance are:

$$\mu = 0.425, \sigma^2 = \frac{0.141}{2q+1} \quad (5-4)$$

A mean value of 0.425 falls well between the reported 0.33 and 0.53, and represents the overall average value for both fine-grained and sandy soils. Thus, the scar length can be calculated as:

$$L_S^{st} = \bar{L}_S \cdot L^{st} \quad (5-5)$$

where, L_S^{st} and L^{st} are the scar length and ALD length, respectively. The superscript “st” stands for ALDs driven by static forces. For earthquake-induced ALDs, the scar length (L_S) and the length (L) are calculated as a sum of the displacements caused by both static and dynamic forces:

$$L_S = L_S^{st} + L_S^{dy} \quad (5-6)$$

$$L = L^{st} + L^{dy} \quad (5-7)$$

where, L_S^{dy} is the scar displacement caused by dynamic forces only.

5.5 Assessment of ALD deformations

Standardised methods for determining scar length of earthquake-induced ALDs are discussed herein. Two different mechanisms govern earthquake triggered slope instability: weakening of the soil shear strength such that it cannot resist earthquake-induced stresses (weakening instability), and generation of inertial deformations that cause failure in the soil (inertial instability) (Kramer 1996). Depending on the type of the instability that takes place, i.e., weakening or inertial, a different approach for estimation of the PGD is applied. Weakening instabilities are investigated using models that account for the effect of excess pore water pressure on the shear strength of soil. On the other hand, inertial instabilities are usually simulated using the analogy of the behaviour of a soil mass with that of a block sliding on an inclined surface (Newmark 1965). In this study, flow failure and lateral spreading are considered as consequences of weakening instabilities.

5.5.1 Weakening instabilities

The geologic history of soil deposits may roughly determine whether they can be considered as susceptible to liquefaction. The surficial soils in the Mackenzie Valley include till, lacustrine, glaciofluvial, colluvial and alluvial fine-grained sediments (Aylsworth et al. 2000) deposited during the last continental Pleistocene glaciation (more than 10,000 years ago) (Monroe and Wicander 1992, and Duk-Rodkin and Lemmen 2000). When fully saturated, these unconsolidated sediments show low to moderate susceptibility to liquefaction (Youd and Perkins 1978).

In addition to the geologic criteria, the geotechnical properties should be considered as well in assessing the liquefaction potential. Boulanger and Idriss (2006) categorized fine-grained soils according to their plasticity index (PI) to soils that exhibit clay-like ($PI \geq 7$) and sand-like ($PI < 7$) behaviour. The former group is essentially not liquefiable, whereas the latter can be liquefied. Limited information, however, was found in the literature: the Atterberg limits of samples collected from the proximity of thaw

front in some ALDs of the Fosheim Peninsula and Mackenzie Valley reveal low to medium plasticity with PI in the range between 5 and 30 (Lewkowitz and Harris 2005); Wang et al. (2005) reported silty clay and clayey silts as the most common soil type within a 20 km-wide corridor east of the Mackenzie River. Although this dataset is not representative for the whole region, it provides an insight in the general soil properties for the liquefaction study. During the 2002 M7.9 Denali earthquake, Alaska, extensive liquefaction was observed in fine-grained soils of Mabel Creek area with average PI of 5.3 and standard penetration test (SPT) values of 4 to 12 (Zhang 2009). According to this limited information, it can be concluded that in northern regions unfrozen low-plasticity clayey silts with $5 \leq PI \leq 7$ can show liquefaction potential. Therefore, study of the likelihood of “weakening instability” is incorporated in this study.

After checking geologic and compositional criteria for liquefaction susceptibility, to represent the triggering conditions, a factor of safety against weakening instability (FS_w) is defined as:

$$FS_w = \frac{CRR}{CSR} \quad (5-8)$$

where, CRR is the cyclic resistance ratio that characterizes the soil resistance against liquefaction and CSR is the cyclic stress ratio. Several assumptions are made to solve Equation (5-8):

- CRR is obtained using SPT results (Seed et al. 1985) that are normalized to overburden pressure of 1 ton/ft² and hammer efficiency of 60%, presented as $(N_1)_{60}$. In this study, based on Seed et al. (1985) and the recommendations of the NCEER workshop (1996) (Youd et al. 2001), the following simplified relationship between CRR and normalized SPT values of clean sand, $(N_1)_{60CS}$, for M7.5 earthquakes is developed:

$$CRR_{M7.5} = \begin{cases} 0.05 & (N_1)_{60CS} \leq 5 \\ 0.0117(N_1)_{60CS} - 0.0083 & (N_1)_{60CS} > 5 \end{cases} \quad (5-9)$$

This relationship, shown in Figure 5-4, is for clean sands rather than those with fines content.

- The effect of fines content on the $(N_1)_{60}$, studied by Idriss and R. B. Seed, is considered applying the following corrective equation (Youd et al. 2001):

$$(N_1)_{60cs} = \alpha + \beta(N_1)_{60} \quad (5-10)$$

where, α and β are functions of fines content (Table 5-3).

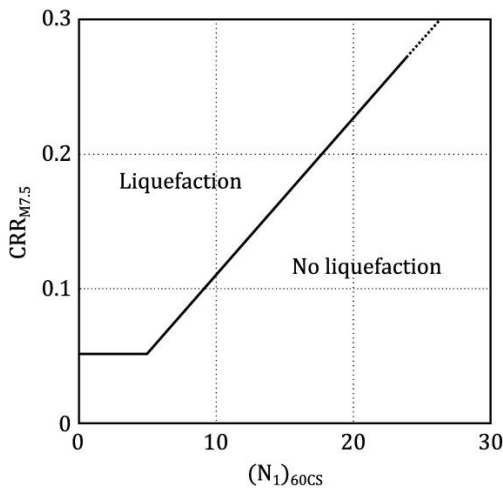


Figure 5-4: Simplified relationship of the cyclic resistance ratio (CRR) in M7.5 earthquakes and SPT results, developed for this study based on Seed et al. (1985) and recommendation of NCEER workshop (1996) published by Youd et al. (2001).

- The effects of earthquake magnitude other than M7.5, soil plasticity and terrain slope on the final resistance against liquefaction are accounted for using corresponding correction factors (Youd et al. 2001):

$$CRR = C_m \cdot C_p \cdot C_s \cdot CRR_{M7.5} \quad (5-11)$$

where, C_m , C_p and C_s are the correction factors for earthquake magnitude, soil plasticity and terrain slope, respectively (Table 5-3).

- CSR, which actually represents the equivalent harmonic shear stress to the liquefaction triggering earthquake-induced cyclic stresses, was presented by Seed and Idriss (1971) as:

$$CSR = 0.65 \left(\frac{\sigma_v}{\sigma'_v} \right) PGA \cdot r_d \quad (5-12)$$

where, PGA is the peak ground acceleration (fraction of g), r_d is the reduction factor for depth (Table 5-3), σ_v and σ'_v are the total and effective vertical stresses at the depth where liquefaction is being studied.

Table 5-3: Correction factors used in the estimation of factor of safety against liquefaction in this study.

Correction factor	Formula	Range of parameters	Reference
Fines content (α)	0	$FC \leq 5\%$	Youd et al. (2001)
	$\exp[1.76 - (190/FC^2)]$	$5\% < FC < 35\%$	
Fines content (β)	5	$FC \geq 35\%$	Youd et al. (2001)
	1	$FC \leq 5\%$	
Depth (r_d)	$0.99 + (FC^{1.5}/1,000)$	$5\% < FC < 35\%$	Liao and Whitman (1986)
	1.2	$FC \geq 35\%$	
Magnitude (C_m)	$1 - 0.00765z$	$z < 9.15 \text{ m}$	Youd et al. (2001)
Plasticity (C_p)	$10^{2.24}/M^{2.56}$	$5^{1/2} \leq M \leq 8^{1/2}$	Ishihara (1993)
	1	$PI \leq 10$	
Slope (C_s)	$1 + 0.022(PI - 10)$	$PI > 10$	Developed based on Kavazanjian Jr et al. (1997)
	$-x + 1$	$D_r \approx 35\%$	
	1	$D_r \approx 40\%$	
	$1.9x + 1$	$D_r \approx 45 - 50\%$	
	$2.9x + 1$	$D_r \approx 55 - 70\%$	

Note: FC and PI stand for fines content and plasticity index, respectively, and $x = \tau_h/\sigma'_v$.

Both flow failure and lateral spreading are weakening instabilities that may result from liquefaction. When $FS_w < 1$, Equations (5-6) and (5-7) apply to compute the scar length (L_S) and the total length (L) in both cases. However, which mechanism will be triggered depends mainly on the sloping angle:

- For small sloping angle of $\theta < 6^\circ$, the lateral spreading represents the governing failure mechanism. The corresponding maximum displacement can be estimated with the empirical expression proposed by Youd et al. (2002) and developed for gently sloping terrains (without free-face):

$$\log(D_H) = -16.213 + 1.532M - 1.406 \log(R + 10^{0.89M-5.64}) - 0.012R + 0.338 \log(S) + 0.540 \log(T_{15}) + 3.413 \log(100 - F_{15}) - 0.795 \log(D50_{15} + 0.1) \quad (5-13)$$

where, M is the earthquake moment magnitude, R is the earthquake source-to-site distance (km), S is the ground slope (%), T_{15} is the total layer thickness (m), F_{15} is the average fines content (%), and $D50_{15}$ is the average mean grain size of the granular soil layer with $(N_1)_{60} < 15$ in millimeters. A standard deviation equal to 0.197 for $\log(D_H)$ is reported by Gillins and Bartlett (2013). For lateral spreading $L_S^{dy} = 0$, $L_S^{st} = D_H$, and L^{st} is calculated from the lognormal distribution with parameters given in Table 5-1.

- For higher sloping angles, $\theta > 6^\circ$, the flow failure mechanism is triggered. In this case, L_S^{st} is calculated from Equation (5-5), L^{st} is found in a similar way to the lateral spreading case and $L_S^{dy} = 0$.

5.5.2 Inertial instabilities

The inertial earthquake-induced slope deformations can be separated into three different types of deformations (Ambraseys and Srbulov 1995): (i) co-seismic deformations, which occur during the ground shaking as a function of the earthquake magnitude and duration, geometry of slope and undrained mobilized strength at the slip surface; (ii) post-seismic deformations triggered immediately after the end of the ground shaking, provided that the factor of safety against inertial instability (FS_I) at the end of the co-seismic stage is smaller than 1. Here, only gravity drives the block, whereas the mobilized undrained residual strength of the slip surface resists against the motion and this continues until $FS_I > 1$; and (iii) indirect deformations caused by phenomena such as creep, consolidation processes and redistribution of pore pressures as the developed ground cracks are filling in with water. They may occur immediately or slightly after the first or the second types of deformations.

The co-seismic deformations can be estimated using the Newmark's sliding block approach assuming rigid body behaviour. During the ground shaking, acceleration may

exceed critical levels for the potential slip surface and the block will experience permanent deformation. It is obtained by summing up the double integrals of the acceleration time history over the duration of the exceedance time, also referred to as the Newmark displacement. Several regression models have been proposed in the literature to facilitate the computation. These models correlate Newmark displacement (D_N) to critical acceleration of the slope (a_c) and to ground motion parameters, such as the PGA, Arias intensity and moment magnitude. As an example, Jibson (2007) derived the following equation based on 875 Newmark displacements resulted from some worldwide strong motions:

$$\log(D_N) = 2.401 \log(I_a) - 3.481 \log(a_c) - 3.230 \pm \sigma \quad (5-14)$$

where, D_N is in cm, I_a is the Arias intensity in m/sec, a_c is in terms of g and $\sigma = \pm 0.656$ represents the standard deviation of the model. Equation (5-14) allows for site-consistent Arias intensity attenuation models, such as those developed by Wilson and Keefer (1985) and Travararou et al. (2003), to correlate I_a and D_N to the earthquake magnitude and the source-to-site distance. In this study, equation developed by Wilson and Keefer that has fewer input parameters is used:

$$\log(I_a) = M - 2 \log(R) - 4.1 \quad (5-15)$$

where, I_a is in m/sec.

Based on the equation of Ambraseys and Menu (1988), Jibson (2007) also presented another expression for D_N that is applicable to $5.3 \leq M \leq 7.6$:

$$\log(D_N) = -2.710 + \log \left[\left(1 - \frac{a_c}{PGA} \right)^{2.335} \left(\frac{a_c}{PGA} \right)^{-1.478} \right] + 0.424M \pm \sigma \quad (5-16)$$

where, $\sigma = \pm 0.454$.

From Figure 5-5, the critical acceleration of the planar slip surface (a_c) in terms of g can be calculated as:

$$a_c = (FS_I - 1)g \sin \theta \quad (5-17)$$

where, θ is the inclination angle. Using the limit equilibrium conditions, FS_I for infinite shallow slope is then defined by:

$$FS_I = \frac{c' + \{H[(1-m)\gamma + m\gamma_{sat}] \cos \theta - u\} \tan \phi'}{H[(1-m)\gamma + m\gamma_{sat}] \sin \theta} \quad (5-18)$$

where, γ and γ_{sat} are the bulk and saturated unit weights of soil, c' is the effective cohesion, ϕ' is the effective friction angle, H is the thickness of thawed active layer, u is the pore water pressure, and m indicates the saturated portion of the active layer's depth measured from the interface of the active layer with the permafrost table (the potential slip surface). The parameters c' , ϕ' and u should be measured at the location of the potential slip surface.

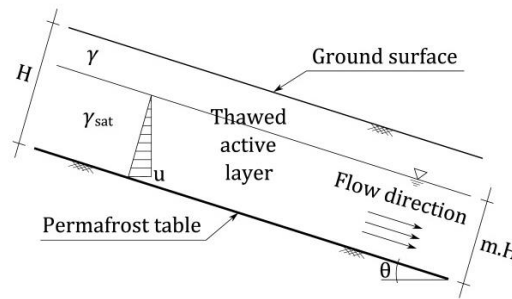


Figure 5-5: Infinite thawed slope in cold region with related parameters.

The Newmark displacement can be used as susceptibility index for prediction of landslide likelihood after calibration against observed landslides (Jibson 2011). Jibson et al. (2000) compared the Newmark displacements from the 1994, M6.7 Northridge earthquake with the triggered landslides, and presented the probability of slope instability. The fitted Weibull distribution shows that the probabilities of failure are 0.45, 0.83 and 0.96 for Newmark displacements less than 5, 10 and 15 cm, respectively. It can therefore be concluded that the majority of the landslides occur when the Newmark displacement is less than 15 cm and this value can be considered as a threshold Newmark displacement. Other threshold displacements proposed in the literature are given in Table 5-4.

Table 5-4: Newmark displacement threshold values (Jibson 2011).

Reference	Threshold D_N (cm)	Target location	Remarks
Wieczorek et al. (1985)	5	San Mateo County, California	
Keefer and Wilson (1989)	10	Southern California	For coherent landslides.
Jibson and Keefer (1993)	5 to 10	Mississippi Valley	
Jibson et al. (2000)	2 to 15	Northern San Fernando Valley and Santa Susana Mountains	For shallow, disrupted rock falls and rock slides in fairly brittle, weakly cemented sediments.
Blake et al. (2002)	5 or 15	Southern California	Depends on slope conditions and soil properties.
California Geological Survey (2008)	0 to 15		Unlikely to be damaging.
	15 to 100	California	Enough serious to be damaging.
	Greater than 100		Very likely to be damaging.
	0 to 1		Low hazard level (shallow landslide).
Jibson and Michael (2009)	1 to 5	Anchorage, Alaska	Moderate hazard level (shallow landslide).
	5 to 15		High hazard level (shallow landslide).
	Greater than 15		Very high hazard level (shallow landslide).

The post-seismic deformations are larger compared to the co-seismic deformations and their magnitude depends on the local site conditions such as slope inclination angle and undrained residual shear strength at the slip surface. Separation of the co-seismic from the post-seismic deformations in the field is often difficult and so is the validation of analytical models against the observed field deformations. Since the post-seismic movements have similar kinematic conditions to the deformations of non-seismically triggered ALDs, the available records of fire- and meteorological-triggered ALDs presented in Section 5.4 may be used as a substitute. Thus, in the case of inertial instabilities, $L_S^{dy} = D_N$ and L_S^{st} is obtained from the lognormal distribution with parameters given in Table 5-1. When D_N is smaller than the threshold $L_S^{st} = 0$ and when D_N is larger than the threshold, L_S^{st} is not zero and should be calculated from Equation (5-5). Equations (5-6) and (5-7) should be used to find the total scar length (L_S) and the total ALD length (L).

Since the soil shear strength during and after the earthquake is the key parameter in determining the type of instability, the occurrence of “weakening” mode is verified first. If the active layer was not susceptible to liquefaction, the “inertial” mode is investigated then. According to this logic, the flowchart shown in Figure 5-6 summarizes the successive steps for estimating the earthquake-induced ALD deformations (scar length).

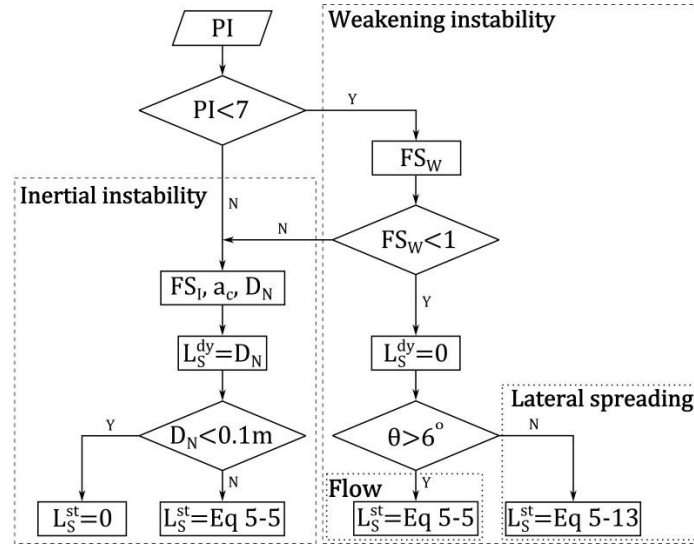


Figure 5-6: Flowchart showing the procedure of earthquake-induced ALD scar length calculations.

5.5.3 Effect of pore water pressure

Two thaw conditions can be considered in this model to calculate the pore water pressure: slow and rapid. Under the slow thawing condition, no pore pressure is assumed to be produced in excess of the hydrostatic pressure. The pore water pressure u in Equation (5-18) is then simply computed for the saturated portion of the active layer:

$$u = mH\gamma_w \cos \theta \quad (5-19)$$

Under the rapid thawing condition, on the other hand, excess pore pressure is generated as a result of “thaw-consolidation”. The thaw-consolidation is a phenomenon exclusive to fine-grained ice-rich soils in cold regions when thawing rate of the active layer is faster than drainage and consolidation rates. It can cause slope instabilities for angles smaller than those predicted by the classic slope stability theories. The rapid thawing usually occurs as a result of forest fire- or construction-caused loss of surface vegetation and heavy rainstorms (Dyke 2004, and Lewkowicz and Harris 2005). Morgenstern and Nixon (1971) developed a thaw-consolidation model combining Terzaghi’s linear consolidation theory and Neumann’s one-dimensional melting solution with the resulting excess pore water pressure given as:

$$\Delta u = \frac{mH(\gamma_{\text{sat}} - \gamma_w) \cos \theta}{1 + \frac{1}{2R_{\text{tc}}^2}} \quad (5-20)$$

where, γ_w is the unit weight of water and R_{tc} is the thaw-consolidation ratio between the input and output water in the thawing ground system defined by:

$$R_{\text{tc}} = \frac{\alpha_h}{2\sqrt{c_v}} \quad (5-21)$$

where, α_h is a heat conductivity-related constant and c_v is the coefficient of consolidation of the thawing soil. Substituting Equation (5-21) into Equation (5-20), the total pore water pressure applied in Equation (5-18) under the rapid thawing condition is obtained as:

$$u = mH \left[\gamma_w + \left(\frac{2R_{\text{tc}}^2}{2R_{\text{tc}}^2 + 1} \right) (\gamma_{\text{sat}} - \gamma_w) \right] \cos \theta \quad (5-22)$$

More details about the thaw-consolidation model of Morgenstern and Nixon and its related parameters are given in Morgenstern and Nixon (1971). According to McRoberts (1975), α_h is likely to fall in the range of 0.1 to 1.0 mm/sec^{0.5}. For the Norman Wells pipeline project, the respective c_v values of 0.0025 and 0.01 cm²/sec for ice-rich clay and till have been used (Hanna and McRoberts 1988). Paudel and Wang (2010) obtained c_v in the range between 0.01 and 0.06 cm²/sec after a number of freeze-thaw cycles in fine-grained soil samples from the Mackenzie Valley.

5.5.4 Ground motion parameters

The seismic ground motion parameters are necessary for evaluating CRR (Equation 5-11) and CSR (Equation 5-12). The ground motion parameters are typically defined employing an attenuation relationship often referred to as ground motion prediction equation (GMPE) consistent with the location of the study area. Consequently, the source-to-site distance, R , in the attenuation relationship should be consistent with those that are used in this study, i.e. in Equations (5-13) and (5-15). In this study, R is defined as the closest horizontal distance of the site to the vertical projection of the fault rupture plane. The GMPE applicable to the Western North America (WNA) developed by Boore et al. (1997) is adopted in this study. This relationship considers different local site conditions

defined with the average shear wave velocity of the top-30 meter (V_{S30}) and has a standard deviation equal to 0.468 for $\ln(\text{PGA})$. It is assumed herein that $V_{S30}=620$ m/sec, which represents average soil condition within soil class C, dense soil to soft rock ($V_{S30}=360-760$ m/sec) (National Building Code of Canada 2010). Plots of PGA attenuation with distance corresponding to different values of M are shown in Figure 5-7.

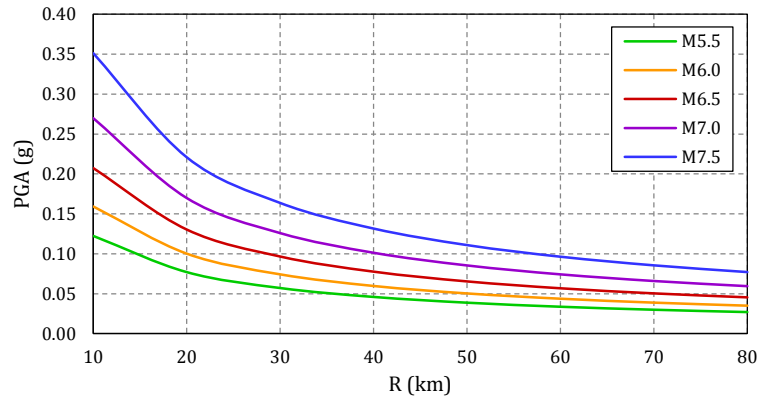


Figure 5-7: Boore et al. (1997) PGA attenuation used in this study. R is the closest horizontal distance of the site to the vertical projection of the fault rupture plane. $\ln(\text{PGA})$ has a standard deviation of 0.468 and median values of PGA are plotted here.

5.6 Probability of exposure and Monte Carlo simulations

To determine the probability of exposure, i.e., the probability that a pipeline is exposed to a landslide as defined with Equation (5-2), and predict the extent of the PGD, a Monte Carlo simulation was performed using Matlab (The MathWorks, Inc. 2011). Table 5-5 summarizes the input variables along with the corresponding distributions and their statistical parameters. The mean values and coefficients of variation (COV) were assumed based on the values reported in the literature and the guidelines of Phoon and Kulhawy (1999).

Table 5-5: Input variables for Monte Carlo simulations.

Variable	Probabilistic			Deterministic	Remarks	
	Mean	COV (%)	Distribution			
Slope:	θ (Deg)	20	50	Lognormal	-	-
	H (m)	1.0	30	Lognormal	-	-
	m	0.75	5	Beta	-	$0.5 \leq m \leq 1.0$
Soil:	S (m)	50, 80, 110	50	Lognormal	-	-
	γ_d (kN/m ³)	16	9*	Lognormal	-	-
	c' (kPa)	2.5	20*	Lognormal	-	Cross-correlated to ϕ'
	ϕ' (Deg)	26	10*	Lognormal	-	Cross-correlated to c'
	$(N_1)_{60}$	5	45*	Lognormal	-	-
	FC (%)	-	-	-	70	-
	PI (%)	15	40	Beta	-	$5 \leq PI \leq 30$
	T_{15} (m)	1.0	30	Lognormal	-	$T_{15} = H$
	F_{15} (%)	-	-	-	70	$F_{15} = FC$
	$D50_{15}$ (mm)	0.01	60	Lognormal	-	-
	D_r (%)	-	-	-	40	-
	R_{tc}	-	-	-	0.0, 1.5, 3.0	-
	Ground motion:	M	-	-	-	5.5, 6.5, 7.5
R (km)		-	-	-	10, 40, 80	-

*Based on the guidelines of Phoon and Kulhawy (1999).

Cross-correlation coefficients among the soil properties are site-dependent and are rarely reported in the literature. For this study, only the variables ϕ' and c' were treated as dependent variables, whereas the other input parameters were assumed as independent. Uzielli et al. (2007) proposed a correlation coefficient between effective friction angle and effective cohesion in the range of -0.75 to -0.25, which can be used for practical applications in the absence of site-specific information.

The Venn diagram of the sample slopes generated by Monte Carlo technique is shown in Figure 5-8. As it can be seen, part of the samples with negative index of exposure (I_E^-) belong to stable slopes, whereas the other part that belongs to unstable slopes include those landslides with runout zones that do not cross the pipeline axis. Using the Venn diagram and concentrating on exposure events with $E=I_E^+$ (Section 5.3), the probabilities of weakening and inertial instabilities can be defined as $P(WI|E)$ and $P(II|E)$, respectively.

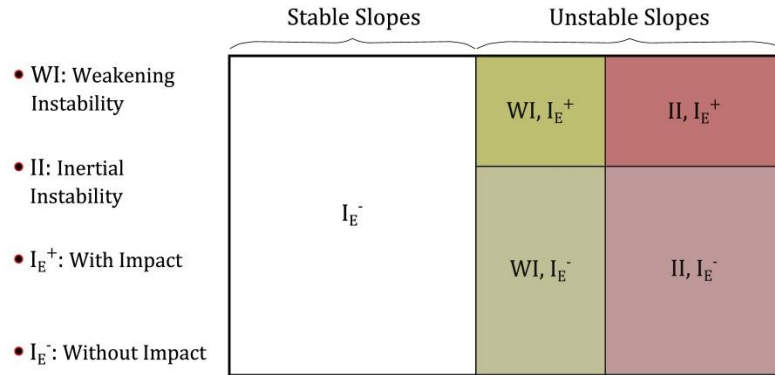


Figure 5-8: Venn diagram of the slope samples generated by Monte Carlo technique.

Effect of four parameters: distance of the pipeline axis to the scar crown, thaw-consolidation ratio, earthquake magnitude and source-to-site distance, on the index of exposure, I_E , are investigated by Monte Carlo simulations. They are shown in the form of cumulative distribution function (CDF) of I_E in Figure 5-9, and PGD in Figure 5-10. In each figure, the considered parameter was assigned three different values (low, moderate and high) while the other parameters remained constant and equal to the moderate value (except for R_{tc} that was kept in its low level, i.e., the slow thawing condition). According to Equation (5-2) and considering Figure 5-8, the probabilities of exposure, $P(E)$, can be calculated as $1 - \text{CDF}(I_E=0)$. These probabilities are shown in Table 5-6.

As it can be seen in Figure 5-9a, I_E is sensitive to the distance of the pipeline axis to the scar crown; however the probability of exposure is not. Also, according to Figure 5-9b, the probability of exposure is very sensitive to the thaw-consolidation ratio in this model. The variation of I_E with the earthquake magnitude indicates that I_E remains almost unchanged with increase of magnitude from M5.5 to M6.5, but it rapidly increases beyond M6.5 (Figure 5-9c). As shown in Figure 5-9d, probability of exposure attenuates rapidly with the increase of source-to-site distance.

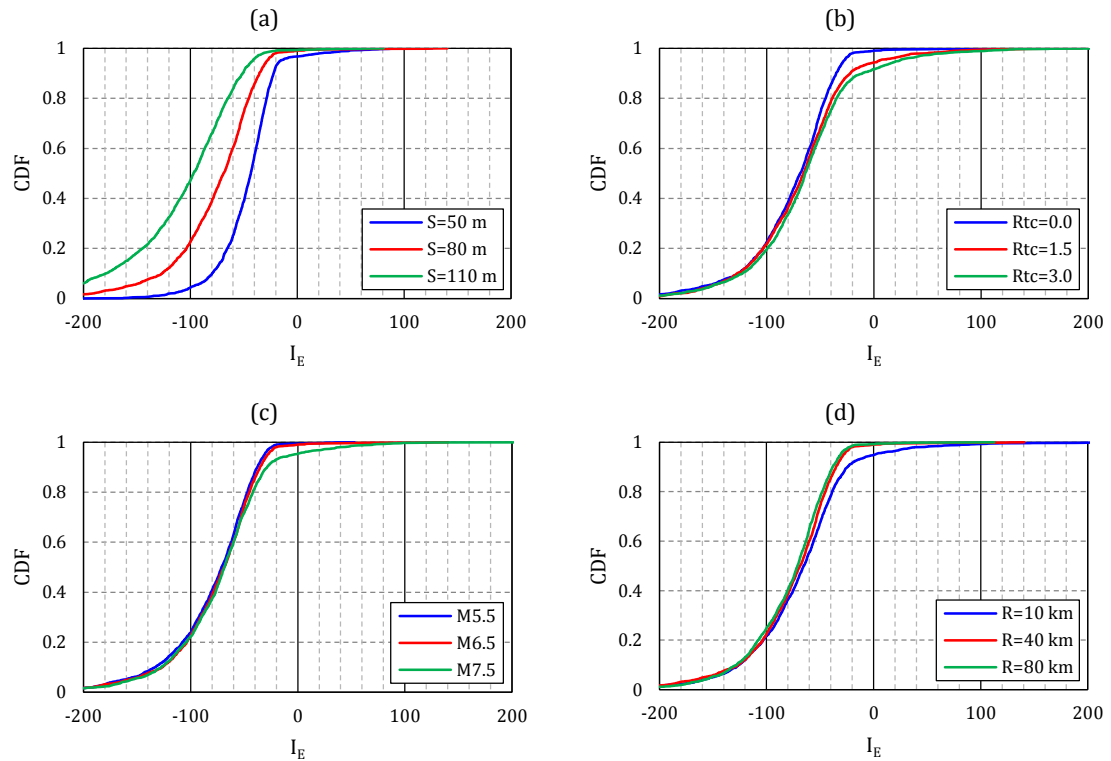


Figure 5-9: Variation of the cumulative distribution function (CDF) of the index of exposure (I_E) with (a) distance of the pipeline axis to the scar crown S , (b) thaw-consolidation ratio R_{tc} , (c) earthquake magnitude M , and (d) source-to-site distance R .

The results of the PGD analyses show negligible sensitivity with variations of S (Figure 5-10a). On the other hand, an increase of R_{tc} increases not only the probability of exposure (Figure 5-9b) but also the PGD extent (Figure 5-10b). PGD shows high sensitivity to changes of the earthquake magnitude and source-to-site distance. However, the PGD shows similar relationship to the probability of exposure for the considered parameters. According to Table 5-6, I_E is the most sensitive to R_{tc} , M and R and the resulting PGD mean and COV have, respectively, proportional and inversely proportional relationships with $P(E)$. In all cases, the Weibull distribution shows excellent fit with the results data.

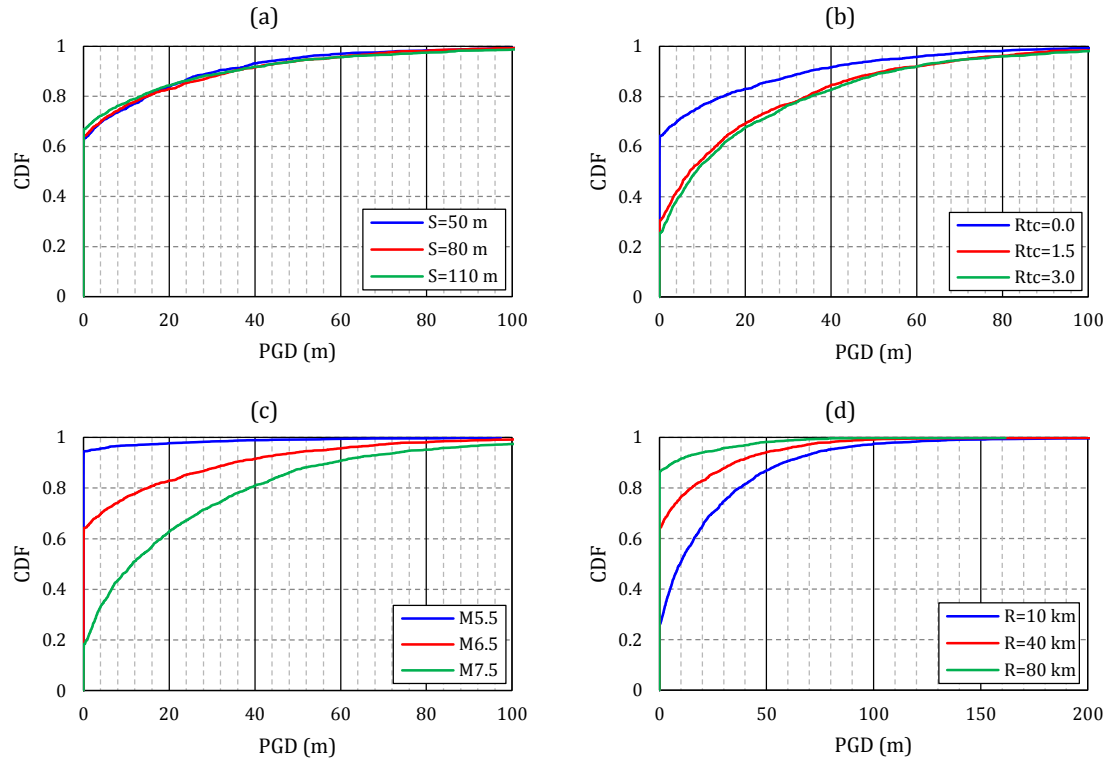


Figure 5-10: Variation of the cumulative distribution function (CDF) of the PGD with (a) distance of the pipeline axis to the scar crown, (b) thaw-consolidation ratio, (c) earthquake magnitude and (d) source-to-site distance.

The probability of exposure for combination of the considered weakening and inertial instabilities (Figure 5-8) and the mean and COV of PGD for the studied cases are presented in Table 5-6. Due to the considered soil PI distribution, one may expect that the majority of the pipeline exposure events result from inertial instabilities rather than soil weakening instabilities. The exception are cases with thaw-consolidation conditions ($R_{tc}>0$) and/or subject to stronger ground motions (M7.5 and R=10 km).

Table 5-6: Probabilities of exposure, weakening instability and inertial instability obtained from Monte Carlo simulations.

	S (m)			R_{tc}			M			R (km)		
	50	80	110	0	1.5	3	5.5	6.5	7.5	10	40	80
P(E)	0.028	0.015	0.008	0.015	0.050	0.070	0.007	0.015	0.043	0.056	0.015	0.007
P(WI E)	0.242	0.235	0.219	0.235	0.630	0.700	0.002	0.235	0.662	0.557	0.235	0.030
P(II E)	0.758	0.766	0.782	0.766	0.370	0.300	0.999	0.766	0.339	0.444	0.766	0.970
PGD Mean (m)	9.30	9.85	9.85	9.85	18.46	19.83	1.28	9.85	22.55	21.51	9.85	3.33
PGD COV (%)	246	236	245	236	147	145	608	236	142	157	236	375

Note: E, WI and II are the events of exposure, weakening instability and inertial instability, respectively.

5.7 Summary and conclusions

The probability that a buried pipeline is exposed to the peak ground deformation (PGD) of earthquake-triggered active-layer detachment (ALD) in permafrost regions was investigated. Two mechanisms were assumed for material transfer: translation and compression. The extent of the PGD along ALD runout zone was determined next. The probability of exposure was determined applying Monte Carlo simulation combined with statistical distribution representing the distance between the scar crown of the ALD and the axis of pipeline and the computed length of the earthquake-triggered ALD. An algorithm was developed considering soil weakening and inertial instabilities triggered by earthquakes. The effects of the distance of the pipeline axis to the scar crown, thaw-consolidation ratio, earthquake magnitude and source-to-site distance on the probability of exposure were studied. The results show that the distance of scar crown to the pipeline axis has a major influence on the exposure. The effect of thaw-consolidation phenomenon was investigated and it was shown that the existence of increased pore water pressure prior to an earthquake can increase the probability of exposure and of the weakening instabilities; large magnitude earthquakes and short source-to-site distances have similar effects on the weakening instabilities. It was assumed that the earthquake-induced PGDs to pipeline follow the Weibull distribution. The scale and shape factors of the distribution were determined and it was observed that they have large coefficient of variations. The accuracy of the results obviously depends on the quality of input parameters and the assumptions made in the study.

To decrease uncertainties, future research topics should include the following:

- Study of the material transfer mechanisms in ALD and determine the conditions under which each of the mechanisms occurs.
- Monitor the behaviour of the potential unstable slopes in the permafrost region and perform post-seismic investigations.
- Determine distribution of the potential ALD locations along pipeline routes.

- Improve the accuracy of the input parameters of the soil and slope by performing detailed geotechnical and geological site investigations.

References

Ambraseys, N. N., and M. Srbulov. "Earthquake induced displacement of slopes." *Soil Dynamics and Earthquake Engineering* 14 (1995): 59-71.

Ang, A. H. S., and W. H. Tang. *Probability concepts in engineering, emphasis on applications in civil & environmental engineering*. John Wiley & Sons, Inc., 2007.

Aylsworth, J. M., A. Duk-Rodkin, T. Robertson, and J. A. Traynor. "Landslides of the Mackenzie Valley and adjacent mountainous and coastal regions." In *The physical environment of the Mackenzie Valley, Northwest Territories: a base line for the assessment of environmental change*. Edited by L. D. Dyke, & G. R. Brooks. Geological Survey of Canada, Bulletin 547, 2000. 167-176.

Blais-Stevens, A., R. Couture, A. Page, J. Koch, J. J. Clague, and P. S. Lipovsky. "Landslide susceptibility, hazard and risk assessments along pipeline corridors in Canada." *GEO2010*. Calgary, Alberta, 2010.

Boore, D. M., W. B. Joyner, and T. E. Fumal. "Equations for estimating horizontal response spectra and peak acceleration from western North American earthquakes: a summary of recent work." *Seismological Research Letters* 68, no. 1 (1997): 128-153.

Boulanger, R. W., and I. M. Idriss. "Liquefaction susceptibility criteria for silts and clays." *Journal of Geotechnical and Geoenvironmental Engineering (ASCE)* 132, no. 11 (2006): 1413–1426.

Chowdhury, R., P. Flentje, and G. Bhattacharya. *Geotechnical slope analysis*. CRC Press, 2010.

Duk-Rodkin, A., and D. S. Lemmen. "Glacial history of the Mackenzie region." In *The physical environment of the Mackenzie Valley, Northwest Territories: a base line for the assessment of environmental change*. Edited by L. D. Dyke, & G. R. Brooks. Geological Survey of Canada, Bulletin 547, 2000. 11-20.

Dyke, L. "Stability of frozen and thawing slopes in the Mackenzie Valley, Northwest Territories." *57th Canadian Geotechnical Conference, 5th Joint CGS/IAH-CNC Conference*. Quebec, 2004.

Gillins, D. T., and S. F. Bartlett. "Multilinear regression equations for predicting lateral spread displacement from soil type and cone penetration test data." *Journal of Geotechnical and Geoenvironmental Engineering (ASCE)* 140, no. 4 (2014).

Hanna, A. J., and E. C. McRoberts. "Permafrost slope design for a buried oil pipeline." *Proceedings of the 5th International Conference on Permafrost*. 1988. 1247-1252.

Harder, L. F., and R. Boulanger. "Application of Ks and Ka correction factors." *NCEER Workshop on Evaluation of Liquefaction Resistance of Soils*. Salt Lake City, NV, 1997.

Harris, C., and A. G. Lewkowicz. "An analysis of the stability of thawing slopes, Ellesmere Island, Nunavut, Canada." *Canadian Geotechnical Journal* 37 (2000): 449-462.

Harris, C., and A. G. Lewkowicz. "Form and internal structure of active-layer detachment slides, Fosheim Peninsula, Ellesmere Island, Northwest Territories, Canada." *Canadian Journal of Earth Sciences* 30 (1993): 1708-1714.

Heginbottom, J. A., P. J. Kurfurst, and J. S. O. Lau. "Regional occurrence of permafrost, Mackenzie Valley, Canada." *Proceedings of the Third International Conference on Permafrost*. 1978. 399-405.

Hyndman, R. D., J. F. Cassidy, J. Adams, G. C. Rogers, and S. Mazzotti. "Earthquakes and seismic hazard in the Yukon-Beaufort Mackenzie." *CSEG Recorder*, 2005.

Ishihara, K. "Liquefaction and flow failure during earthquakes." *Geotechnique* 43, no. 3 (1993): 351-415.

Jahns, H. O., and C. E. Heuer. "Frost heave mitigation and permafrost protection for a buried chilled-gas pipeline." *Proceedings of the Permafrost Fourth International Conference*. Fairbanks: National Academy Press, 1983. 531-536.

Jibson, R. W. "Methods for assessing the stability of slopes during earthquakes - A retrospective." *Engineering Geology* 122 (2011): 43-50.

Jibson, R. W. *Predicting earthquake-induced landslide displacements using Newmark's sliding block analysis*. Washington, DC: Transportation Research Record 1411, 1993.

Jibson, R. W. "Regression models for estimating coseismic landslide displacement." *Engineering Geology* 91 (2007): 209-218.

Jibson, R. W., E. L. Harp, and J. A. Michael. "A method for producing digital probabilistic seismic landslide hazard maps." *Engineering Geology* 58 (2000): 271-289.

Juang, C. H., S. Y. Fang, and D. K. Li. "Reliability analysis of liquefaction potential of soils using standard penetration test." In *Reliability-based design in geotechnical engineering*, edited by K. K. Phoon, 497-526. New York, USA: Taylor & Francis Group, 2008.

Kavazanjian Jr, E., N. Matasovic, T. Hadj-Hamou, and P. J. Sabatini. *Geotechnical engineering circular #3, Design guidance: geotechnical earthquake engineering for highways, volume I - design principles*. Washington, DC: US Department of Transportation - Federal Highway Administration, 1997.

Kay, A. E., A. M. Allison, W. J. Botha, and W. J. Scott. "Continuous geophysical investigation for mapping permafrost distribution, Mackenzie Valley, N.W.T., Canada." *Proceedings of the Fourth International Permafrost Conference*. Fairbanks: National Academy Press, 1983. 578-583.

Kramer, S. L. *Geotechnical earthquake engineering*. Upper Saddle River, NJ: Prentice Hall, 1996.

Lee, E. M., and D. K. C. Jones. *Landslide risk assessment*. second ed. London: ICE Publishing, 2014.

Lewkowicz, A. G. "Morphology, frequency and magnitude of active-layer detachment slides, Fosheim Peninsula, Ellesmere Island, N.W.T." *Proceedings of the Fifth Canadian Permafrost Conference*. Quebec, 1990.

Lewkowicz, A. G., and C. Harris. "Morphology and geotechnique of active-layer detachment failures in discontinuous and continuous permafrost, northern Canada." *Geomorphology* 69 (2005): 275–297.

Liao, S. S. C., and R. V. Whitman. *Catalogue of liquefaction and non-liquefaction occurrences during earthquakes*. Cambridge, MA: Department of Civil Engineering, MIT, 1986.

Lipovsky, P., and C. Huscroft. *A reconnaissance inventory of permafrost-related landslides in the Pelly River watershed, central Yukon*. Whitehorse, YT: Yukon Geological Survey, 2006.

Malamud, B. D., D. L. Turcotte, F. Guzzetti, and P. Reichenbach. "Landslide inventories and their statistical properties." *Earth Surface Processes and Landforms* 29 (2004): 687-711.

Mathewson, C. C., and T. A. Mayer-Cole. "Development and runout of a detachment slide, Bracebridge Inlet, Bathurst Island, Northwest Territories, Canada ." *Bulletin of the Association of Engineering Geologists* XXI, no. 4 (1984): 407-424.

Matlab and Statistics Toolbox Release 2011b. Natick, MA: The MathWorks, Inc, 2011.

McRoberts, E. C. "A note on field observations of thawing in soils." *Canadian Geotechnical Journal*, 1975: 126-130.

McRoberts, E. C., and N. R. Morgenstern. "The stability of thawing slopes." *Canadian Geotechnical Journal* 11, no. 4 (1974): 447-469.

Monroe, J. S., and R. Wicander. *Physical geology: exploring the Earth*. St. Paul, MN: West Publishing Company, 1992.

Morgenstern, N. R., and J. F. Nixon. "One-dimensional consolidation of thawing soils." *Canadian Geotechnical Journal*, 1971: 558-565.

"Multi-hazard loss estimation methodology earthquake model HAZUS MH MR4 technical manual." Washington, DC: Federal Emergency Management Agency (FEMA), 2003.

National Building Code of Canada. Ottawa, ON: Associate Committee on the National Building Code, National Research Council of Canada, 2010.

Newmark, N. M. "Effects of earthquakes on dams and embankments." *Canadian Geotechnical Journal* 15 (1965): 139-159.

Nixon, J. F., R. Saunders, and J. Smith. "Permafrost and thermal interfaces from Norman Wells pipeline ditchwall logs." *Canadian Geotechnical Journal* 28 (1991): 738-745.

Paudel, B., and B. Wang. "Freeze-thaw effect on consolidation properties of fine grained soils from the Mackenzie Valley, Canada." *Geo Alberta*. Calgary, Alberta, 2010.

Phoon, K. K., and F. H. Kulhawy. "Characterization of geotechnical variability." *Canadian Geotechnical Journal* 36 (1999): 612-624.

Savigny, W., A. Isherwood, and A. Baumgard. *Mackenzie gas project, review of strain-based design- loadings, Appendix B*. Vancouver, BC: BGC Engineering Inc., 2005.

Seed, H. B., and I. M. Idriss. "Simplified procedure for evaluating soil liquefaction potential." *Journal of the Soil Mechanics and Foundations Division (ASCE)* 97 (1971): 1249-1273.

Seed, H. B., K. Tokimatsu, L. F. Harder, and R. M. Chung. "Influence of SPT procedures in soil liquefaction resistance evaluations." *Journal of Geotechnical Engineering (ASCE)* 111, no. 12 (1985): 1425-1445.

Seed, R. B., and L. F. Harder. "SPT-based analysis of cyclic pore pressure generation and undrained residual strength." *H. Bolton Seed Memorial Symposium*. Berkeley, 1990.

Travasarou, T., J. D. Bray, and N. A. Abrahamson. "Empirical attenuation relationship for Arias Intensity." *Earthquake Engineering and Structural Dynamics* 32 (2003): 1133-1155.

Uzielli, M., S. Lacasse, F. Nadim, and K. K. Phoon. *Soil variability analysis for geotechnical practice*. Vols. 3 and 4, In *Characterisation and engineering properties of natural soils*, edited by T. S. Tan, K. K. Phoon, D. W. Hight, & S. Leroueil, 1653-1752. London, UK: Taylor & Francis Group, 2007.

Wang, B., S. Nichol, and X. Su. "Geotechnical field observations of landslides in fine-grained permafrost soils in the Mackenzie Valley, Canada." In *Landslides, risk analysis and sustainable disaster management*, edited by K. Sassa, H. Fukuoka, F. Wang, & G. Wang, 203-212. Berlin: Springer, 2005.

Wieczorek, G. F., R. C. Wilson, and E. L. Harp. "Map showing slope stability during earthquakes in San Mateo County, California." US Geological Survey, 1985.

Wilson, R. C., and D. K. Keefer. "Predicting areal limits of earthquake-induced landsliding." *Evaluating earthquake hazards in the Los Angeles region-An earth-science perspective*. Edited by J. I. Ziony. US Geological Survey professional paper 1360, 1985. 317-345.

Youd, T. L., and D. M. Perkins. "Mapping liquefaction-induced ground failure potential." *Journal of Geotechnical Engineering (ASCE)* 104, no. 4 (1978): 433-446.

Youd, T. L., C. M. Hansen, and S. F. Bartlett. "Revised multilinear regression equations for prediction of lateral spread displacement." *Journal of Geotechnical and Geoenvironmental Engineering (ASCE)* 128, no. 12 (2002): 1007-1017.

Youd, T. L., et al. "Liquefaction resistance of soils: summary report from the 1996 NCEER and 1998 NCEER/NSF workshops on evaluation of liquefaction resistance of soils." *Journal of Geotechnical and Geoenvironmental Engineering (ASCE)* 127 (2001): 817-833.

Zhang, Y. *Impact of freeze-thaw on liquefaction potential and dynamic properties of Mabel Creek silt*. PhD dissertation, Fairbanks, AK: University of Alaska Fairbanks, 2009.

Chapter 6

6 Vulnerability of buried energy pipelines subject to earthquake-triggered landslides in permafrost thawing slopes⁵

6.1 Introduction

Alaska and northern Canadian oil and natural gas pipelines traverse vast permafrost terrains. In addition to permafrost-related geohazards (Nixon et al. 1990), the seismic activity in the region poses threat to their safety (Hyndman et al. 2005). The seismic transient ground shaking itself generates stresses and strains in the pipelines. It can also trigger ground failures such as slope instability and liquefaction, which lead to permanent ground deformations (PGD) that can compromise the pipeline integrity.

Active-layer detachment (ALD) is the most frequent landslide type in North American permafrost terrains (Dyke 2004, and Lipovsky and Huscroft 2006). Active layer is the surficial soil located on top of the permafrost table subjected to seasonal freeze/thaw cycles. ALD represents the instability of the active layer on sloped terrains, which can be triggered either by meteorological or seismic events. ALDs are characterized by their width (W), length (L) and scar length (L_s), as illustrated in Figure 6-1. Of interest for this study are seismic events during the thawing period, which can develop an ALD and endanger the safety of pipelines buried in the active layer (Figure 6-1a). In order to quantify the pipeline vulnerability to seismically-triggered ALD, it is necessary to determine the probability of exposure of a given pipeline to the ALD. Figure 6-1b shows schematically the random distribution of ALDs along a pipeline route, which may or may not impact the pipeline. Assuming that occurrence of ALDs along pipeline route can be expressed by Poisson distribution with the occurrence rate ν_{ALD} and standard lognormal distribution for the distance from the scar crown to the pipeline axis (S), the exposure index, I_E , in Chapter 5 was introduced as follows:

$$I_E = L - S \quad (6-1)$$

⁵ A version of this chapter has been submitted to the journal of Geotechnique.

where, $I_E > 0$ represents the case of pipeline exposure to ALD hazard.

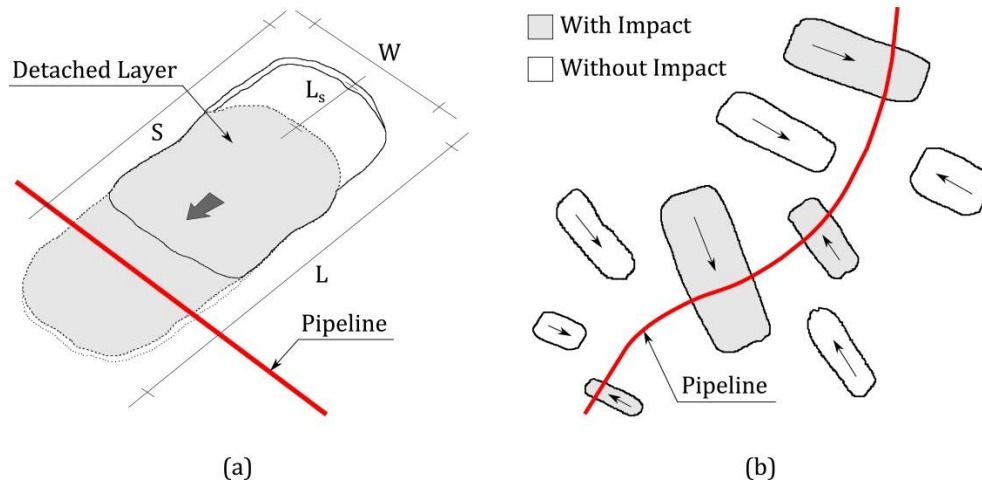


Figure 6-1: (a) Parameters that characterize an active-layer detachment (ALD) hazard: ALD width (W), length (L), scar length (L_s), and distance of scar crown to pipeline axis (S), and (b) distribution of ALDs along a pipeline route, which may or may not impact the pipeline.

Utilizing Monte Carlo simulation technique, a probabilistic seismic slope stability analysis procedure was developed in Chapter 5 to determine the probability of exposure, $P(\text{Exposure})=P(I_E > 0)$, and the extent of PGD hazard. The effect of thaw-consolidation phenomenon, which occurs in ice-rich fine-grained soils of permafrost regions, was introduced in the model considering the thaw-consolidation theory by Morgenstern and Nixon (1971). It explains the development of excess pore water pressure in the active layer subject to rapid thawing, where the thaw-consolidation ratio, R_{tc} , indicates the relationship between the active layer thawing and the consolidation rate. During normal thaw periods, $R_{tc}=0$ and no excess pore pressure is generated. However, in rapid thaw cycles resulting from forest fire or intense warm season, $R_{tc} > 0$ and excess pore water pressure develops in the soil. This excess pore water pressure promotes the slope instability and occurrence of ALD. The effects of four parameters critical to the development of ALD were studied in Chapter 5: distance of scar crown to pipeline axis (S), thaw-consolidation ratio (R_{tc}), earthquake moment magnitude (M) and source-to-site distance (R).

This chapter aims to propose a standardized analytical method for development of seismic vulnerability functions for continuous ductile pipelines subject to permanent ground deformations (PGD) caused by ALDs under permafrost conditions. A structural analysis program that considers different limit states of collapse was developed, validated and applied for damage assessment in pipelines under PGDs with different geometries. To reduce the computational effort, the program uses only frame elements to model geometrical nonlinearities. Monte Carlo technique is employed to simulate PGD zone geometrical uncertainties. The generated pipeline seismic vulnerability functions correlate the repair rate per unit length to the PGD extent.

6.2 Seismic vulnerability function

Seismic vulnerability function, also referred to as “fragility” or “damage” function, may be expressed by: (i) the probability that a structure attains or exceeds a given damage state level (widely used for buildings and bridges); or (ii) the repair rate per unit length (particularly useful for linear structures, e.g., pipelines). In both cases, it is a function of an appropriate seismic intensity measure representative of the earthquake severity and confirmed empirically or analytically to have strong correlation with the observed damage. For example, peak ground acceleration (PGA), peak ground velocity (PGV) and spectral displacement (S_d) have typically been employed as intensity measures for building vulnerability (FEMA 2003, and SYNER-G 2013). On the other hand, PGV is used as intensity measure for buried pipelines subjected to transient ground shaking, and permanent ground deformation (PGD) for pipelines subjected to ground failure (landslide and liquefaction) (ALA 2001a, FEMA 2003, and SYNER-G 2013). Generally, vulnerability functions can be derived using empirical observations in the field following damaging earthquakes, applying analytical methods, expert’s opinion, or any combination of these (SYNER-G 2013, and Porter 2015).

The empirical functions are useful as they account for real structural and site conditions such as state of pipeline corrosion, soil type and heterogeneity, etc. However, since they are usually developed based on a few damage records in specific pipeline configurations (diameter, material, connections, etc.), and subjected to a limited number of moderate to

strong seismic events scenarios with uncertain local intensity, they cannot be representative of all ground shaking intensities and geotechnical and structural settings. Therefore, the resulting empirical functions have limited capability to predict the damage under the full spectrum of potential field conditions.

The analytical approach considers numerical simulations of the nonlinear dynamic structural response and employs a comprehensive set of conditions including those that yet have not been experienced by similar structures. This method overcomes the main setback of the empirical method as the input parameters related to the hazard, site and structure are rather continuous and not limited to particular observed conditions. In this case, the focus has to be on the validation of the results with field records. In the expert opinion approach, which seems to be outperformed by the previous two methods (SYNER-G 2013), the opinions of a small group of experts about the extent of the damage under particular conditions are collected. The quality of the results depends on the experts' knowledge and estimation ability which cannot be evaluated easily. This method is only used in the absence of empirical observations and when numerical simulations are disregarded due to insufficient input parameters or high computational costs.

The majority of pipeline vulnerability functions found in the literature are derived empirically (e.g., Barenberg 1988, Honegger and Eguchi 1992, and O'Rourke and Ayala 1993). On the other hand, the analytical approach has been widely used for above-ground engineering structures, buildings and bridges (e.g., Kircher et al. 1997, Shinozuka et al. 2000, Nielson and DesRoches 2007, and Porter et al. 2014), and rarely for buried pipelines (e.g., Terzi et al. 2007). It can be speculated that the analytical approach is not popular from buried pipelines due to limited development in the soil-pipe interaction modelling and the high inherent uncertainty of the soil properties. Application of the experts' opinion approach can only be seen in the case of buried pipelines subjected to ground failure in the research work of Eguchi (1983) and in the American Lifelines Alliance (ALA) guidelines for seismic vulnerability of water pipelines (ALA 2001a).

Almost all available pipeline vulnerability functions (empirical, analytical and expert opinion) consider damage (leak or break) in brittle and segmented pipelines. To assess the potential damage in ductile pipes, there is no exclusive vulnerability function); for example, Hazus (FEMA 2003), applies the functions of Honegger and Eguchi (1992) developed for brittle and segmented cast iron water pipes with a correction factor of 0.3.

6.3 Analysis of pipeline damage

The fundamental part of the analytical methods for development of seismic vulnerability functions consists of performing comprehensive analyses to quantify the pipeline damage. In the current study, a nonlinear finite element program, which accounts for large deformations, was developed in Matlab (The MathWorks, Inc. 2011). The program combines frame elements with Winkler elastoplastic springs in three perpendicular directions to simulate soil-pipe interaction. The spring force-deformation characteristics, i.e., yield force and respective displacement, were determined according to ALA's guideline for design of buried steel pipes (ALA 2001b).

6.3.1 Loading and boundary conditions

The vulnerability of buried pipelines to PGD depends on the soil and pipe properties as well as the ALD geometry. The effects of ALD width, maximum displacement and spatial PGD variation on the pipeline deformation are considered by applying the equation suggested by Liu and O'Rourke (1997), i.e.:

$$y(x) = \frac{\delta}{2} \left[1 - \cos \left(\frac{2\pi x}{W} \right) \right] \quad (6-2)$$

where, y is the ground deformation at distance x from the margin of the PGD zone, δ is the peak value of PGD and W is the ALD width. Figure 6-2 illustrates the spatial PGD variation and the corresponding pipeline deformation.

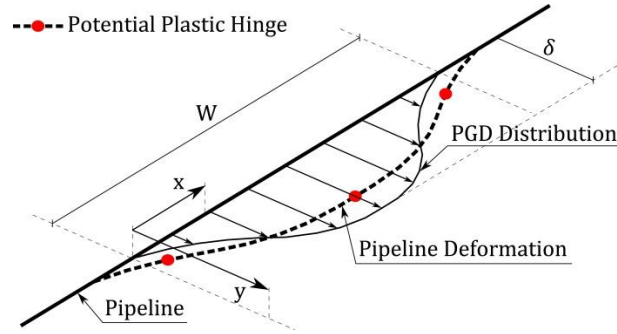


Figure 6-2: PGD spatial variation and locations of the potential plastic hinges on pipeline.

Lewkowicz (1990) studied the characteristics of ALDs occurred at three sites on the Fosheim Peninsula, a continuous permafrost region in the Canadian territory of Nunavut, and concluded that their morphological characteristics are lognormally distributed. Using the statistical data presented by Lewkowicz, in Chapter 5 the lognormal distribution parameters of ALD width W (in metres) were estimated with $\mu = 2.284$ and $\sigma = 0.707$. It was also shown that the earthquake-induced PGDs follow the Weibull distribution with large coefficients of variation (COV). Table 6-1 summarizes the main findings of the statistical analysis of the four parameters that impact the pipeline vulnerability: distance of scar crown to pipeline axis (S), thaw-consolidation ratio, earthquake moment magnitude (M) and source-to-site distance (R).

Table 6-1: Probability of exposure and the peak PGD (δ) Weibull distribution parameters from Chapter 5.

	S (m)			R_{tc}			M			R (km)		
	50	80	110	0	1.5	3	5.5	6.5	7.5	10	40	80
P(Exposure)	0.028	0.015	0.008	0.015	0.050	0.070	0.007	0.015	0.043	0.056	0.015	0.007
δ Mean (m)	9.30	9.85	9.85	9.85	18.46	19.83	1.28	9.85	22.55	21.51	9.85	3.33
δ COV* (%)	246	236	245	236	147	145	608	236	142	157	236	375
Shape Factor	0.421	0.389	0.299	0.389	6.210	8.206	0.001	0.389	13.86	10.19	0.389	0.015
Scale Factor	0.215	0.211	0.208	0.211	0.318	0.352	0.195	0.211	0.496	0.405	0.211	0.198

*COV stands for coefficient of variation.

The following considerations were introduced in the developed finite element program. The base of the transverse horizontal springs of the PGD zone has identical displacement as the input ground motion whereas the base of the horizontal springs located outside the PGD zone is fixed. The considered segment of the pipeline model should be long enough such that its response remains unaffected by the considered length. To this goal, as a

criterion the induced bending strains at the segment margins were limited to a maximum 1×10^{-5} by O'Rourke (1988). As well, according to Suzuki et al. (1988) and Liu and O'Rourke (1997) the axial pipeline movement should be accommodated by the axial soil-pipe friction, implying no bending or axial strains development at the segment margins. In the current study, the modelled length of the segment is considered sufficiently long so that only negligible internal forces can be developed at the ends.

6.3.2 Plastic hinges

During the step-by-step analysis, the program accounts for the development of plastic hinges to capture the material and geometric nonlinearities of the pipeline. Approximate locations of the potential plastic hinges are depicted in Figure 6-2. Each plastic hinge is formed of a number of linear and nonlinear frame elements spatially configured in a cylindrical shape with a diameter equal to that of the pipe. The side and front views of this spatial plastic hinge are shown in Figure 6-3a. Material nonlinearity in the hinges is modelled by the Ramberg-Osgood equation (Ramberg and Osgood 1943). The nonlinear elements in Figure 6-3 have discretized the cross-sectional area of the pipe. Stress and strain at each point on the cross-section can be estimated from the deformation and secant elasticity modulus of the corresponding nonlinear element at each step. The role of the linear elements of the hinge is to maintain its stability and to prevent the hinge cross-section from distortion, i.e., the planar surfaces remain planar under bending moment (Figure 6-3b).

The geometric nonlinearity of the cross-section (ovalization), which impacts its mechanical properties and stability, is incorporated in the plastic hinge based on the results of Chapter 2. The relationships between the cross-sectional ovalization and curvature as well as the potential premature failure at plastic hinges of the buried pipes were numerically investigated in Chapter 2. The initial cylindrical configurations of the plastic hinges follow the obtained relationships and gradually transform to elliptic cylinders. This cross-sectional transformation is shown in Figure 6-3b.

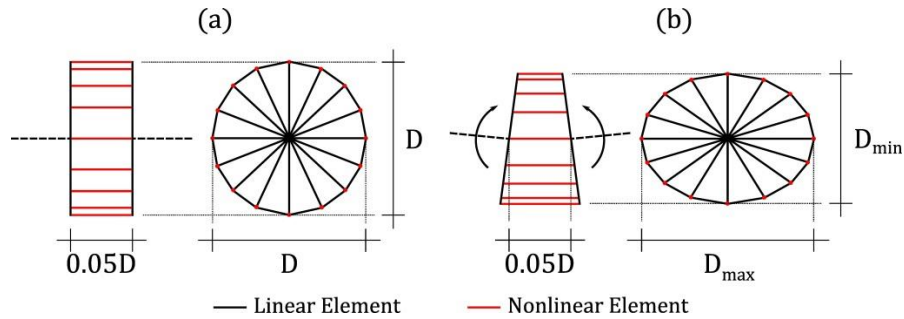


Figure 6-3: The side and front views of (a) undeformed plastic hinge, and (b) deformed plastic hinge under a bending moment.

The performance of the plastic hinge was calibrated against the experimental results of Sherman (1983) on the pure bending of cylinders. The results agreed well for the case of a plastic hinge with 16 nonlinear elements. The response was evaluated for two cross-section configurations: slender with $D/t=96$ and non-slender with $D/t=36$ to examine the ability of the plastic hinge to simulate the impact of the wall-thickness ratio (D/t) on the pipe mechanical behaviour. The obtained moment-curvatures were normalized with respect to yield moments and curvatures (Figure 6-4a). The excellent agreement between the results suggests that the considered plastic hinge is capable of simulating behaviour of pipes with an extensive D/t range.

The calibrated hinge representing a pipe with $D/t=36$ was then subjected to 5 different combinations of bending moment and axial force to verify its ability to simulate bending moment-axial force interactions. The resulting normalized moment-curvatures are compared to the analytical curves of Sohal and Chen (1987) in Figure 6-4b. The small discrepancy between the results can be explained by the different assumptions made for the ovalized shape of pipe cross-section in the two studies.

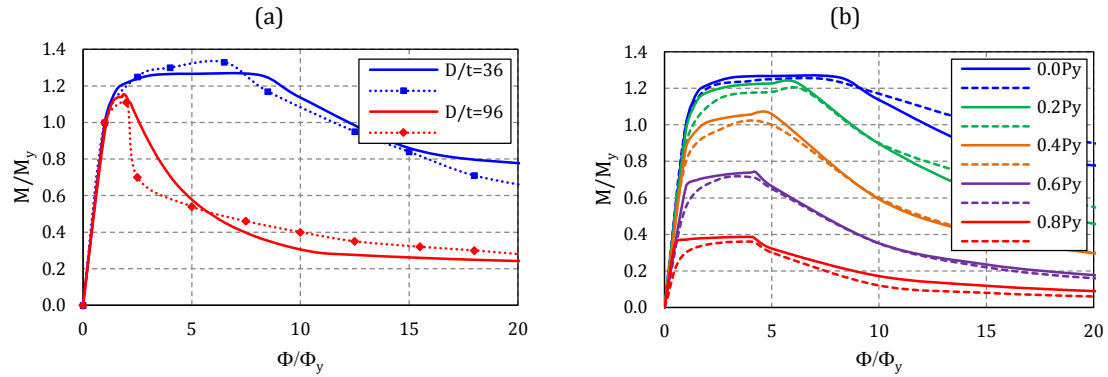


Figure 6-4: Normalized moment-curvatures resulted from the present study (continuous lines) compared to (a) experimental results of Sherman (1983) for pure bending ($D/t=36$ and 96), and (b) analytical results of Sohal and Chen (1987) for combined bending moment-axial force only ($D/t=36$). M_y , Φ_y and P_y represent the yield moment, yield curvature and yield axial force of the cross-section, respectively.

The Canadian standard for oil and gas pipeline systems (CAN-CSA Z662) limits the internal pressure-induced hoop stress to 80% of the specified minimum yield strength (SMYS) of the steel. The proposed plastic hinge can be applied to the analysis of internally pressurized pipes by simply modifying the yield capacity of the nonlinear elements according to the Von Mises criterion. The procedure is shown in Figure 5a where the internal pressure-induced hoop stress (σ_H) is associated with the seismic-induced longitudinal stress (σ_L), which subjects the pipe wall to a biaxial stress condition. According to the Von Mises yield criterion, an increase in internal pressure would increase the yield stress in tension whereas it reduces the yield stress in compression (Figure 6-5b). The maximum developed hoop stress permitted by CAN-CSA Z662 along with its corresponding yield stresses in tension and compression, denoted by $\sigma_{y(80)}^+$ and $\sigma_{y(80)}^-$, respectively, are also shown in Figure 6-5b. The original stress-strain curve under zero internal pressure as well as the modified curve for the most critical condition, i.e., $\sigma_H = 0.8SMYS$, are shown in Figure 6-5c. These yield corrections render the plastic hinge suitable for simulating the ultimate flexural behaviour of the pressurized pipes.

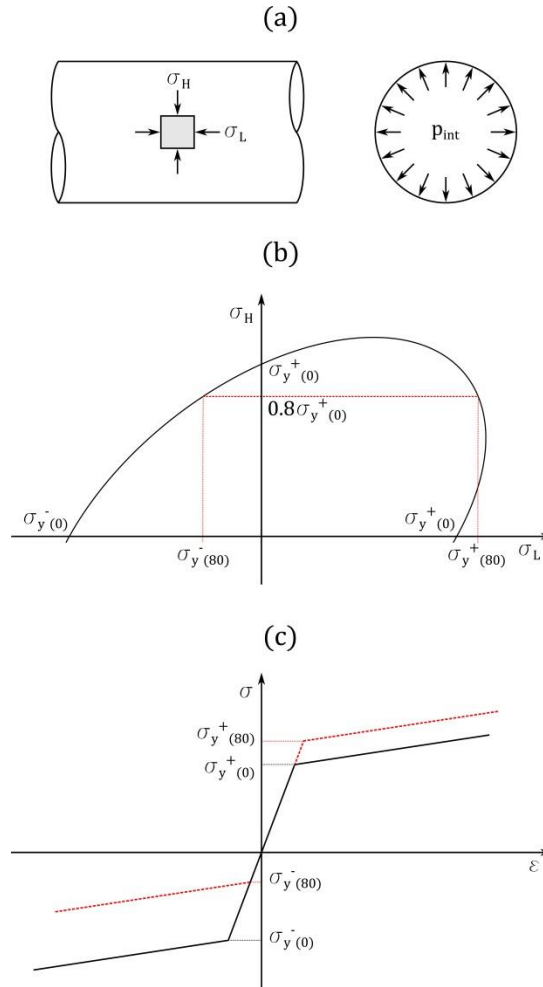


Figure 6-5: Modification of the yield capacity of the pressurized pipes: (a) biaxial stress condition, (b) the Von Mises yield criterion, and (c) the corrected stress-strain curves based on the Von Mises criterion.

6.3.3 Damage state indication

Damage indicators related to the potential modes of failure were employed to quantify the PGD damage to pipeline (leaks/breaks). Two modes of failure have been considered herein: tensile rupture and local buckling. The beam buckling failure, which may also occur only in case of pipelines with shallow burial depth under longitudinal loading, was not considered. In the absence of detailed information on the pipe and weldment, CAN-CSA Z662 ultimate tensile strain capacity (ϵ_t^{ult}) of 0.0075 was assumed. To prevent

local buckling, CAN-CSA Z662 limits the ultimate compressive strain capacity (ϵ_c^{ult}) given by:

$$\epsilon_c^{ult} = 0.5 \left(\frac{t}{D} \right) - 0.0025 + 3000 \left[\frac{(p_{int} - p_{ext})D}{2tE} \right]^2 \quad (6-3)$$

where, t is the pipe wall-thickness, D is the pipe outside diameter, E is the steel modulus of elasticity, and p_{int} and p_{ext} are the internal and external pressures, respectively. In addition, to prevent local instabilities caused by cross-sectional ovalization, CAN-CSA Z662 also limits the ovalization deformation (OV_{CSA}) by:

$$OV_{CSA} = 2 \left(\frac{D_{max} - D_{min}}{D_{max} + D_{min}} \right) \quad (6-4)$$

where, D_{max} and D_{min} are the maximum and minimum outside diameters of the pipe when it is subjected to bending moment as shown in Figure 6-3b. In the absence of pertinent data, OV_{CSA} can be taken as 0.03, and may be increased up to 0.06 for cases where it can be proved that the premature failure will not happen. The ALA defines the ovalization as (ALA 2001b):

$$OV_{ALA} = \frac{D - D_{min}}{D} \quad (6-5)$$

with suggested maximum allowable OV_{ALA} of 0.15. Assuming equal cross-sectional deformation in the bending plane ($D - D_{min}$) and in the plane perpendicular to it ($D_{max} - D$), the two ovalization indicators can be approximately correlated as:

$$OV_{CSA} \approx 0.5OV_{ALA} \quad (6-6)$$

Effects of burial depth, soil stiffness and internal pressure on the ovalization of typical energy pipelines subjected to bending were studied in Chapter 2 and it was shown that only unpressurized slender pipes (with large D/t) buried in dense soils in the practical normalized burial depth ranges (H/D) may experience OV_{CSA}^{ult} up to 0.07. Also, it was shown that in the case of pressurized pipes under the maximum allowed internal pressure, cross-sectional ovalization of the pipes is independent of D/t and can be ignored. However, the premature failure of the pressurized pipes should still be considered in the

analysis. In the current study, the value of 0.06 is used as reasonable estimate of the ultimate ovalization factor of the unpressurized pipes.

All three types of damage: tensile rupture, local buckling and premature cross-sectional failure along the pipeline can be modelled by the developed plastic hinge model.

6.3.4 Model validation

To validate the finite element program, pipeline response subjected to PGD was compared with results from Abaqus models obtained by Liu and O'Rourke (1997). The comparison is given in Figure 6-6 for a 400 m-long segment of pipeline with $D=0.61$ m and $D/t=64$ made of X52 steel subjected to three widths of the PGD zone: 10, 20 and 30 m. As it can be seen, excellent agreement is obtained for the bending moment (Figure 6-6a), axial force (Figure 6-6b) and maximum pipe strains (Figure 6-6c).

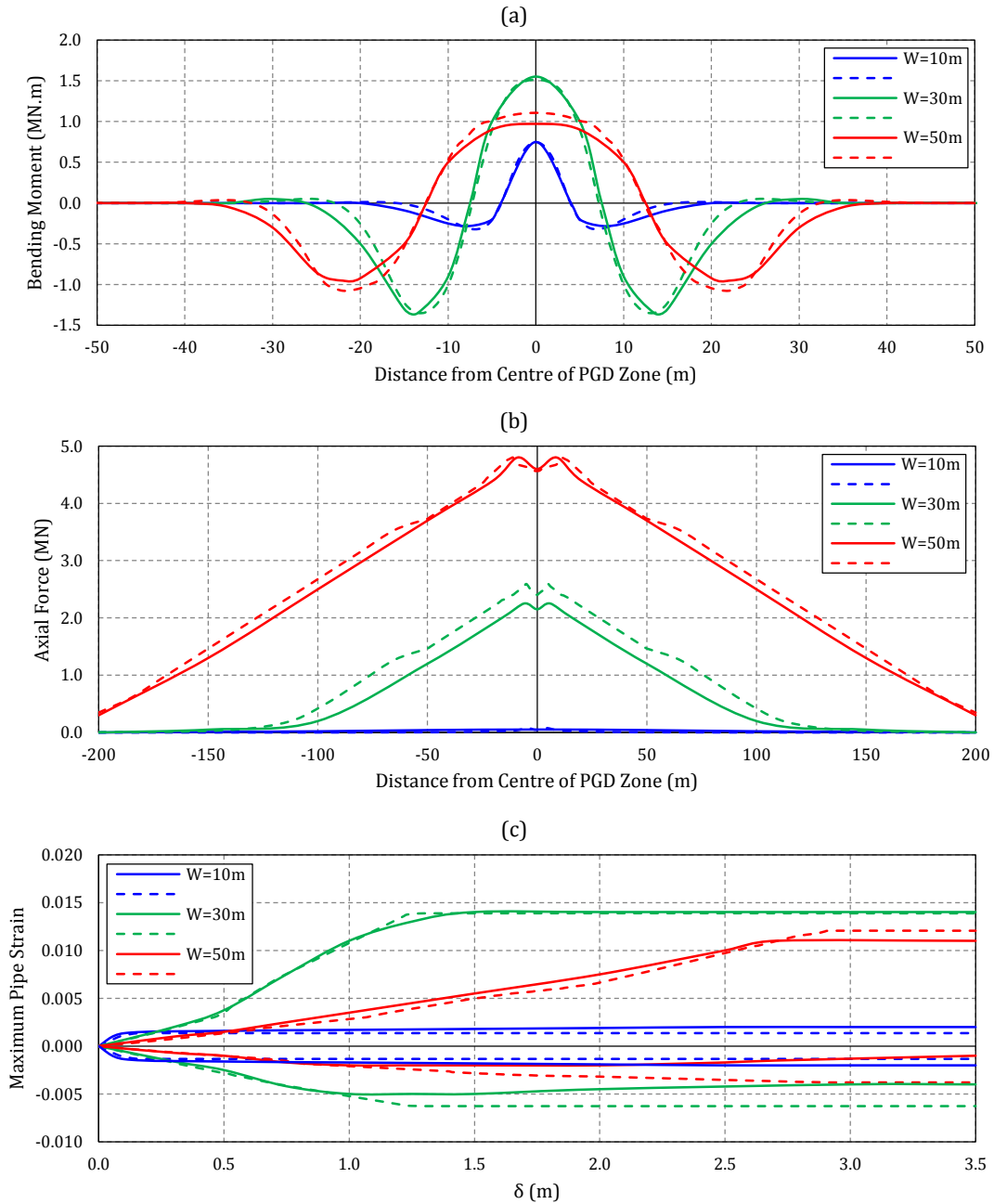


Figure 6-6: Responses of a 400m-long segment of pipeline with $D=0.61$ m and $D/t=64$ made of X52 steel subjected to three levels of PGD zone width (W). Comparison of (a) bending moments, (b) axial forces and (c) maximum pipe strains resulted from this study with those of Liu and O'Rourke (1997). Results of this study are presented with dashed lines.

6.4 Damage evaluation

In this section, vulnerability of a 600 m-long straight pipeline segment (flawless and corrosion free) with $D=0.61$ m and $D/t=78$ made of X52 steel is investigated. Two extreme limits of the internal pressure are considered, i.e., zero and the maximum allowed by CAN-CSA Z662. Considering burial depth of $H=1$ m and soil friction angle, cohesion and dry unit weight as $\phi' = 26^\circ$, $c' = 2.5$ kPa and $\gamma_d = 16$ kN/m³, respectively, the nonlinear soil spring relationships are calculated according to ALA (2001b). The results of this simulation for the three PGD widths are shown in Figure 6-7. It can be observed that beyond a certain level of δ , the response remains constant as a result of soil failure along the part of the PGD zone that applies active pressure to pipeline. Accordingly, this is the worst condition that a pipeline may experience in the PGD zone. In Figures 6-7a and b, this maximum δ can be detected with the onset of the plateau-type shape of both strain and ovalization responses.

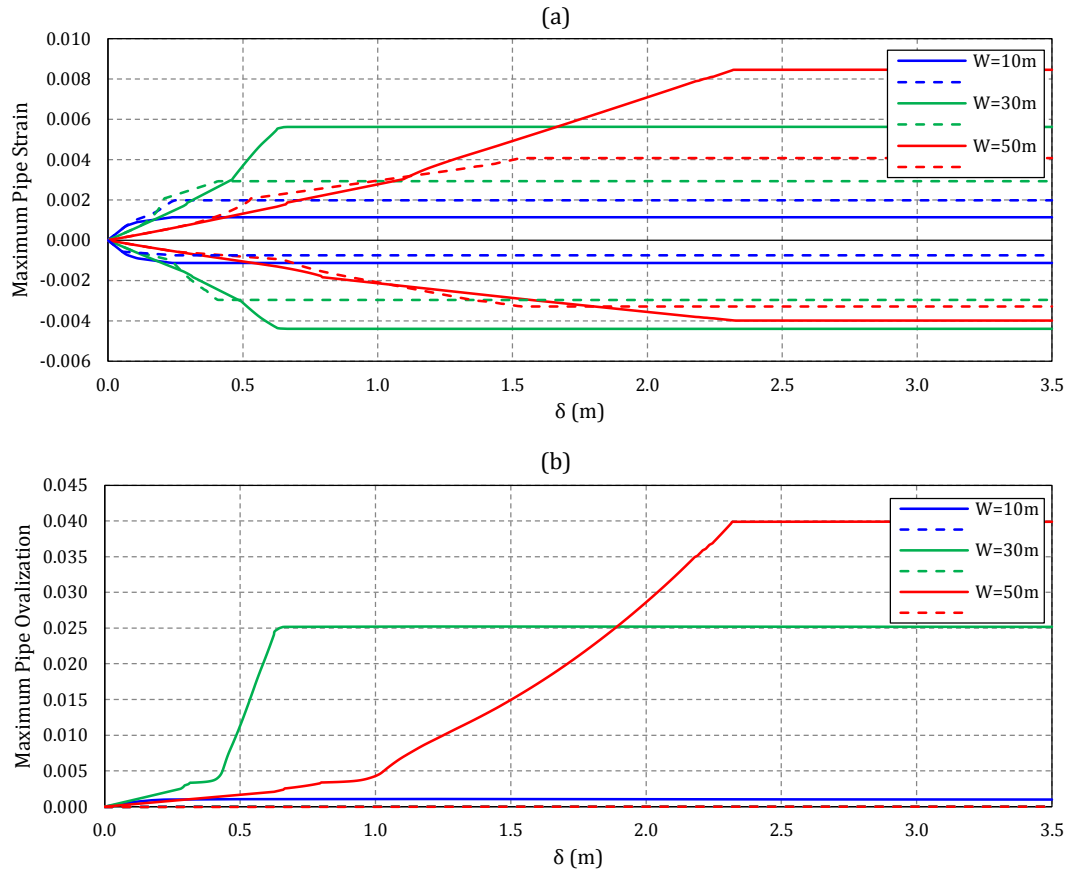


Figure 6-7: (a) Maximum pipe strains and (b) maximum pipe ovalization according to ALA (2001b) definition in a 600 m-long segment of pipeline with $D=0.61$ m and $D/t=78$ made of X52 steel subjected to three levels of PGD zone width (W). Results of the simulations for the pressurized pipes are shown with dashed lines.

The critical value of PGD, δ_{cr} , beyond which a damage occurs can be derived as a function of W using the analysis results considering $\epsilon_t^{ult} = 0.0075$, $\epsilon_c^{ult} = -0.0039$ and $OV_{ALA}^{ult} = 0.12$ for unpressurized pipe conditions; and using $\epsilon_t^{ult} = 0.0075$, $\epsilon_c^{ult} = -0.0101$ and $OV_{ALA}^{ult} = 0.00$ for pressurized conditions. In the first case and for the practical range of W of up to 50 m, the resulting relationship shows asymptotical behaviour. As can be seen in Figure 6-8, for $W \leq 10$ m, the value of the function should be considered as infinity. In the case of a pressurized pipe, no damage could be observed within the practical range of W because ϵ_c^{ult} was larger and consequently the pipe wall was more stable.

A Monte Carlo simulation was performed to obtain the average number of repairs using the function shown in Figure 6-8 as a damage triggering indicator. Three repairs were assigned corresponding to a single ALD and analog to the 3 plastic hinges that develop as a consequence (Figure 6-2). In the simulations, W and δ were assumed independent and randomly generated according to their respective statistical distributions, i.e., lognormal and Weibull. The lognormal parameters of W were discussed earlier in Section 6.3.1 ($\mu = 2.284$ and $\sigma = 0.707$), whereas the Weibull parameters (shape and scale factors) were treated as variables in the simulations. The resulting average number of repairs per ALD, RR_{ALD} , obtained by varying mean δ is shown in Figure 6-9. The effect of the COV levels of δ on the results was studied through the simulations. As it can be seen, for large mean values of δ , RR_{ALD} approaches the maximum number of 3 for one ALD, however, the convergence rate varies for different values of COV.

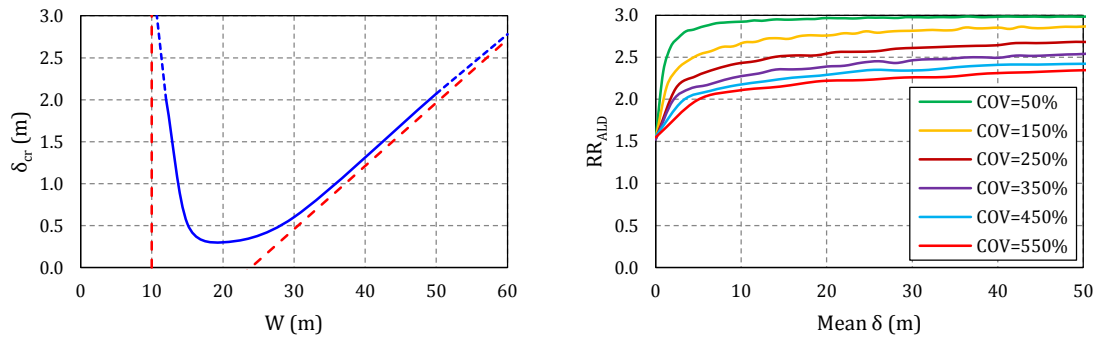


Figure 6-8: Critical values of peak PGD, δ_{cr} , as a function of PGD zone width, W , for unpressurized pipes. **Figure 6-9: Repairs for one ALD, RR_{ALD} , as a function of mean and COV of δ .**

The average number of repairs RR_{ALD} vs. mean δ relationships in Figure 6-9 can be used for practical applications to determine RR_{ALD} when the mean and COV of δ are known. The repair rate (number of repairs per km) can then be calculated from the probability of exposure and mean occurrence rate of ALD (discussed in Section 6.1 and shown in Figure 6-1b) as follows:

$$RR = P(E) \cdot v_{ALD} \cdot RR_{ALD} \quad (6-7)$$

A 13 km-length segment of pipeline with standard properties discussed earlier, subjected to M6.5 scenario earthquake with a source-to-site distance equal to 10 km in a region with $v_{ALD} = 12$ per km is considered herein as an example to demonstrate the power of the proposed method. From Table 6-2 the mean δ is 21.51 m and its COV is 157%. According to Figure 6-9 the corresponding RR_{ALD} will be approximately 2.8 and the repair rate is obtained as:

$$RR = (0.056) \cdot (12) \cdot (2.8) = 1.88 \text{ per km}$$

and the number of repairs for the total considered length of the pipeline is:

$$(13) \cdot (1.88) = 24.4 \approx 25$$

Accordingly, 25 repairs can be expected in average for this hypothetical scenario. According to FEMA (2003) 80% of the damages due to PGD are breaks of the pipeline and 20% are simple leaks. Assuming this definition, about 20 breaks and 5 leaks could be expected over the 13 km of the pipeline. In another example, increasing the source-to-site distance to 40 km, reduces the repair rate to:

$$RR = (0.015) \cdot (12) \cdot (2.5) = 0.45 \text{ per km}$$

with the total number of repairs equal to:

$$(13) \cdot (0.45) = 5.85 \approx 6$$

from which, 5 breaks and 1 leak are to be expected.

6.5 Summary and conclusions

Vulnerability functions for buried energy pipelines subject to earthquake-triggered active layer detachment (ALD) in permafrost regions were determined. They give the average number of repairs to be expected for a given scenario. A nonlinear finite element program that accounts for large deformations was developed in Matlab environment in order to analyze the pipeline vulnerability. The following standardized analysis steps were then applied:

(i) Development of a function, which relates critical level of PGD, δ_{cr} , to the width of PGD zone, W . This function has a vertical asymptote corresponding to the minimal width below which any PGD cannot cause damage to the pipeline.

(ii) Performing Monte Carlo simulations using the function derived from the previous step along with statistical distribution of PGD zone width to obtain relationship of the average number of repairs per ALD to the δ mean and COV values.

(iii) Computation of the repair rate for unit length of a pipeline multiplying the probability of exposure with the ALD occurrence rate and the number of repairs per ALD.

The effect of internal pressure on damage was also investigated for the special case of the maximum code permitted pressure and it was shown that highly pressurized pipes appear to be more resistant against PGD hazards. The application of the proposed procedure was demonstrated through a simple example of a buried pipeline subject to a seismic scenario.

Beside the pipeline properties and the local geotechnical conditions, the accuracy of the results obviously depends on the assumptions made for quantifying the ALD hazard itself. To decrease uncertainties, future research topics should include the following:

- Improvement of the quality of the input parameters used for hazard analysis by performing detail site investigations.
- Determination of the potential locations of the ALDs along pipeline routes and estimation of the site-specific occurrence rates.

References

Barenberg, M. E. "Correlation of pipe damage with ground motion." *Journal of Geotechnical Engineering (ASCE)* 114, no. 6 (1988): 706-711.

CSA Z662-03 oil and gas pipeline systems. Mississauga, ON: Canadian Standards Association, 2003.

D8.10 - Guidelines for deriving seismic fragility functions of elements at risk: Buildings, lifelines, transportation networks and critical facilities. Ispra, Italy: European

Commission Joint Research Centre, Institute for the Protection and Security of the Citizen, 2013.

Dyke, L. "Stability of frozen and thawing slopes in the Mackenzie Valley, Northwest Territories." *57th Canadian Geotechnical Conference, 5th Joint CGS/IAH-CNC Conference*. Quebec, 2004.

Eguchi, R. T. "Earthquake behavior and safety of oil and gas storage facilities, buried pipelines, and equipment." *International Symposium on Lifeline Earthquake Engineering, the 4th National Congress on Pressure Vessel and Piping Technology*. Portland, Oregon, 1983.

Guideline for the design of buried steel pipe. American Lifelines Alliance, 2001.

Honegger, D. G., and R. T. Eguchi. "Determination of the relative vulnerabilities to seismic damage for San Diego County Water Authority: water transmission pipelines." 1992.

Hyndman, R. D., J. F. Cassidy, J. Adams, G. C. Rogers, and S. Mazzotti. "Earthquakes and seismic hazard in the Yukon-Beaufort Mackenzie." *CSEG Recorder*, 2005.

Kircher, C. A., A. A. Nassar, O. Kustu, and W. T. Holmes. "Development of building damage functions for earthquake loss estimation." *Earthquake Spectra* 13, no. 4 (1997): 663-682.

Lewkowicz, A. G. "Morphology, frequency and magnitude of active-layer detachment slides, Fosheim Peninsula, Ellesmere Island, N.W.T." *Proceedings of the Fifth Canadian Permafrost Conference*. Quebec, 1990.

Lipovsky, P., and C. Huscroft. *A reconnaissance inventory of permafrost-related landslides in the Pelly River watershed, central Yukon*. Whitehorse, YT: Yukon Geological Survey, 2006.

Liu, X., and M. J. O'Rourke. "Behaviour of continuous pipeline subject to transverse PGD." *Earthquake Engineering and Structural Dynamics* 26 (1997): 989-1003.

Matlab and Statistics Toolbox Release 2011b. Natick, MA: The MathWorks, Inc., 2011.

Morgenstern, N. R., and J. F. Nixon. "One-dimensional consolidation of thawing soils." *Canadian Geotechnical Journal* 8 (1971): 558-565.

"Multi-hazard loss estimation methodology earthquake model HAZUS MH MR4 technical manual." Washington, DC: Federal Emergency Management Agency (FEMA), 2003.

Nielson, B. G., and R. DesRoches. "Analytical seismic fragility curves for typical bridges in the central and southeastern United States." *Earthquake Spectra* 23, no. 3 (2007): 615-633.

Nixon, J. F., K. A. Sortland, and D. A. James. "Geotechnical aspects of northern gas pipeline design." *The fifth Canadian Permafrost Conference*. Quebec, 1990.

O'Rourke, M. J., and G. Ayala. "Pipeline damage due to wave propagation." *Journal of Geotechnical Engineering (ASCE)* 119, no. 9 (1993): 1490-1498.

O'Rourke, T. D. "Critical aspects of soil-pipeline interaction for large ground deformation." *1st Japan-US Workshop on Liquefaction, Large Ground Deformation and Their Effects on Lifeline Facilities*. 1988. 118-126.

Porter, K. *A beginner's guide to fragility, vulnerability and risk*. Denver, CO, USA: University of Colorado Boulder, 2015.

Porter, K., K. Farokhnia, D. Vamvatsikos, and I. Cho. *Analytical derivation of seismic vulnerability functions for building classes and nonstructural components, emphasizing highrise buildings*. Global Vulnerability Consortium, 2014.

Ramberg, W., and W. R. Osgood. *Description of stress-strain curves by three parameters*. Washington DC: Technical Note No. 902, National Advisory Committee For Aeronautics, 1943.

Seismic fragility formulations for water systems, Part 2- Appendices. American Lifelines Alliance, 2001.

Sherman, D. R. *Report on bending capacity of fabricated pipes*. Milwaukee, WI, USA: Department of Civil Engineering, University of Wisconsin, 1983.

Shinozuka, M., M. Q. Feng, H. Kim, and S. Kim. "Nonlinear static procedure for fragility curve development." *Journal of Engineering Mechanics (ASCE)* 126, no. 12 (2000): 1287-1295.

Sohal, I. S., and W. F. Chen. "Local buckling and sectional behavior of fabricated tubes." *Journal of Structural Engineering (ASCE)* 113, no. 3 (1987): 519-533.

Suzuki, N., O. Arata, and I. Suzuki. "Subject to liquefaction-induced permanent ground displacement." *1st Japan-US Workshop on Liquefaction, Large Ground Deformation and Their Effects on Lifeline Facilities*. 1988. 155-162.

Terzi, V. G., M. N. Alexoudi, and T. N. Hatzigogos. "Numerical assessment of damage state of segmented pipelines due to permanent ground deformation." *10th International Conference on Applications of Statistics and Probability in Civil Engineering*. Tokyo, Japan, 2007.

Chapter 7

7 Summary and conclusions

7.1 Summary

This thesis covered several topics related to the seismic response of buried energy pipelines in cold regions. The important aspects of seismic response of energy pipelines in permafrost are discussed in the main chapters of research (i.e., Chapters 2 to 6). Here is a summary of what was addressed in these chapters:

- In Chapter 2, cross-sectional ovalization of buried steel pipes subjected to bending moment induced by end displacements was discussed. A three dimensional finite element analysis was conducted employing the commercially available Abaqus software. The pipe was simulated using 3D shell elements while discrete nonlinear springs were employed to simulate the saturated sand soil medium along the pipeline. The effects of the burial depth to pipe diameter ratio (H/D ; normalized depth), diameter to wall-thickness ratio (D/t), sand density and the internal pressure on the ovalization were investigated, and resulting ovalization distribution with respect to bending moment at critical sections was presented.
- In Chapter 3, seismic site response under discontinuous permafrost conditions was discussed. Both experimental and numerical investigations were conducted to examine this peculiar problem. The experimental program included a series of 1g shaking table tests on small-scale models. Nonlinear numerical analyses were performed employing the commercially available FLAC software and the models were calibrated with the experimental results. Parametric simulations were then conducted in predictive mode to study the variations of the free-field spectral accelerations (on top of the frozen blocks and unfrozen soils) with different spatial configurations of the frozen and unfrozen soils, and to determine the key parameters and their effects on the seismic site response.
- In Chapter 4, the role of discontinuous permafrost in the manifestation of differential transient ground deformations was studied. Results of experimental and numerical analyses of the site response in discontinuous permafrost, obtained

in Chapter 3, were the basis for investigation of the seismic response of continuous buried pipelines. Soil-pipe interactions were simulated with finite element software developed especially for this purpose. Validation of the results was done against numerical and analytical solutions available in the literature. Parametric analyses were performed to investigate the pipe axial and bending strains as functions of the following parameters: seismic wave type, soil density, distribution of frozen soil along the pipeline, frequency of soil particle vibration, pipe cross-sectional properties and burial depth. Depending whether the pipe is fully or partially buried in the active layer, two cases for spatial distribution of soil stiffness were accounted for: identical support stiffness (ISS) and multiple support stiffness (MSS). For each case, variations in pipe axial and bending strains with the wave angle of incidence were derived.

- Chapter 5 addressed the occurrence of earthquake-induced active layer detachment (ALD) hazard and developed a standardised risk assessment framework for existing and future linear infrastructure such as pipelines, bridges and roads traversing permafrost regions. The potential for earthquake-triggered ALD was analytically quantified. Morphological statistics for the Canadian North were combined with seismic slope stability analyses to determine the probability of buried pipeline exposure to permanent ground deformations (PGD) caused by ALD, and the extent of the potential PGD. Monte Carlo technique was applied to simulate and assess the sensitivity of the model parameters to earthquake magnitude and source-to-site distance.
- Chapter 6 proposed an analytical method for assessment of vulnerability of ductile energy pipelines traversing permafrost regions prone to ALD hazard. The probability of pipeline exposure to PGD and the extent of the potential PGD obtained in Chapter 5 were used as input. The computer program introduced in Chapter 4 was employed in order to analyze the structural behaviour of pipelines and evaluate their vulnerability considering three damage mechanisms: tensile rupture, local buckling and premature cross-sectional failure. Vulnerability functions associated with PGD, expressed in terms of repair rate, were developed applying Monte Carlo simulation to the structural analysis results. These

vulnerability functions are specific to permafrost regions and can be incorporated in Hazus-type platforms for regional seismic risk assessment.

7.2 Conclusions

The following conclusions are drawn from this thesis:

Chapter 2:

- Pipe flexural rigidity and the soil density are key parameters which control the failure mechanisms of a soil-pipe system, i.e., pipe failure and soil failure.
- Under horizontal and vertical deformations, behaviour of unpressurized buried pipes with small D/t is similar to that of the in-air pipes. In this case, soil density and normalized burial depth determine the magnitude of the developed bending moment and the corresponding curvature. On the other hand, the behaviour of unpressurized buried pipes with large D/t ratio is sensitive to soil density and different from the in-air pipes. The flexural capacity of buried pipes with small D/t decreases, whereas the capacity of those with large D/t increases. In both cases, premature failure caused by ovalization occurs earlier than what was expected by the current codes.
- Under vertical deformations, the induced bending moment depends on the direction of deformations, i.e., upward and downward, because the soil stiffness and bearing capacity differs in the two directions. This was not the case for the simulated lateral deformations with uniform soil properties.
- Response of pressurized pipes to bending moment depends on D/t and internal pressure. Response of pipes with small D/t compared to those with large D/t shows less sensitivity to the internal pressure. Generally, an increase of the internal pressure in pipes with large D/t improves their bending capacity; however, this is not the case for pipes with small D/t .
- Presented results enable analyses with simple one dimensional finite element models to consider geometrical cross-sectional nonlinearities of buried pipelines.

Chapter 3:

- In discontinuous permafrost regions, acceleration response on top of frozen soils is higher than that on top of unfrozen soils. However, the amount of difference depends on several factors such as shaking intensity, shear wave velocity of frozen soil, thickness of deposit, etc.
- The acceleration responses of frozen and unfrozen soil parts are sensitive to their corresponding width: the frozen block response decreases with increase of the frozen block width, whereas the unfrozen soil response decreases with increase of the unfrozen part width.
- The relative depth of the frozen blocks did not show considerable effects on the frozen block and unfrozen soil responses.
- Considering more than two intermittent blocks in the numerical studies of the site response, showed only minor differences in the response of frozen blocks and unfrozen soils.
- The frozen block response is inversely proportional to the shear wave velocity of the frozen material; however, the unfrozen soil response is not sensitive to that.
- Site response of the cases in which plane strain conditions were not satisfied were successfully simulated by the 2D plane strain numerical models.

Chapter 4:

- In discontinuous permafrost during wave propagation under ISS conditions, higher strains are developed in the pipeline compared to the homogeneous ground conditions.
- It was confirmed that similar to the homogeneous ground, the pipe axial strains developed by R waves in discontinuous permafrost are dominant compared to the bending strains.
- Accounting for the soil-pipe interaction in the analyses indicated that strains developed in the pipe are larger when they are buried in denser soils.
- Although the bending strains increased under the MSS compared to the ISS conditions, the axial strains remained unchanged and dominant again. It was concluded that MSS conditions are more critical.

- It was shown that pipe strains have an inverse relationship with frequency content of the ground particles vibration, i.e., the higher the frequency the lower strains are generated.
- Results for varying pipe diameter (D) and diameter to wall-thickness ratio (D/t) revealed that small-diameter pipes with large D/t are the most critical condition. As well, larger strains are developed in pipelines with higher burial depths.
- Under all other conditions equal, largest strains were developed in small-diameter slender pipes under low-frequency soil particle vibration. However, for modern straight, flawless and corrosion-free pipelines the seismic performance is satisfactory with a good margin of safety against tensile rupture, local buckling and premature cross-sectional failure.

Chapter 5:

- Pipeline exposure to seismic-induced active layer detachment hazard heavily depends on the distance from scar crown to the pipeline axis.
- Study on the effect of thaw-consolidation phenomenon confirmed that the presence of pre-earthquake excess pore water pressure in the active layer of permafrost increases the probability of exposure and the number of the weakening instabilities. In addition, increase of earthquake magnitude and decrease of source-to-site distance increase the number of weakening instabilities.
- PGDs of the earthquake-induced ALDs applied to pipelines follow the Weibull distribution and its parameters, the scale and shape factors, for some cases were presented.
- Vulnerability of buried pipelines as well as any other linear infrastructure may be evaluated utilizing the findings of this chapter.

Chapter 6:

- Employing the results of Chapter 5 as input, the analytical vulnerability functions under the PGD hazard associated with earthquake-induced ALDs can be derived following these consecutive steps:

1. Apply finite element analysis method to determine variations of the critical level of the PGD lateral extent and width of the PGD zone. Results indicate the minimal width below which any PGD cannot cause damage to the pipeline.
 2. Combine results from step 1 with Monte Carlo simulations of the uncertain PGD zone width, in order to correlate the average number of repairs per ALD with PGD mean and coefficient of variation.
 3. Calculate the pipeline repair rate multiplying the probability of exposure (given in Chapter 5) with the site-specific ALD occurrence rate and the number of repairs per ALD (obtained from step 2).
- The internal pressure was shown to have a positive influence on the capacity of the buried pipes against PGD hazards.

7.3 Suggestions for future studies

Based on the undertaken research and obtained results, the following topics are recommended for future consideration:

- The developed Abaqus finite element model used to study ovalization in buried pipes was validated against a few laboratory tests reported in the literature. It is necessary to conduct more experimental modelling on buried pipes considering parameters such as pipe diameter and slenderness, soil type, burial depth and internal pressure.
- Conduct laboratory tests with real frozen soil instead of the soil-cement blocks. As well, experiments with simulated transitional zones between the frozen and unfrozen soils will make the results more reliable and closer to reality. Performing shaking table tests in centrifuge instead of 1g shaking table tests will also improve the quality of the results.
- Install dense arrays of strong motion seismographs in earthquake prone discontinuous permafrost regions to monitor seismic activity, wave propagation patterns and validate the findings of this study.

- Extend the numerical study of pipeline response to wave propagation, to different pipeline geometries such as bends and T-shape connections.
- Account for the effect of corrosion and other types of potential weakness on the pipeline response employing appropriate pertinent models.
- Investigate the effects of vertical seismic component on the pipeline response, especially when combined with the effects of frost heave and/or thaw settlement.
- Apply advanced models of cyclic loading to the soil-pipe interaction simulations.
- Increase the accuracy of the slope stability analysis conducting:
 - Study of the material transfer mechanisms in ALD and of the conditions under which each of the mechanisms occurs be determined;
 - Continuous monitoring of the behaviour of the potential unstable slopes be and post-seismic investigations performed;
 - Determine the distribution of the potential ALD locations along pipeline routes to estimate the occurrence rate of ALD more precisely;
 - Perform detailed geotechnical and geological site investigations to improve the accuracy of the input parameters (soil and slope).
- Develop or apply the existing predictive models for the ground long-term thermal behaviour to assess the long-term vulnerability of buried pipelines as a result of warming climate.

Appendix A

Technical specifications of measuring instruments

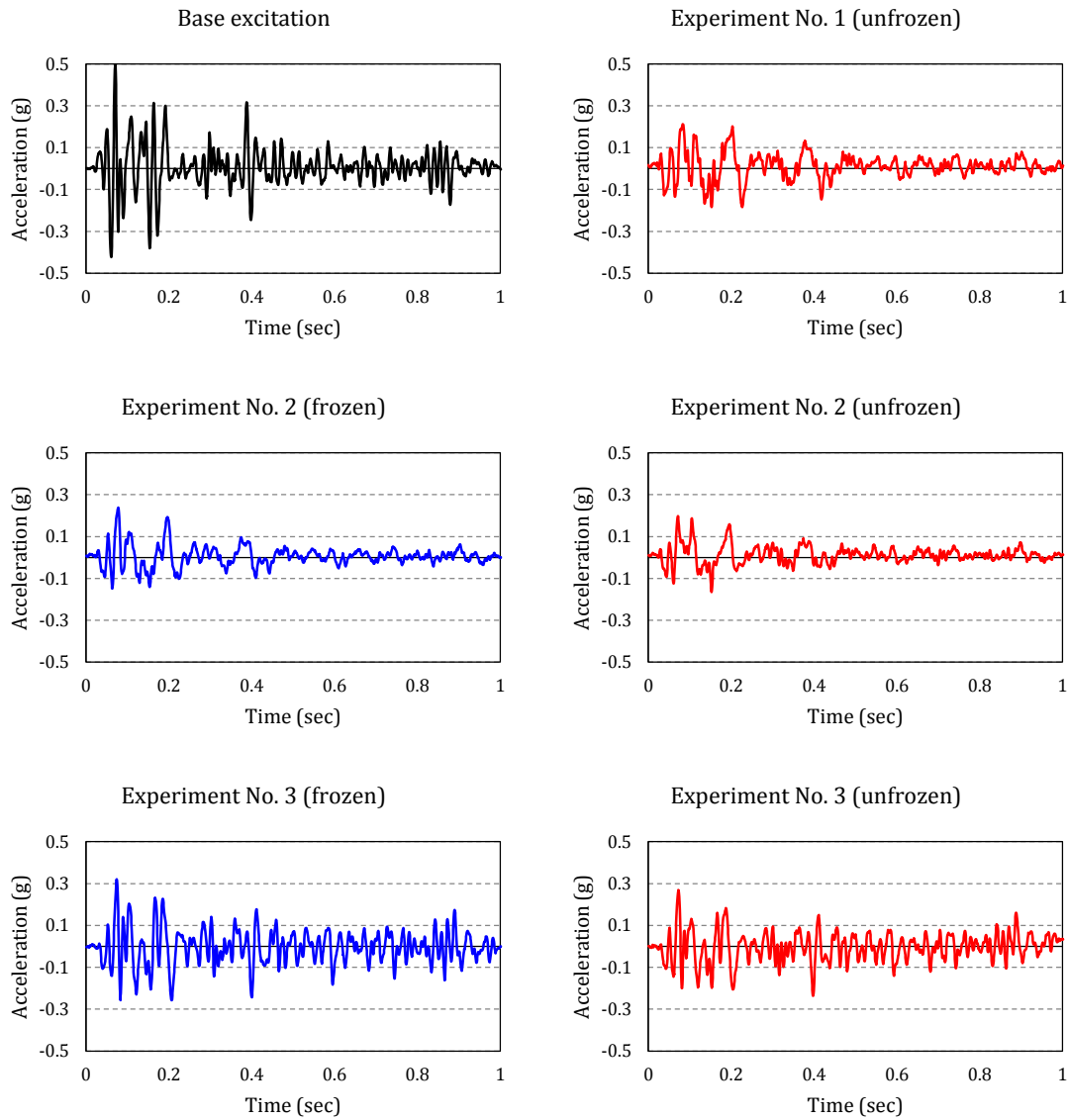
Accelerometers: Make and model: Analog Devices™ (ADXL203 Dual-axis); acceleration range: $\pm 5g$; specified voltage: 5 V; operating temperature range: -40 to $+125^{\circ}\text{C}$; maximum nonlinearity: ± 1.25 ; dimensions (in water-resistant shield): $22\text{ mm} \times 19\text{ mm} \times 15\text{ mm}$; weight (including water-resistant shield): 8.5 gr.

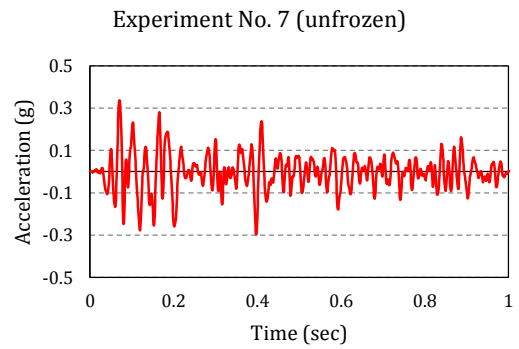
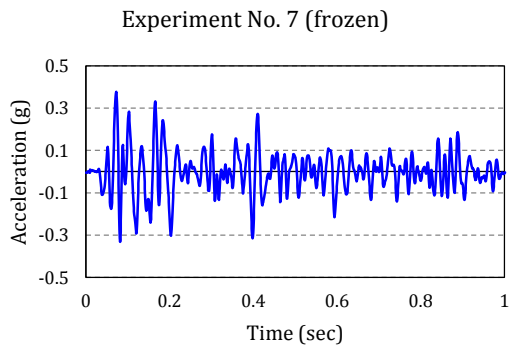
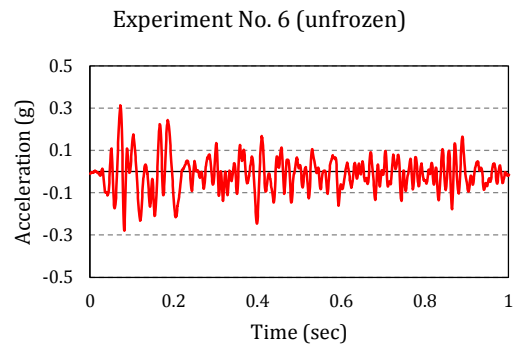
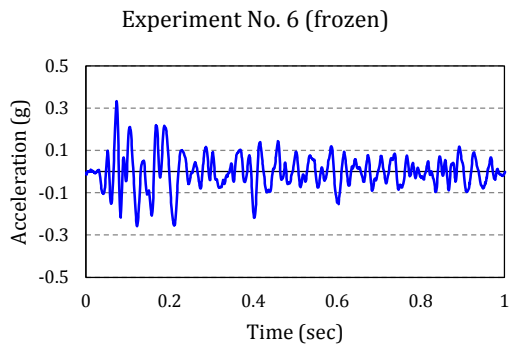
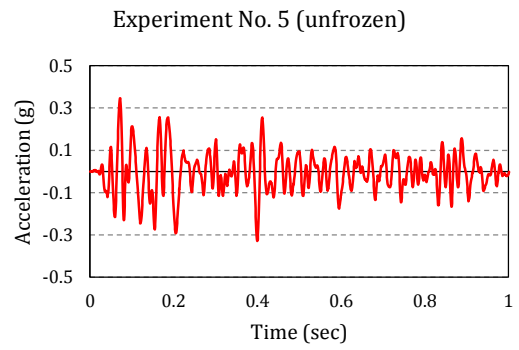
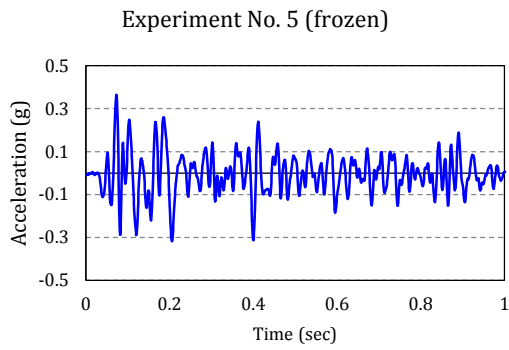
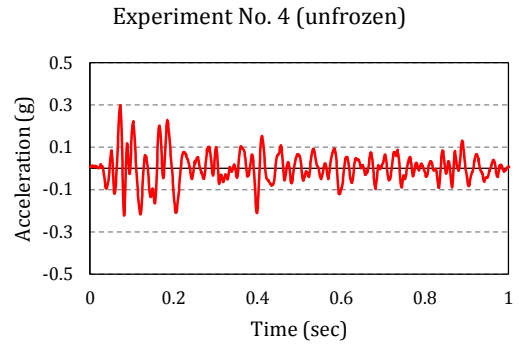
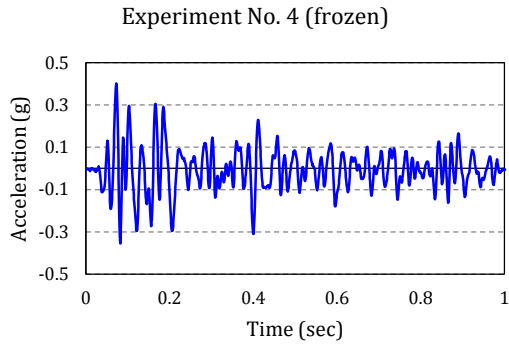
Pressure transducers: Make and model: Measurement Specialties™ (EPB-PW); pressure range: 0.1 MPa; full-scale output (FSO): 30 mV; operating temperature range: -40 to $+80^{\circ}\text{C}$; nonrepeatability: $\pm 0.25\%$ FSO; thermal zero shift: $\pm 4\%$ FSO/ 50°C ; thermal sensitivity shift: $\pm 2\%$ FSO/ 50°C ; dimensions (body): $\text{Ø}6.4\text{ mm} \times 11.4\text{ mm}$; weight (body): 0.8 gr.

Appendix B

Acceleration time-histories

Some of the recorded acceleration time-histories during the experiments No. 1 to 8 are presented in this appendix. Location of accelerometers is shown in Figure 3-4. All the ground responses given in Figure B-1 are obtained under high-intensity base excitations with $PGA=0.5g$.





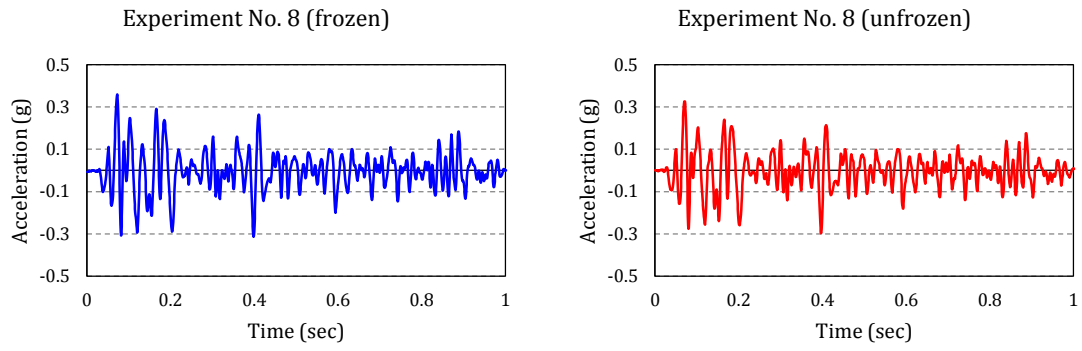


Figure B-1: Acceleration time-histories recorded during the experiments No. 1 to 8 under base excitation intensities with PGA=0.5g.

Appendix C

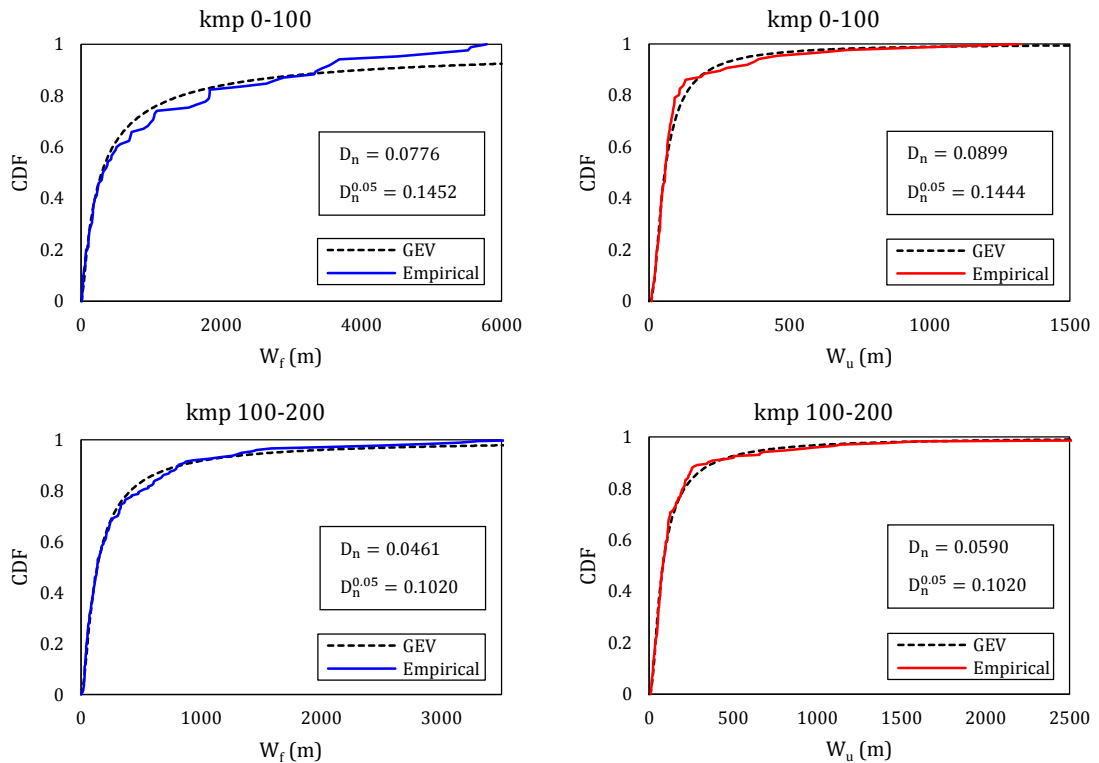
Evaluating the goodness-of-fit

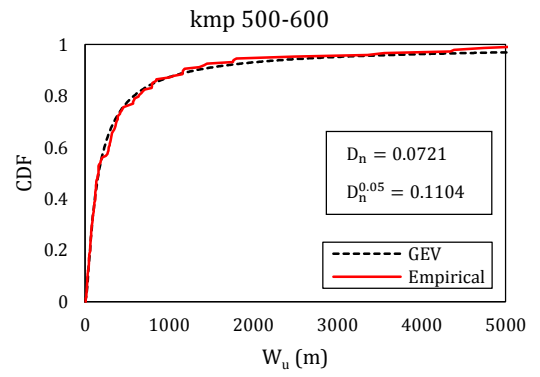
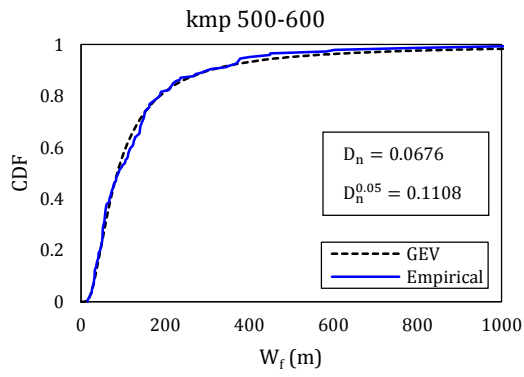
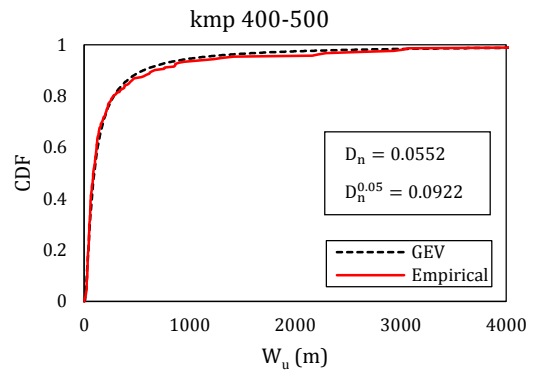
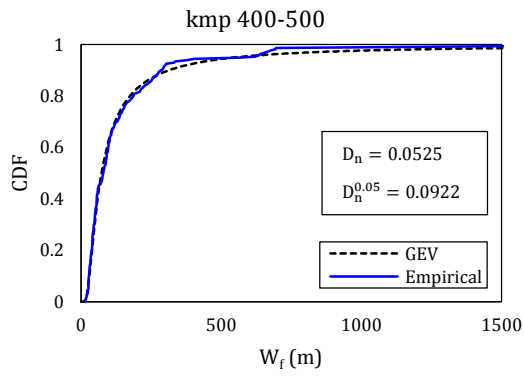
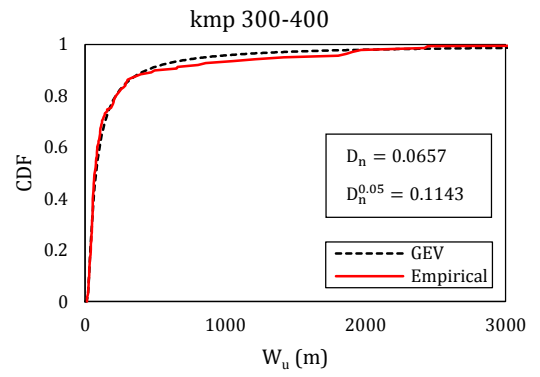
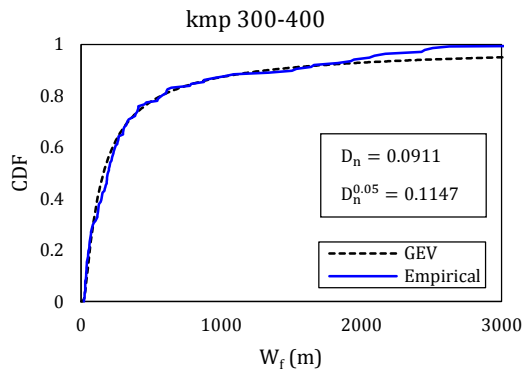
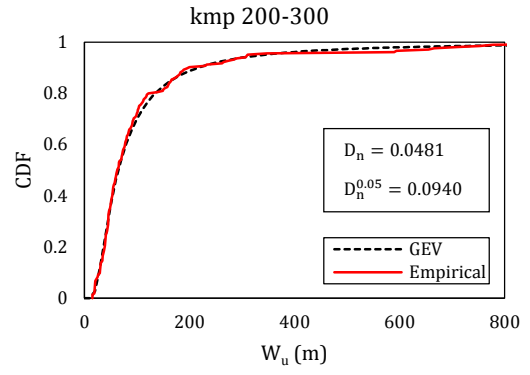
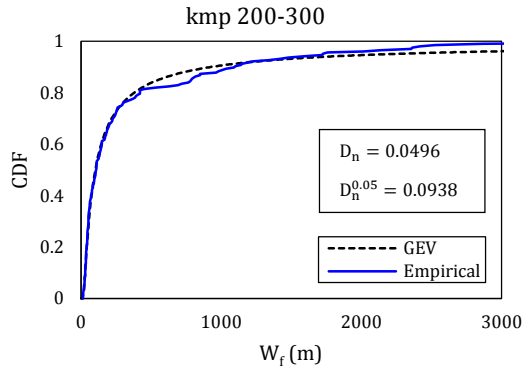
The Kolmogorov-Smirnov (K-S) test which is based on the difference between the observed and the assumed cumulative distribution functions (CDF) was conducted to evaluate the goodness-of-fit. For the sample size n , the maximum difference of the CDFs, D_n , is correlated to the significance level α by (Massey 1951):

$$P(D_n \leq D_n^\alpha) = 1 - \alpha$$

where, D_n^α is a critical value that depends on the sample size and the significance level and is given in the mathematical references.

Results of the K-S test ($\alpha = 0.05$) for measuring the compatibility of random samples (W_f , width of frozen blocks, and W_u , distance separating frozen blocks) with a theoretical probability distribution function (generalized extreme value, GEV) are presented in Figure C1.





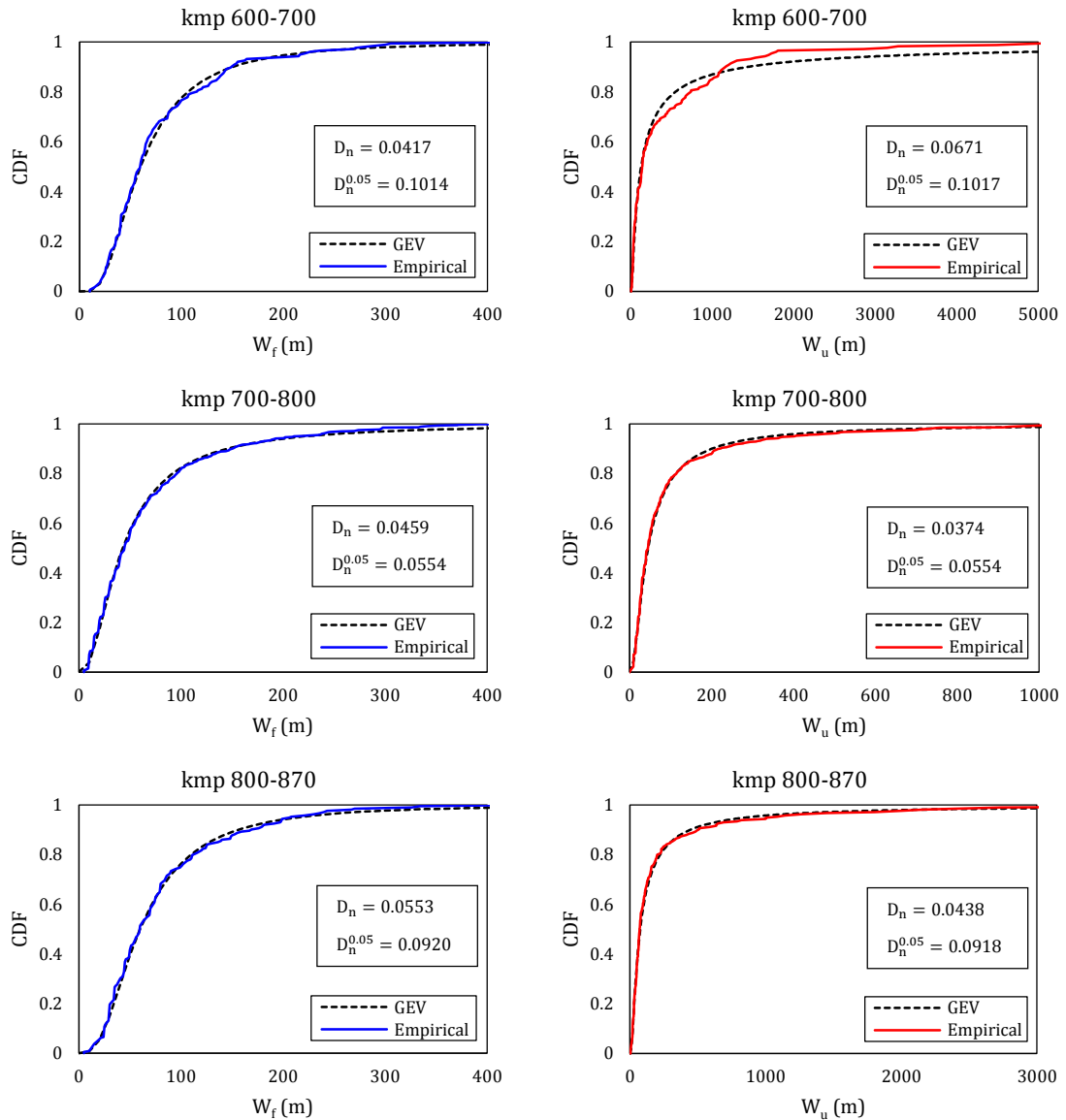


Figure C-1: Results of the K-S test ($\alpha = 0.05$) for evaluating the goodness-of-fit. W_f , width of frozen blocks, W_u , distance separating frozen blocks, and GEV, generalized extreme value distribution.

References

Massey, F. J. "The Kolmogorov-Smirnov test for goodness of fit." *Journal of the American Statistical Association* 46, no. 253 (1951): 68-78.

Curriculum Vitae

Name: Behrang Dadfar

Post-secondary Education and Degrees: Iran University of Science and Technology
Tehran, Tehran, Iran
1999-2003 B.Sc. (Civil Engineering)

Iran University of Science and Technology
Tehran, Tehran, Iran
2004-2007 M.Sc. (Structural Engineering)

The University of Western Ontario
London, Ontario, Canada
2011-2016 Ph.D. (Geotechnical Engineering)

Honours and Awards: Milos Novak Memorial Award (\$1,100)
The University of Western Ontario
2014

Ontario Graduate Scholarship (\$15,000)
2014-2015

Research Affiliate Program (RAP) Bursary (\$56,000)
Government of Canada – Natural Resources Canada
2011-2014

Related Work Experience: Teaching Assistant
The University of Western Ontario
2011-2016

Research Assistant

The University of Western Ontario

2011-2015

Structural and Bridge Designer

Vinehsaar Consulting Engineers

2007-2011

Publications:

Dadfar, B., M. H. El Naggar, and M. NasteV. "Vulnerability of buried energy pipelines subject to seismic wave propagation in discontinuous permafrost." *Soil Dynamics and Earthquake Engineering*, submitted.

Dadfar, B., M. H. El Naggar, and M. NasteV. "Vulnerability of buried energy pipelines subject to earthquake-triggered landslides in permafrost thawing slopes." *Computers and Geotechnics*, submitted.

Dadfar, B., M. H. El Naggar, and M. NasteV. "Quantifying exposure of linear infrastructures to earthquake-triggered transverse landslides in permafrost thawing slopes." *Canadian Geotechnical Journal*, submitted.

Dadfar, B., M. H. El Naggar, and M. NasteV. "Experimental and analytical study of seismic site response of discontinuous permafrost." *Canadian Geotechnical Journal* 53 (2016): 1-13.

Dadfar, B., M. H. El Naggar, and M. NasteV. "Ovalization of steel energy pipelines buried in saturated sands during ground deformations." *Computers and Geotechnics* 69 (2015): 105-113.

Dadfar, B., M. H. El Naggar, and M. NasteV. "Seismic behavior of buried energy pipelines in northern permafrost regions." *6th International Conference on Earthquake Geotechnical Engineering*, Christchurch, New Zealand, November 2015.

Dadfar, B., M. H. El Naggari, and M. Nastev. "Seismic site response of discontinuous permafrost." poster presentation in *85th Annual Meeting of the Eastern Section of the Seismological Society of America*, Charlevoix, Quebec, Canada, October 2013.

Kaveh, A., and **B. Dadfar**. "Optimum seismic design of steel moment resisting frames by genetic algorithms." *Asian Journal of Civil Engineering (Building and Housing)* 9 (2008): 107-129.

Kaveh, A., and **B. Dadfar**. "Eigensolution for free vibration of planar frames by weighted graph symmetry." *International Journal for Numerical Methods in Engineering* 69 (2007): 1305-1330.

Kaveh, A., and **B. Dadfar**. "Eigensolution for stability analysis of planar frames by graph symmetry." *Computer-Aided Civil and Infrastructure Engineering* 22 (2007): 367-375.